INFORMATION TO USERS

This manuscript has been reproduced from the microfilm master. UMI films the text directly from the original or copy submitted. Thus, some thesis and dissertation copies are in typewriter face, while others may be from any type of computer printer.

The quality of this reproduction is dependent upon the quality of the copy submitted. Broken or indistinct print, colored or poor quality illustrations and photographs, print bleedthrough, substandard margins, and improper alignment can adversely affect reproduction.

In the unlikely event that the author did not send UMI a complete manuscript and there are missing pages, these will be noted. Also, if unauthorized copyright material had to be removed, a note will indicate the deletion.

Oversize materials (e.g., maps, drawings, charts) are reproduced by sectioning the original, beginning at the upper left-hand corner and continuing from left to right in equal sections with small overlaps. Each original is also photographed in one exposure and is included in reduced form at the back of the book.

Photographs included in the original manuscript have been reproduced xerographically in this copy. Higher quality 6" x 9" black and white photographic prints are available for any photographs or illustrations appearing in this copy for an additional charge. Contact UMI directly to order.

UMI

A Bell & Howell Information Company
300 North Zeeb Road, Ann Arbor, MI 48106-1346 USA
313/761-4700 800/521-0600

A study of galaxy interactions

by

Vassilios Charmandaris

A Dissertation Submitted to the
Graduate Faculty in Partial Fulfillment of the
Requirements for the Degree of
DOCTOR OF PHILOSOPHY

Department: Physics and Astronomy
Major: Astrophysics

Approved:

Curtis Struck

In Charge of Major Work

DKFinnemore

For the Major Department

For the Graduate College

Members of the Committee:

Russell J. Lavery
Dennis K. Ross
C. Soukoulis
Stephen J. Willson

Iowa State University
Ames, Iowa
1995

TABLE OF CONTENTS

LIST OF TABLES

LIST OF FIGURES

ACKNOWLEDGEMENTS

I would like to thank my advisors Curt and Phil for keeping my motivation and excitement for learning and doing research high over the past several years. Without their guidance, patience, and understanding I would not have completed this work.

I am grateful to Dr. Kevin Olson (NASA/GSFC) who provided the original N-body code and introduced me to the concepts of efficient parallel programming. His advice and suggestions during our collaboration was invaluable.

I would also like to thank the members of my committee for their constructive criticism and comments. In particular, I would like to acknowledge the help of Dr. Russell J. Lavery for expanding my background in astronomy, as well as, for raising my spirit when I was disappointed and bringing me down to earth when I was getting carried away.

Finally, I want to express my gratitude to the members of the Greek community of Ames and in particular to the families of Costas Soukoulis and Costas Stassis. Their presence made the harsh winters of the Midwest seem less unfriendly.

This dissertation is dedicated to my parents *Γιώργο* and *'Ελένη* who unconditionally supported me over the past 28 years. When I applied for graduate studies, my father had his doubts that someone would actually pay me money to pursue a career in astronomy. Six years have passed and I still haven't proven him wrong ...

CHAPTER 1. INTRODUCTION

1.1 Overview

Heisenberg, a Nobel laureate physicist, stated that no lecture or treatise on any scientific subject would be complete unless it began with a reference to the Classical Greek philosophers. He believed that they had presented ideas so fundamental that they should be the starting point of all current research. Therefore, I begin the introduction of this dissertation with a quote of the ancient Greek philosopher Heraclitus.

> The Universe, in which everyone of us lives, was created by neither a God nor a Human. It was, it is, and it will remain an everlasting fire. A fire which lights with “*μέτρον*”[1] and extinguishes with “*μέτρον*”.

I hope that by end of this thesis and after presenting the detailed study of the dynamics and star formation properties of two interacting galaxies, it will be evident that the previous quote was of some relevance.

---

[1] “*μέτρον*” is a Greek word which attributes to the subject the meaning of “order” and “moderation” due to a physical law.

1.2 Galaxies

The concept of galaxies (ensembles of $O(10^{11})$ gravitationally bound stars) outside the Milky Way was unknown to astronomers until the end of the first quarter of this century. Up until the *Great Debate* between H. Shapley and H.D. Curtis in the 1920s on the origin and distances of some "spiral nebulae", the majority of the scientific community believed (like Shapley) that everything one observed in the sky was part of our Galaxy. In this debate, Curtis presented new evidence that the spiral nebulae were not gravitationally bound to our Galaxy. Few years later, in 1923, E. Hubble, using the recently completed 100-inch telescope at Mount Palomar, observed the outer disk of M31 and M33 and for the first time he was able to resolve in them hundreds of objects that could be identified as individual stars. The luminosity of those stars was so small that even if one assumed that they had the same absolute luminosity as the most luminous stars of our Galaxy, they had to be in distances much further than the edge of our Galaxy. Subsequent observations by Hubble of *Cepheid* variables and the determination of the actual distance to M31 (known also as the great galaxy of Andromeda) proved Curtis's point of view correct and established once and for all the extragalactic origin of the "spiral nebulae" (Hubble 1925, 1926, 1929, 1936).

1.2.1 Galaxy Classification and Evolution Scheme

Observations clearly show that galaxies present a wide range of morphologies. They have different sizes, shapes, and absolute luminosities (Mihalas & Binney 1981). Based on their morphological characteristics galaxies are classified as Ellipticals (E) (about 13%), Lenticulars (S0) (about 22%), Spirals (S) (about 61%) and Irregulars

(I) (about 4%). The most widely used classification scheme was introduced by Hubble (1936) and is presented in Figure 1.1.

Hubble used the terms "early" and "late" type in characterizing the galaxies as one moves along the sequence from ellipticals to spirals. These terms, though, do not imply any kind of evolution. It was Sandage (1961) who suggested that if the Hubble classification scheme indicates an evolution, then it should go in the opposite sense, that is from right to left (from Sc to Sa and SBc to SBa). The observational evidence which support such a sequence are :

1. The percentage of gaseous component (H I, CO) decreases from Sc to Sa. This is consistent with stellar evolution which leads to the depletion of the interstellar gas.
2. The total visible mass increases from Irr to Sc to S0.
3. The bulge to disk luminosity ratio increases from late to early type spiral galaxies. If the mass to light ratio (M/L) remains the same for all types of galaxies this implies that the mass concentration also increases. If there is an evolution in the morphology, this can only be towards increasing the mass concentration.
4. Early type spirals have closely wound spiral arms while late types have more open arms.

1.2.2 The Role of the Gas

The observational evidence presented in the previous section indicate that galaxy evolution is primarily controlled by the dynamical behavior of the gas in the galaxies. It is the gaseous content that causes dynamical dissipation, fuels star formation, and

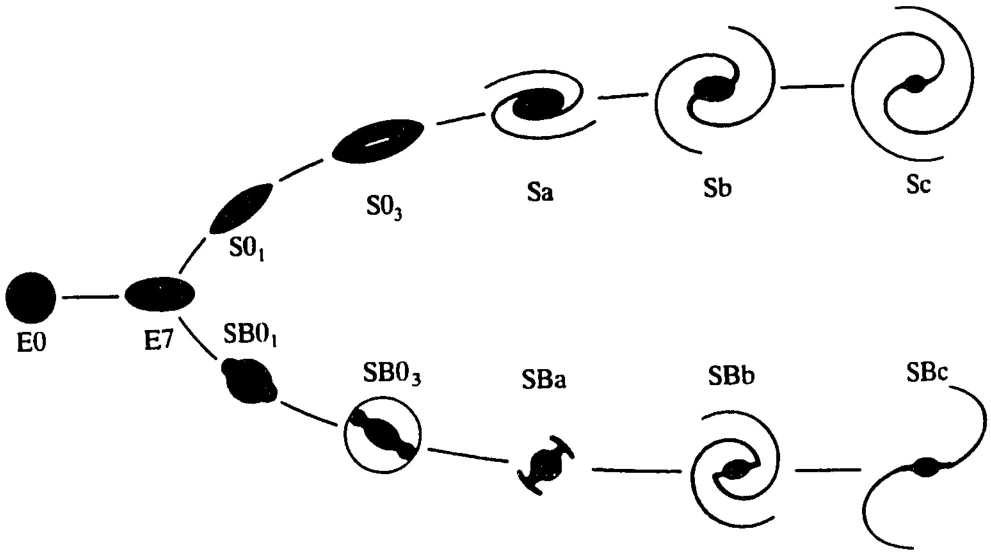

Figure 1.1: The Hubble *tuning-fork diagram* (Mihalas & Binney 1981).

changes the morphology of galaxies. Hence, in order to be able to construct a model which would explain the formation and evolution of galaxies, one needs to study the basic mechanisms that influence the behavior of the gas.

The mass distribution of the gaseous component of a galaxy is determined by and also influences the gravitational potential of the galaxy. In a simplified picture, if for some reason a gravitational instability occurs at a localized region of the galaxy, the gas density will increase (Binney & Tremaine 1987). If this increase in gas density is over a critical value, the gas clouds will fragment and collapse leading to the formation of stars (Elmegreen 1992, and references therein). Such types of instabilities can be local or a result of a more general disturbance to the potential of the galaxy. Typically, star formation is observed in the core of galaxies where the gravitational potential reaches a minimum, in areas of local minima such as spiral waves, and in galactic bars. Bars which can be considered the result of the superposition of leading and trailing waves on the galactic disk (Lynden-Bell & Kalnajs 1972), are of the few long-lived features currently observed (Pfenniger & Norman 1990). As a result, they are one of the driving mechanisms of galaxy evolution. They may lead to formation of nuclear rings (Schwartz 1981) and since they help transfer angular momentum outwards, they can produce mass concentrations near the galactic center (Combes 1994 and references therein).

Another event that can disturb the potential and change the morphology of a galaxy is a gravitational interaction with another galaxy.

1.3 Galaxy Interactions

A galaxy may interact with another galaxy more than once over a Hubble time. This is not surprising since galaxies tend to form in groups or clusters and the typical intergalactic distance is usually just an order of magnitude greater than the typical size of a galaxy. Thus, galaxy evolution is strongly influenced by the environment.

The pioneering work by Toomre & Toomre (1972) showed the profound changes in the morphology of a galaxy resulting from the tidal interaction with a companion in near parabolic orbit. In the same paper, the authors, using arguments based on the dynamics of the encounters, speculated that a) galaxy interactions could be more frequent in the past, b) they could lead to the formation of elliptical galaxies, and c) they could "... bring deep into the galaxy center a sudden supply of interstellar gas which could fuel the activity of "exotic" phenomena such as jets." Over the years, most of their predictions have proven correct.

The enhancement of star formation rate (SFR) in interacting systems was shown by the study of Larson & Tinsley (1978). They constructed color evolution models which could explain the differences in the UBV plane scatter (see Figure 1.2) of peculiar/interacting systems when compared with normal galaxies. Their study showed that the large scatter in the colors of peculiar galaxies is consistent with bursts of SFR with time scales $\leq 2 \times 10^7$ years. In contrast, colors in normal galaxies are consistent with a monotonically decreasing SFR and few have experienced large variations in SFR with time scales $\leq 5 \times 10^8$ years.

Numerical simulations of merging disk galaxies of equal mass (Barnes 1992), indicate that the end product of the interaction can have the morphological characteristics of an elliptical galaxy. Cosmological N-body simulations ($N > 10^6$) also

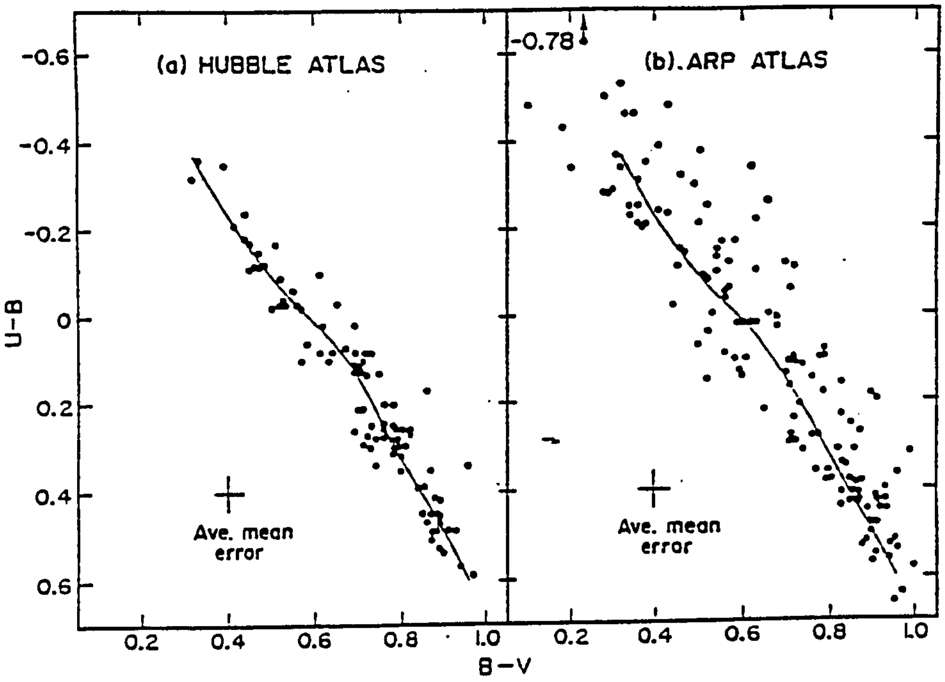

Figure 1.2: A two-color plot for morphologically normal and peculiar galaxies. The peculiar galaxies where taken from the Arp atlas. The solid curve is an eye estimate mean line through each sample (Larson & Tinsley 1978).

showed that multiple mergers can lead to the formation of elliptical galaxies (Fullagar *et al.* 1992).

Observations of distant clusters of galaxies ($0.003 \leq z \leq 0.54$) revealed an excess in the number of blue galaxies (Butcher & Oemler 1978, 1984). This effect (also known as "Butcher-Oemler" effect) was consistent with the hypothesis that there was an excess in the SFR in the past. Imaging of few of those distant clusters by Lavery & Henry (1988), showed that the blue galaxies were morphologically disturbed. They also exhibited tidal features which could be the result of interactions.

It is now believed that the ultra-luminous IRAS galaxies (Soifer, Houck & Neugebauer 1987) are triggered by such collisions. This is fairly clear since many bright IRAS galaxies display signs of mergers, such as multiple nuclei, shells and loops (Allen, Roche & Norris, 1985; Sanders *et al.* 1988). As a consequence, it is possible that a significant fraction of stars in the universe were formed in galactic–scale collision/merger events. It is therefore important not only for galaxy formation and evolution, but also for the history of star formation and metal enrichment in the universe, to develop a good understanding of precisely what happens in strong collisions among gas–rich galaxies.

1.4 Ring Galaxies

The morphology of galaxies which have experienced interactions with neighboring systems varies greatly (Toomre 1977). It depends on the type of galaxies that interact, the orbital parameters of the interaction, as well as how evolved the system is when we happen to observe it. The majority of merger remnants are fairly complicated systems. As a result, understanding the dynamical history and evolution of a typical merger remnant is a non-trivial problem.

One special class of colliding or merging galaxies is the **ring** and **ring-like** galaxies. Collisional ring galaxies represent a class of interacting gas-rich systems in which at least one of the member galaxies remains sufficiently intact after the collision (Lynds & Toomre 1976, Toomre 1978, Appleton & Struck 1995 and references therein). Typically a ring galaxy is formed when a companion passes through the center of a larger rotating disk galaxy driving ring-like density waves through the disk. The over-density of the gas in the wave triggers intense star formation along the rings. In a sense, the ring galaxy serves as a galaxy-scale perturbation experiment that allows the study of hydrodynamic and stellar evolutionary processes that influence the disk. In most cases, the gravitational perturbation due to the collision is modest, which allows models of star formation to be critically examined.

Ring galaxies are much more rare than other types of galaxy interactions. However, their geometrical simplicity makes them prime candidates for creating detailed models of their dynamics and star formation properties. The fact that the typical timescale of propagation of the ring waves through the disk is comparable to the dynamical timescale of the interaction (10^8 years) makes it easier to identify the possible companion galaxy and to test our models against the observations.

1.5 The Galaxies Studied

In this dissertation I present the study of two galaxies, namely Arp 10 and VII Zw 466. Both of them belong to a larger sample of ring galaxies which has been studied extensively using optical, infrared, radio imagery and spectroscopy (Appleton & Marston 1995, Marston & Appleton 1995, Appleton & Struck 1995 and references therein).

Using the 2.1 m telescope at Kitt Peak National Observatory, we performed optical imaging and longslit spectrophotometry of both systems in order to collect information about the morphology, star forming properties and kinematics of the stellar component. To probe the dynamics and distribution of the neutral hydrogen gas in both systems, we also obtained 21 cm radio observations, using the C-Array of the VLA.

1.6 Dissertation Organization

This dissertation consists of six chapters. The first chapter is the introduction, chapters two and three are papers on Arp 10 and chapter four contains a paper on VII Zw 466. In chapter five we present a detailed description of the method used to develop our numerical simulation program. Our general conclusions and future research plans are presented in the chapter six, while the code developed is included in the Appendix.

CHAPTER 2.

THRESHOLD STAR FORMATION EFFECTS IN THE PECULIAR GALAXY ARP 10 (= VV 362)

A paper published in The Astrophysical Journal, 1993, **414**, 154

Vassilis Charmandaris, Philip N. Appleton & Anthony P. Marston

2.1 Abstract

We present images of the peculiar galaxy Arp 10 which reveal two rings of concurrent star formation. Apart from a bright ring visible on early photographs of the system, an even brighter inner ring of H II regions is found within the nuclear bulge of the galaxy. A very faint ring-arc of H II regions is also seen associated with a third outer ring or shell. We detect a small companion galaxy on the minor axis of Arp 10 and an extended extra-nuclear knot which lies between the first and second rings. An investigation of the Hα fluxes in the rings reveals an increase in the emission where the ring surface density in the R–band light exceeds 21.3±0.2 mag arcsec^{-2}. If the R–band light is dominated by old stars in the underlying density wave, then the results suggest evidence for a star formation law which exhibits a threshold dependence on the strength of the density wave in the rings. Even if the R–band continuum in the ring is heavily contaminated with red light from the underlying young stars (a result

at odds with the smooth continuum morphology of the ring) then a smaller, but still significant non-linear enhancement in the star formation rates in one segment of the second ring is required to explain the results. In either case, strong trends in the star formation rate with azimuth around Ring 2 are in good agreement with off-center collisional ring galaxy models.

2.2 Introduction

Arp 10 (= VV 362) is a galaxy containing a bright ring, an off-center nucleus and a faint bar. Vorontsov-Velyaminov (1977) describes the galaxy as containing " ... an enormously developed massive part of the ring" which we will later show is a region of enhanced star formation in the ring. Arp 10 was noted as a ring galaxy by Dahari (1985). Faint traces of outer filaments resembling antennae are seen protruding from the galaxy in the photograph presented in the Arp Atlas of Peculiar Galaxies (Arp 1966) suggesting that Arp 10 may be a colliding system. Although the outer filaments in Arp 10 in some ways resemble shells around some elliptical galaxies (Malin and Carter 1983), the single dish H I spectrum of the galaxy obtained by Sulentic and Arp (1983) exhibits the typical two-horned profile of a rotating planar disk.

We present deep CCD images of Arp 10 which support the collisional picture for the formation of the ring and filaments. A small elliptical companion is found approximately one ring diameter from Arp 10 on its minor axis, suggesting that Arp 10 may be a ring galaxy formed by the head-on collision of a small intruder galaxy through the center of a rotating disk (Lynds and Toomre 1976; Theys and Spiegel 1977). Another ring and additional ring-arcs are also discovered in the light of Hα in Arp 10. The newly discovered ring lies in the inner regions of the central bulge. The Hα imaging also reveals sharply defined ring-arcs associated with the faint outer filaments. Multiple rings are expected in well evolved models of colliding ring galaxies (Toomre 1978; Appleton and Struck-Marcell 1987, hereafter ASM; Struck-Marcell 1990).

Ring galaxies provide an ideal laboratory for exploring models of star formation triggered by density waves. Of special interest is the mildly off-center collision between an intruder galaxy and a disk. It has been argued by Appleton and Struck-Marcell (1987) that such a collision will generate an expanding ring wave which shows large but smooth variation in stellar and gaseous density around the ring. Such a wave is an ideal tool for exploring the dependence of star formation rate (hereafter SFR) on ring surface density in galaxies. The work is relevant to threshold star formation mechanisms such as those put forward by Scalo and Struck-Marcell (1984; 1986), Struck-Marcell and Appleton (1987), hereafter SMA, for colliding systems as well as Kennicutt (1989; 1990) for normal galaxies (See also observations by Skillman 1987; Schombert and Bothun 1988; Carignan and Beaulieu 1989).

In this paper we will investigate the peculiar morphology of Arp 10 and will calculate the SFR in the bright knots in all three ring structures. In § 2 we describe our observations and we present the optical morphology of Arp 10 in § 3. In § 4 we present details of how we performed the photometry and the star formation rate (SFR) calculations. The results are presented in § 5. In § 6 we describe some predictions based on existing models. In § 7 we discuss their physical significance, and our conclusions are highlighted in § 8. The systemic heliocentric velocity of Arp 10 is 9093 $\mathrm{km\,s^{-1}}$ (Sulentic and Arp 1983). Using the velocity corrected for motion relative to the local group (de Vaucouleurs de Vaucouleurs and Corwin 1976) and assuming a value for the Hubble constant of 75 $\mathrm{km\,s^{-1}\,Mpc^{-1}}$ we estimate a distance to Arp 10 of 122 Mpc.

2.3 Observations

The observations were made during photometric conditions on the night of January 19 1991 using the KPNO 2.1 m telescope. Images were obtained through a broad-band R and a narrow band 80 Å wide filter, centered close to the wavelength of redshifted Hα and [N II]. The detector was a Tek2 512×512 pixel^2 CCD. Two 1500 s observations were made using the Hα + [N II] filter in order to detect emission from the star forming knots. A 1200 s exposure was taken using the R-band filter. Bias subtraction and flat fielding of the images was performed in a standard way. Flat fields were obtained using sky observation made during the morning twilight. The continuum was removed from the spectral line images using a carefully scaled R-band image. The seeing disks were very similar for both the line and continuum images (FWHM = 1.2 arcsec). Calibration of the photometry was performed using data taken from the star Hz 15 (Stone 1974) and the standard star 95 52 (Landolt 1983).

As a further check of the reliability of the R-band image as a good representation of the stellar continuum, we made further observations of Arp 10 with the newly commissioned wide-field CCD system at Iowa State University's E. W. Fick Observatory. The Fick wide-field CCD camera was attached to the 0.6 m Mather telescope with a focal reducer providing an f/4 beam at the detector. The CCD is a thinned TI 800×800 pixel^2 device providing a 1.3 $\mathrm{arcsec\,pixel^{-1}}$ image scale. The observations of Arp 10 were made during the nights of August 28 and 29 1992 through a narrow band, 50 Å wide interference filter, centered at 6700 Å. This provided a narrow-band continuum with no possibility of contamination by hydrogen emission lines. No discernible difference was found between the KPNO R-band and the Fick Observatory image down to a level of 5%. (see Appendix)

2.4 Optical Morphology

A grey-scale representation of the R-band image is shown in Figure 2.1. The galaxy has a dominant ring containing a nucleus and faint bar and an outer structure which extends from the south-east in shell-like filaments. We indicate in Figure 2.1 a possible elliptical companion galaxy to Arp 10, which lies 60 arcsec to the north-east on the minor axis of the ring. If Arp 10 is a collisional ring system this is a prime candidate for the intruder galaxy. A bright extra-nuclear knot is also seen close to the nucleus of Arp 10 to the south-west. This knot, which is also marked in Figure 2.1, may be in some way related to the collisional nature of the system. It is also visible in Hα emission, which indicates that it must belong to the system. We will not elaborate more on its nature since we do not yet have radial velocity measurements which would help to further define its relationship to the disk of Arp 10.

In Figures 2.2 and 2.3 we show a grey-scale image and a contour map, of the Hα+[N II] line emission from Arp 10. In addition to the bright ring we also see for the first time the strong inner line-emitting ring which lies within the central bulge of Arp 10. Faint outer emission knots are also visible associated with the shell-like continuum especially to the north-east. We will refer to the inner ring, the bright intermediate ring and the outer ring-arcs (see Figure 2.2) as Rings 1, 2 and Ring-arc 3 throughout this paper. The radii of the three ring-like structures are 2.8, 21.5 and

40 arcsec respectively.

2.5 Photometry and SFR Calculations of the Ring Knots and Arcs

The photometric fluxes of the many bright knots in Arp 10 were determined in two ways:

- I. We integrated the flux contained within each knot down to an Hα isophotal level of 0.60×10^{-16} ergs $\mathrm{cm}^{-2}\mathrm{s}^{-1}$ arcsec^{-2} (2.5 × rms noise level in the image). The boundaries defined by this isophotal level in the Hα map were then transferred to the suitably registered R-band continuum image in order that the R-band flux be estimated over the same area. From these flux estimates and a knowledge of the area of the limiting contour, we then calculated the surface brightness of the regions in both Hα and red continuum light.
- II. We performed photometry in a fixed circular software aperture with a radius of 2.87 arcsec centered on each bright knot of Ring 2. Again the surface brightness at the same aperture center was estimated once the fluxes had been evaluated.

We calculated of the surface brightness using these two different methods in order to ensure that the surface area of the flux evaluation did not play a significant role in the final results. Indeed, as will be shown below, the two methods yield similar results.

In Figure 2.2, we indicate the specific areas over which the flux was evaluated down to the isophotal limit given above (Method I). The regions, presented in Table 2.1, are labeled 1–29, for future reference. We note that for the very bright

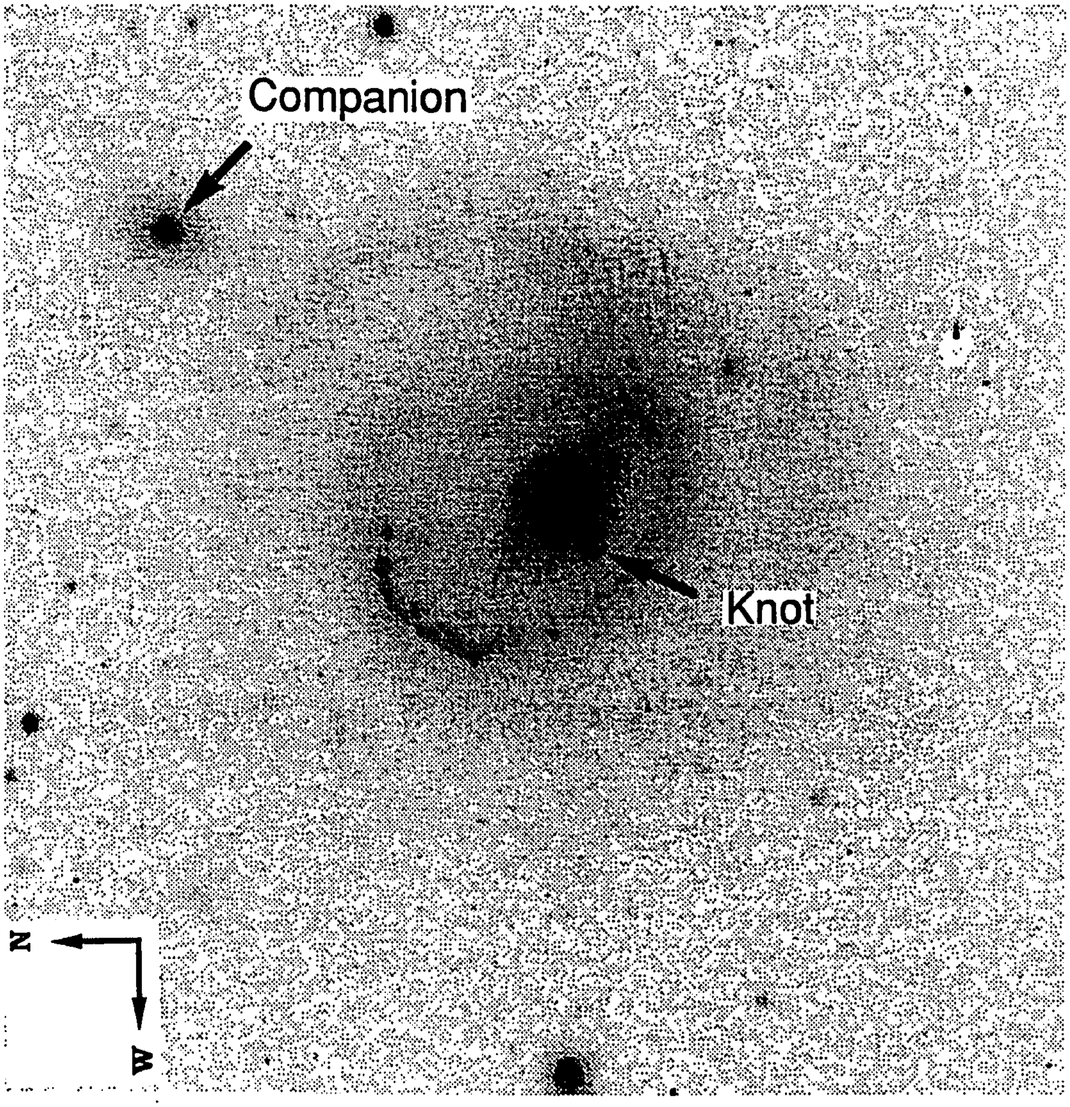

Figure 2.1: Greyscale image of Arp 10 through the R-band filter. Note the possible elliptical companion galaxy seen to the north-east of Arp 10 and the bright extra-nuclear knot which lies to the west of the nucleus. North is to the left and west is at the bottom in all the images in this paper.

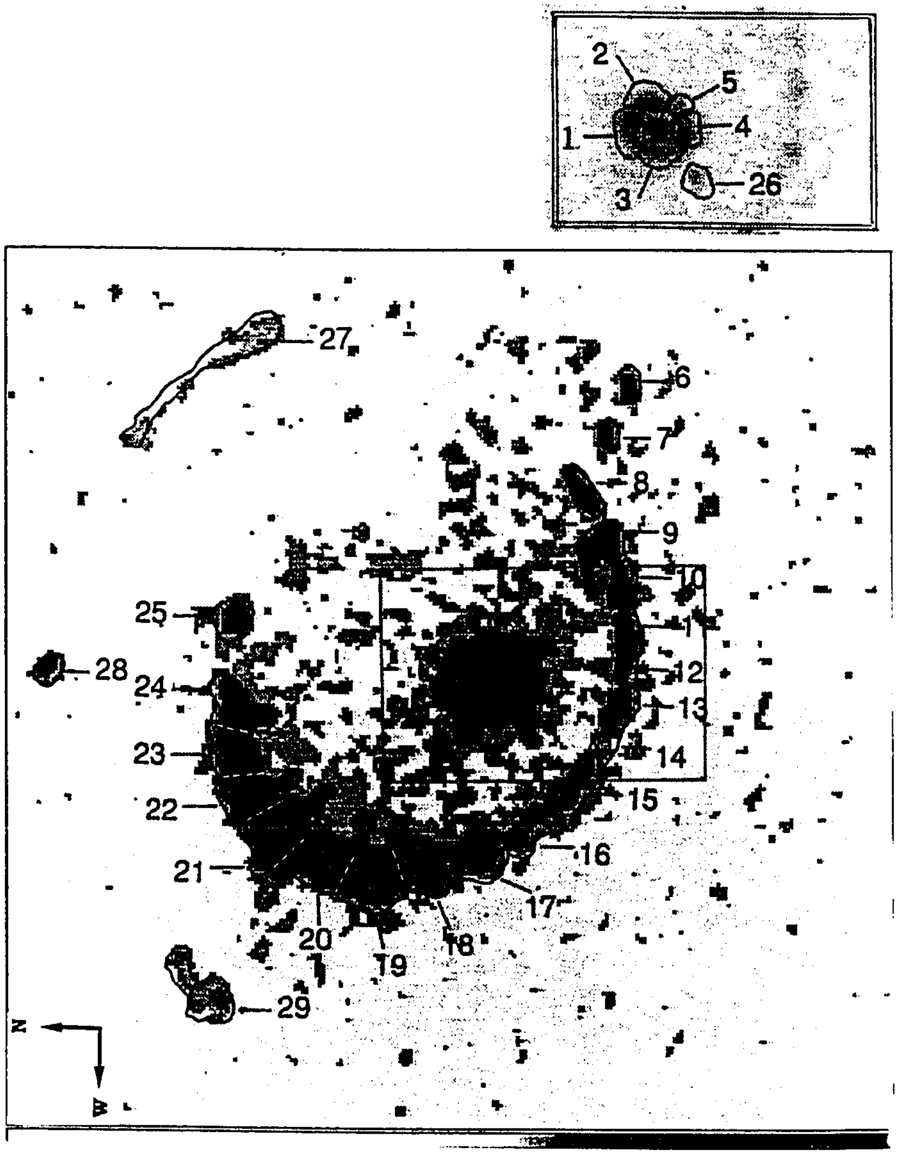

Figure 2.2: Greyscale image of Arp 10 through a narrow band (80 Å wide) filter centered close to the wavelength of redshifted Hα and [N II]. The inset shows the same region defined by the box but at a different greyscale contrast level, emphasizing the ring-like nature of the inner ring. The numbered region are discussed in the text.

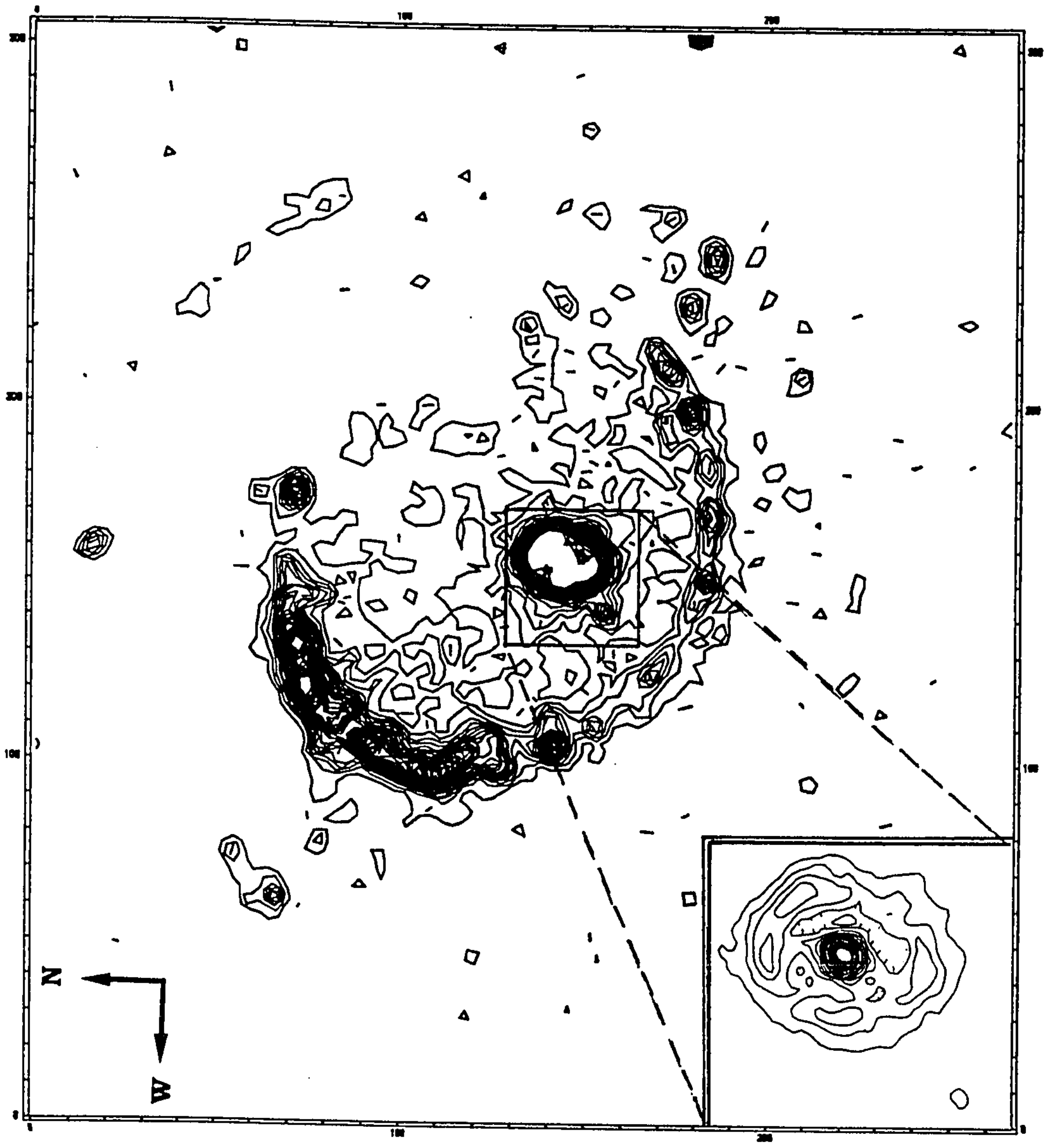

Figure 2.3: Contour map of Figure 2.1. The contour levels are at 0.36×10^{-16} ergs cm^{-2} arcsec^{-2} increments, between 0.36×10^{-16} ergs cm^{-2} arcsec^{-2} and 14.3×10^{-16} ergs cm^{-2} arcsec^{-2}. The inset shows details of the inner ring and nucleus.

north-west region of Ring 2, an entire portion of the ring exceeds the isophotal limit because the many bright knots which lie close together in that region cause the contours to merge. Since we are primarily interested in surface brightness rather than total flux in our discussion below, we decided to split up this part of the ring into segments equal in length to the isophotal thickness of the ring (about 5 arcsec). We attempted to include one bright H II region complex in each ring segment and avoided bisecting bright partially resolved hot-spots. A similar argument applies to the inner ring which also exceeds the isophotal limit over its entire extent. The two western knots associated with the ring-arc were included in the calculations. However, one section of the outer ring-arc subtends a large area at a surface-brightness level of 0.3×10^{-16} ergs s^{-1} cm^{-2}. Although this was below our isophotal limit, we decided to include the arc region for completeness.

The regions used in the constant aperture method (Method II) a–s, are presented in Table 2.2. The circular aperture was centered at each bright knot which was included in the regions selected for Method I. In this way the regions a–f correspond roughly to regions 6–11 and regions g–s to regions 13–25.

Star formation rates have been estimated from Hα fluxes by a number of authors but most notably by Kennicutt (1983) and Gallagher Hunter and Tutukov 1984 (hereafter GHT). The assumptions in either case are similar. It is usually assumed that the Hα emission arises from Case B hydrogen recombination in balance with a strong ionising continuum dominated by stars in the 30 to 60 $M_{\odot}$ range. Observationally, the Hα flux can be converted to the number of Lyman continuum photons through the expression :

$$N_C = 8.78 \times 10^{61} F_C(\mathrm{H}\alpha) D^2 \tag{2.1}$$

where D is the distance to the galaxy in Mpc, and $F_C(\mathrm{H}\alpha)$ is the Hα flux in units of $\mathrm{ergs\,s^{-1}\,cm^{-2}}$ corrected for reddening. In order to derive from this a SFR it is usual to assume a fixed slope for the IMF and an upper mass cutoff. If these factors do not change from region to region in a galaxy and if, additionally, there are few or no super-massive stars present in the H II regions (e.g. Wolf-Rayet stars), then changes in Hα flux are attributed to changes in the total number of stars born per year. For example, GHT estimate that for a Salpeter IMF of the form $\Phi(M) = M^{-a}$ with $a = 2.35$ and $M_{upper} = 100\,M_\odot$, the SFR is :

$$\alpha_C = 2.5 \times 10^{-54} N_C \,\mathrm{stars\,yr^{-1}} \tag{2.2}$$

Virtually all the ionising photons are produced by 30–60 $M_\odot$ stars with lifetimes 3×10^6 yr; so formally α_C provides an instantaneous value of the SFR. Integrating over the mass range 10–100 $M_\odot$, it is easy to show that this corresponds to a SFR, measured in gas mass converted into massive (M > $10 M_\odot$) stars per year, of $0.7\alpha_C$ $M_\odot\,\mathrm{yr}^{-1}$. If all stars are included down to a lower mass cut-off of 0.1 $M_\odot$ the total SFR would equal $5.8\alpha_C\,M_\odot\,\mathrm{yr}^{-1}$. This agrees closely with the estimate by Kennicutt (1983) adopting very similar assumptions.

Table 2.1: Photometry of Arp 10 using the constant isophotal level method

Region	Area	$m_{H\alpha}$	m_R	$\sigma_{H\alpha}$	σ_R	L	SFR
#	arcsec^2	mag	mag	ergs s^{-1} cm^{-2} arcsec^{-2} in units of 10^{-16}	mag arcsec^{-2}	ergs s^{-1} in units of 10^{39}	stars Gyr^{-1} pc^{-2}
(1)	(2)	(3)	(4)	(5)	(6)	(7)	(8)
1	4.10	18.38	17.32	23.57	18.66	17.23	22.03
2	4.86	18.16	17.07	24.40	18.59	21.10	22.80
3	4.13	18.60	17.30	19.09	18.64	14.07	17.84
4	4.30	18.46	17.25	20.90	18.64	16.01	19.53
5	2.79	19.24	17.77	15.66	18.69	7.80	14.63
6	5.31	20.59	20.82	2.37	22.44	2.25	2.22
7	4.31	20.90	20.78	2.20	22.17	1.69	2.06
8	9.43	19.91	19.52	2.50	21.76	4.21	2.34
9	18.35	19.02	18.28	2.92	21.24	9.56	2.73
10	11.40	19.91	18.80	2.07	21.25	4.21	1.94
11	12.58	19.64	18.80	2.40	21.35	5.40	2.25
12	7.58	20.55	19.39	1.72	21.40	2.34	1.62
13	12.61	19.73	18.86	2.21	21.41	4.97	2.07
14	8.369	20.87	19.31	1.16	21.42	1.74	1.09
15	17.07	19.54	18.47	1.94	21.35	5.92	1.82

Table 2.1 (Continued)

Region	Area	$m_{H\alpha}$	m_R	$\sigma_{H\alpha}$	σ_R	L	SFR
#	arcsec^2	mag	mag	ergs s^{-1} cm^{-2} arcsec^{-2} in units of 10^{-16}	mag arcsec^{-2}	ergs s^{-1} in units of 10^{39}	stars Gyr^{-1} pc^{-2}
(1)	(2)	(3)	(4)	(5)	(6)	(7)	(8)
16	16.51	19.78	18.75	1.61	21.60	4.75	1.51
17	22.75	18.59	18.24	3.50	21.44	14.20	3.27
18	38.10	18.3	17.93	2.73	21.69	18.55	2.56
19	28.99	17.68	17.64	6.35	21.10	32.83	5.94
20	31.90	17.71	17.63	5.62	21.19	31.93	5.25
21	27.92	17.96	17.94	5.10	21.36	25.37	4.77
22	24.26	17.73	17.96	7.25	21.22	31.36	6.78
23	23.73	17.83	18.01	6.76	21.25	28.60	6.32
24	19.16	18.99	18.4	2.87	21.41	9.82	2.69
25	17.73	19.23	19.25	2.49	22.17	7.87	2.33
26	10.49	19.94	17.43	2.19	19.79	4.09	2.05
27	112.30	18.81	19.55	0.57	24.48	11.60	0.54
28	21.24	20.12	21.94	0.91	25.06	3.47	0.86
29	67.66	19.1	20.98	0.73	25.36	8.88	0.69
30	114.44	15.82	14.26	8.93	19.21	182.11	8.35
31	575.91	15.32	14.8	2.81	21.50	288.62	2.63

2.6 Results

The results of Method I are presented in Table 2.1. Column (1) gives the name of the region identified in Figure 2.2 and Column (2) presents the area of the region in arcsec^2. In Columns (3) and (4) we show the magnitude of the region measured through the Hα and R-band filters respectively (see § 2). In Column (5) we give the Hα surface brightness, after applying a correction for an assumed 5% contamination of the Hα flux by [N II] emission. Such a correction is consistent with the work of Kennicutt (1983) on irregular galaxies and is similar to that measured in the Cartwheel ring galaxy by Fosbury and Howarden (1976). In Column (6) we present the R-band surface brightness of each region. Both columns (5) and (6) have also been corrected for a Galactic extinction of $A_v = 0.15$ (de Vaucouleurs, de Vaucouleurs and Corwin 1976). In Column (7) we show the luminosity of each region and finally in Column (8) we present the SFR in units of $\mathrm{stars\,Gyr^{-1}\,pc^{-2}}$. We note that no correction has been made for internal extinction within the galaxy itself.

In Table 2.2 we present the results of Method II. Column (1) indicates the region identified in Figure 2.2, Column (2) presents the constant area in arcsec^2, and the Columns (3) to (6) have similar information to that of Table 2.1.

The luminosities of the H II region complexes (see Table 2.1) show a wide spread in values, ranging from approximately 3×10^{39} $\mathrm{ergs\,sec^{-1}}$ in the outer ring-arc (region 27) to 2×10^{40} $\mathrm{ergs\,sec^{-1}}$ in the inner ring (region 2). Although the regions we have evaluated probably contain more than one individual H II region (this is especially true in the bright north-western regions of Ring 2), it is interesting to note that in all cases the luminosities are comparable with the brightest H II regions seen in late-type galaxies (Kennicutt (1988)). For example, even the emission from knot 28

Table 2.2: Photometry of Ring 2, using the constant aperture method.

Region	Area	$m_{H\alpha}$	m_R	$\sigma_{H\alpha}$	σ_R
a	25.87	20.48	20.70	1.54	22.89
b	25.87	20.67	20.26	1.28	22.46
c	25.87	19.16	19.67	5.18	21.87
d	25.87	19.56	19.21	3.59	21.41
e	25.87	20.33	19.05	1.77	21.25
f	25.87	20.05	19.23	2.29	21.43
g	25.87	20.10	19.27	2.18	21.47
h	25.87	21.00	19.32	0.95	21.52
i	25.87	20.25	19.17	1.89	21.36
j	25.87	20.40	19.48	1.65	21.68
k	25.87	19.07	19.15	5.66	21.35
l	25.87	19.45	19.21	3.97	21.41
m	25.87	18.42	18.68	10.27	20.88
n	25.87	18.64	18.88	8.37	21.07
o	25.87	18.64	18.89	8.38	21.08
p	25.87	18.23	18.85	12.23	21.05
q	25.87	18.27	18.77	11.76	20.97
r	25.87	19.85	19.07	2.75	21.27
s	25.87	19.62	19.99	3.40	22.19

in the outer ring-arc has the luminosity of an average H II region observed in an Sbc or Sc galaxy.

2.7 Model Predictions for Ring Galaxies

It was demonstrated by Toomre (1978) that mildly off-center collisions between galaxies drive ring-like waves through their disks. This work was extended by ASM and SMA to include the study of the star formation response in ring galaxies. This showed that the overdensity in the ring can be used as a probe of the sensitivity of the star formation rate to the density in the ring wave. Indeed, mildly off-center collisions are shown to lead to a strong azimuthal variation in ring gas density. In Figure 2.4a we show the density distribution of an expanding ring wave driven into a disk derived from Figure 7c of ASM. We have modified the figure to include a notation which will allow us to discuss further the azimuthal dependence of the star formation rate on the ring density, using the letters A to F to indicate azimuth angles around the ring at intervals of 60 degrees. The dependence of the predicted star formation rate on the ring density (relative to the unperturbed density) is shown for two forms of star formation rate law. The first, Figure 2.4b, is derived directly from ASM Model E and as discussed in that paper, follows approximately a Schmidt law in which the SFR $\propto \rho^{1.5}$. The second law, hereafter called the "threshold" model, has a SFR which follows a Schmidt law below some critical gas surface density, but then increases rapidly above that density (see Figure 2.4c). Using the lettering system defined in Figure 2.4a to identify azimuthal position of the region around the ring, it is noted that both star formation laws exhibits systematic behavior with azimuth. In the case of the Schmidt law model, the behavior in the SFR/density domain is a loop which begins at the left of the diagram (Position A in Figure 2.4a; low density, small star formation rate), rises monotonically through the densest part of the wave (B through D) and then falls back to its initial value in the least dense part of the ring (E through F). In the case of the threshold model, similar behavior is found until the threshold is exceed, where the SFR follows a much steeper path, again forming a tight loop. The threshold model of Figure 2.4c, shows some important differences from the Schmidt-type model of Figure 2.4b. Firstly, the SFR/density relationship shows a sudden discontinuity at the critical density. This would have direct observational consequences if star formation rates and ring densities could be determined over a wide enough dynamic range on either side of the discontinuity. Secondly, because of the peculiar geometry of the off-center collision shown here, the sudden steepening of the SFR law at the critical density translates into a sudden brightening of the ring in Hα light in an arc encompassing the densest parts of the ring. For example, in Figure 2.4c, the azimuthal regions of the ring extending between points C and E in Figure 2.4a, lie well above threshold and would be emitting strongly at the wavelength of Hα (We note that point D is so luminous in this model it lies outside the range of the plotted points in Figure 2.4c). In contrast, from Figure 2.4b, it can be seen that only a small region near point D would be expected to be producing stars at a high rate. For the threshold models it is clear that the physical extent of the bright region will be strongly dependent on the value of the threshold and the strength of the density wave and will differ from one galaxy to another. It is important to note that these predictions relate only to gaseous density waves although it is expected that at least initially, the amplitude of the stellar and gaseous wave will be similar in the collisional picture. However, an early-type disk galaxy containing no cool gas is unlikely to exhibit the star formation behavior described here.

The threshold models predict that for an off-center collision, a high contrast, high star formation rate segment of the ring will develop. From Figure 2.2, it is likely that Arp 10's intermediate ring (Ring 2) fits this description well. The north-western quadrant of the ring is extremely luminous in Hα light and this will be quantified in the next section. We note also that the size of the H II regions grow suddenly in this region and this will be considered as further evidence for threshold behavior.

2.8 Evidence for a Star Formation Threshold in Arp 10

2.8.1 The Surface Brightness Properties of the Rings

In Figure 2.5 we present the Hα surface density as a function of the R-band continuum around the ring features. These data have been obtained from values taken from Table 2.1. The knots associated with the three ring structures are indicated. As one proceeds from Ring-arc 3 (outer ring-arc) to the slightly higher R-band surface brightness levels, σ_R, in Ring 2, the Hα surface brightness increases slowly with an average value of approximately 3.1×10^{-22} $\mathrm{ergs\,s^{-1}\,cm^{-2}\,pc^{-2}}$. However, as one proceeds to higher levels of σ_R, an increase in scatter of the points is observed near σ_R=21.3±0.2 mag arcsec^{-2}. Although some of the scatter is attributable to measurement error, (especially region 14), most of the scatter is due to regions 19 through 23, which are significantly more luminous (by a factor of 5 on a linear scale) in Hα light than the other regions with similar σ_R. These points correspond to the bright regions of the ring noted by Vorontsov-Velyaminov. Finally, we proceed to Ring 1 (the inner ring). Here the Hα surface brightness is well determined but the strength of the red continuum is only poorly known. This is because the ring

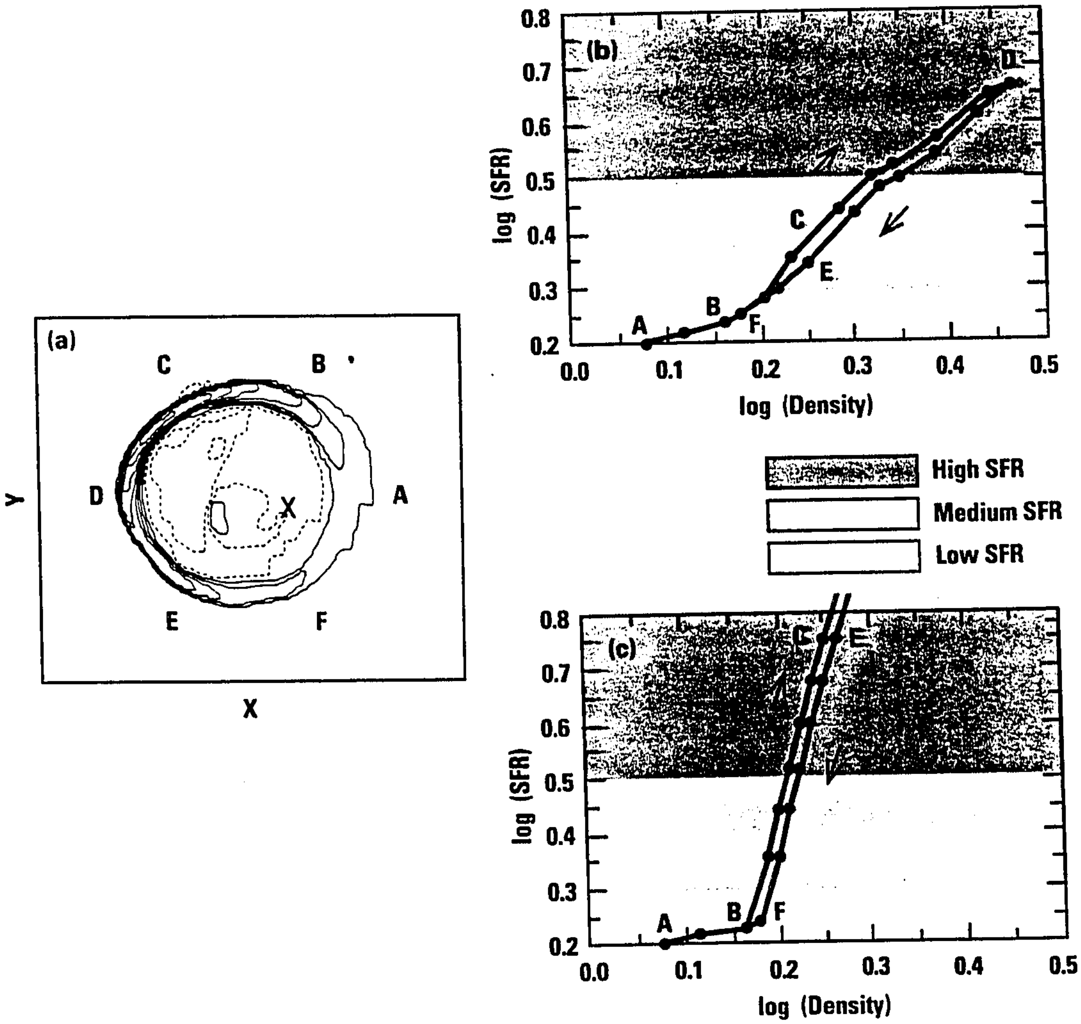

Figure 2.4: (a)The gas density distribution for an off-center ring galaxy model (Model E) from the work of Appleton & Struck-Marcell (1987). Note that the density varies with azimuth around the ring. We have labeled azimuthal positions around the ring with the letters A to F for reference. (b) The relationship between the star formation rate (SFR) and gas density for the model shown in (a). The behavior follows that of a Schmidt law (see text). The letters refer to the azimuthal positions given in (a). (c) The same relationship as in (b) but for a "threshold" star formation law. Here the SFR follows a Schmidt law below a critical density (In this case 1.5 x the unperturbed density) and then changes to a steeper form in which SFR $\propto \rho^6$ above the critical density.

is embedded in a strong central bulge which dominates the red light. We therefore accounted for the bulge contribution to the light by fitting an $R^{1/4}$ law profile to the bulge and then removing its contribution to the inner ring. Because of uncertainties in the fit to the bulge light, the surface brightness at R-band for the Ring 1 points have correspondingly large errors (see Figure 2.5). However, they do provide an important extra piece of evidence for a threshold star formation law in Arp 10 as discussed below and so we have included them for completeness in Figure 2.5.

As discussed in § 4, we repeated the surface brightness estimates for the Ring 2 using the constant aperture method (Method II). We confirmed that an increase in dispersion was observed in the Hα surface brightness at a level of 21.3 mag arcsec^{-2}, in accord with the earlier result of Figure 2.5.

2.8.2 The Possible Contamination of the R-band Light by Young Stars

Before proceeding to discuss the implications of Figure 2.5 for testing models of density wave induced star formation, we must first question the assumption that the red continuum light is dominated by old stars in the ring waves, rather than light from young star clusters. We have already noted that the distribution of R-band emission in the rings is rather smooth relative to that of the Hα emission and this fact alone argues that our continuum measurements are not strongly influenced by light from young stars. However, for the purposes of the following discussion we will adopt a "worst-case contamination" approach to the problem and assume that all of the red continuum light results from emission from underlying young stars and explore its impact on our conclusions.

If the underlying young clusters dominate the red continuum then this is likely

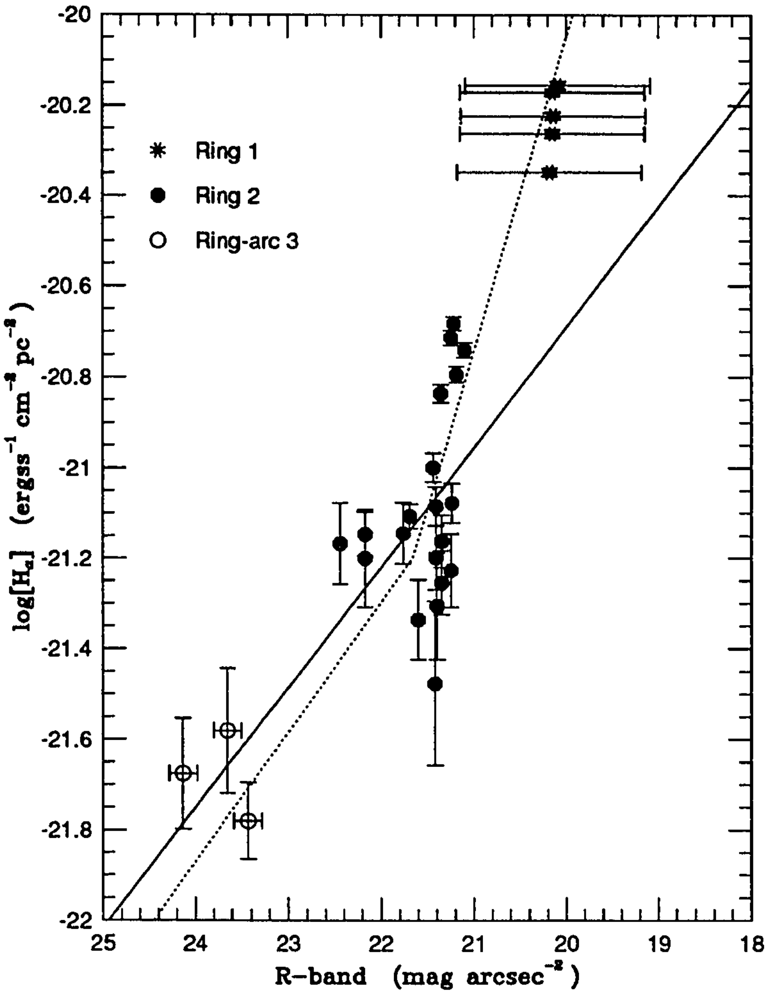

Figure 2.5: Plot of Hα versus R-band surface brightness for the constant isophote method (see Table 2.1). The different symbols indicate data for the three ring structures. Note that the large error bars for Ring 1 indicate our uncertainty in the removal of the bulge light which dominates the R-band emission for this inner ring. The solid line shows a linear fit to these data and the dotted lines show the result of a two line fit (see text).

to lead to a correlation between log(F(Hα)) and a broad-band continuum magnitude. Such a loose correlation is observed in studies of H II regions in late type galaxies (see Kennicutt and Chu (1988)). The correlation can be understood in terms of a set of self-similar clusters of increasing size in which the ratio of the Hα to continuum flux remains fixed. Assuming that all other properties of the cluster remain the same (age, metallicity, IMF) then such a set of clusters would lead to a linear correlation between log(F(Hα)) and σ_R with a slope of -0.4. Indeed we note that formally fitting a straight line to the data for Ring 2 and Ring-arc 3 yields a line with a slope close to this value (dotted line in Figure 2.5). In order to explore this possibility further, we show in Figure 2.6, the residuals of Figure 2.5 after subtracting from it the linear fit to the data. To a first approximation, the scatter in the residuals shown in Figure 2.6 might be taken to imply a good fit to the data. However, a number of important points need to be emphasized. The first is that the points 19 to 23 (corresponding to the bright H II regions in the north-western quadrant of Ring 2) lie significantly above the linear relationship, given their small observational errors. As previously stated, these points are a factor of 5 times brighter than the average for their values of σ_R. Secondly, we will show conclusively in § 7.4, that the apparent scatter in the residuals shown in Figure 2.6 for Ring 2, especially near σ_R= 21.3±0.2 mag arcsec^{-2}, arises from *systematic azimuthal changes* around the ring, not random errors in the linear relationship. This subtle point is crucial to our later argument about the nature of the enhancement of emission in the north-western quadrant of Ring 2. We will demonstrate below, that these systematic variations away from the linear fit are naturally explained within the context of the threshold star formation model. However, as the linear fit to Figure 2.5 may imply, we cannot rule out some contamination by young stars as an explanation for the increase in red light in the brighter Hα emitting regions. Even if some degree of contamination does exist from young stars, it does not invalidate the main conclusion, that the H II regions observed in regions 19–23 of Figure 2.2 are unusually bright as compared with other H II regions with the same R-band continuum. [1]

2.8.3 Density Wave Induced Star Formation

Another equally valid way of interpreting Figure 2.5 is to assume that Arp 10 is a collisional ring galaxy in which density waves are driven through its disk. The slow decline in σ_R as one proceeds from inner Ring 1 radially outward to the outer rings would be explained as a consequence of the decreasing strength of the density waves with radius. If we further assume that the stellar ring density can be used to measure the gas density in the expanding wave (see § 7.6), then Figure 2.5 can be used as a diagnostic of the various forms of star formation law discussed in § 6. For example, deviations from a simple linear relation in Figure 2.5, can be interpreted as deviations from a Schmidt law behavior. We have already pointed out in § 7.2, that systematic deviations of this kind do exist. We will now investigate the possibility that these deviations are evidence for a threshold star formation picture.

The evidence for a SFR threshold law in Arp 10 depends on two things. The first

---

[1] Another approach to the question of contamination of the R-band flux from the underlying host cluster would have been to predict the expected contribution to the R-band emission based on the strength of the Hα flux. In order to do this we would have had to assume values for the IMF, the metallicity and the age of the clusters and use a color evolution model to predict the expected R-band continuum. We believe that although such models exist for solar abundances, the reliability of such models, especially the treatment of the giant and supergiant stars is still quite questionable. We therefore preferred to make use of the rough correlation derived from observations.

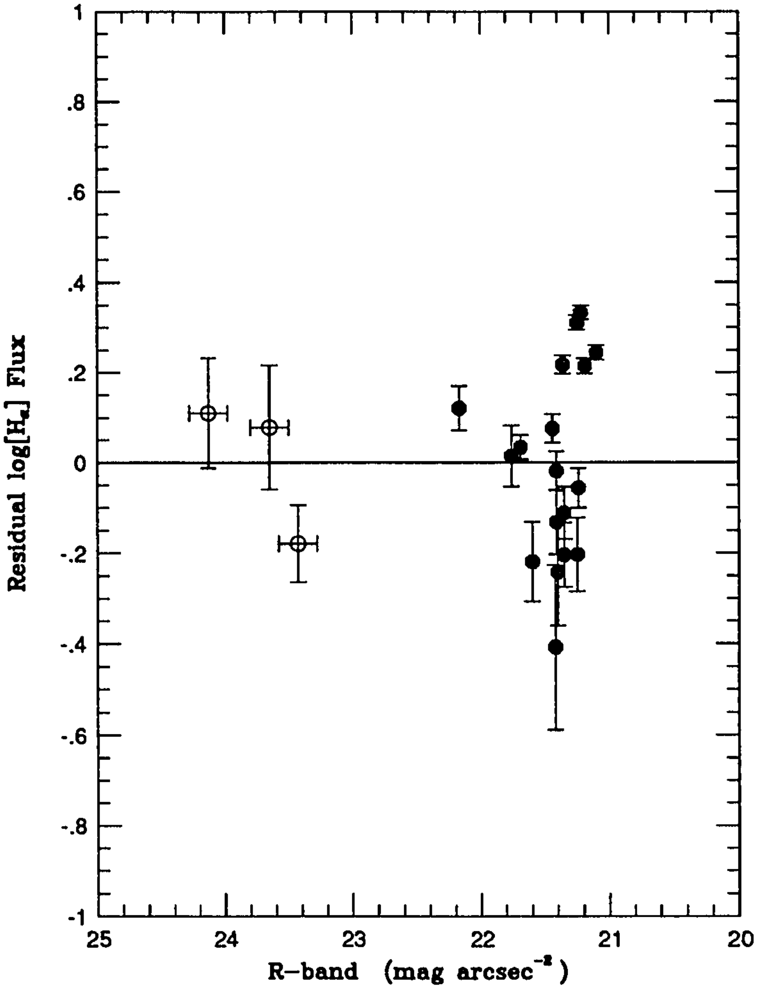

Figure 2.6: Plot of the residuals from Figure 2.5 after the subtraction of the linear fit through the points of Ring 2 and Ring-arc 3.

is our ability to recognize a discontinuity in the SFR versus ring density relationship consistent with our model predictions and the second is that such a discontinuity should exhibit the azimuthal variations predicted for the off-center collisional model. As was stated earlier, the former problem is one of dynamic range. Within any one ring, the dynamic range in the star formation rate is relatively small, despite the apparently bright regions in Ring 2 discussed earlier. Arp 10 provides a useful probe of star formation mechanisms because its three rings sample a wide range of densities, from the weak outer Ring-arc 3 to the more overdense inner rings.

One simple method of finding a sudden discontinuity in the data similar to that of Figure 2.4c is to split the data presented in Figure 2.5 into two equal sets ordered by the Hα flux and independently fit a straight line to them. As long as the discontinuity lies somewhere near the center of gravity of the data then two lines of markedly different slope would be found. On the other hand, if the same slope is found for both lines, then this would argue for a continuous function of Hα emission with continuum light. In Figure 2.5 we show the result of fitting two straight lines to the data for all three rings using a Gauss-Markov elimination method. The method depends critically on good sampling of points on either side of the discontinuity. The only restriction to the fitting procedure was that the crossing point of the two lines should occur somewhere within the body of these data. Despite the very uncertain values for σ_R in Ring 1 (giving these points lower weight), there is evidence for a discontinuous form to the data presented in Figure 2.5 since the fitted lines do have different slopes. The intersection between the two lines occurs at around σ_R= 21.2 mag arcsec^{-2} which is similar to the surface density at which the increase in dispersion was noted in the Ring 2 emission alone. As long as it is valid to treat all three rings together, the evidence suggests a threshold star formation law similar to that discussed in § 6.

The increase in Hα surface brightness at the R-band threshold of 21.3±0.2 mag arcsec^{-2} is most easily interpreted as a threshold in the massive SFR. Using the values for the knots presented in Table 2.1, we plot, in Figure 2.7, the SFR per square parsec as a function of the red continuum surface density. The discontinuity in Hα surface brightness translates, under these assumptions, into a sudden change in SFR. The rates change from an average of 0.5–1.5 stars Gyr^{-1} pc^{-2} (or 2.9–8.7 $M_{\odot}$ Gyr^{-1} pc^{-2}) in the fainter outer ring-arc and the faint southern sections of Ring 2 to values which rise to 2–6 stars Gyr^{-1} pc^{-2} (or 11–30 $M_{\odot}$ Gyr^{-1} pc^{-2}) in the bright north-west portion of Ring 2. Higher star formation rates of approximately 20 stars Gyr^{-1} pc^{-2} (or 116 $M_{\odot}$ Gyr^{-1} pc^{-2}) are found for Ring 1. We compare these values with Caldwell et al (1991) who found rates of $< 0.4\, M_{\odot}$ Gyr^{-1} pc^{-2} for early type spirals and values of 4–20 $M_{\odot}$ Gyr^{-1} pc^{-2} for Sc type galaxies. The local SFR in the inner ring appears to be extremely large, while those in Ring 2 appear to be similar to local SFR of Sc galaxies.

2.8.4 Azimuthal Variations in Ring 2

Much of the foregoing argument for a threshold dependence of star formation rate on ring strength is based on the assumption that all three rings are generated by a similar dynamical process. However, if Ring 1 was formed, for example, at an inner Lindblad resonance by some other process, then our argument for a threshold star formation law would be weakened. Nevertheless, there is evidence in Ring 2 alone, for threshold behavior. We have already discussed in § 7.2 the unusually

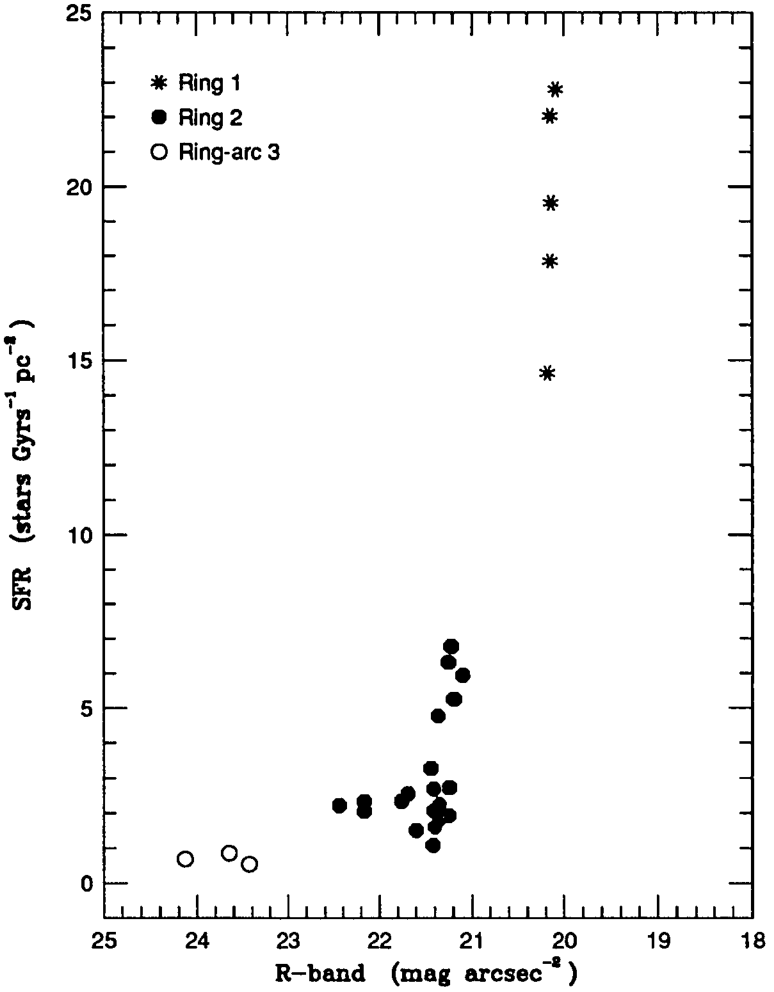

Figure 2.7: Plot of the SFR in the three ring structures, in units of stars Gyr^{-1} pc^{-2}, versus the R-band surface brightness for the constant isophote method (see Table 2.1). Note that the uncertainties in the Ring 1 points are identical to those shown in Figure 2.6.

bright star forming complexes in the north-western quadrant of Ring 2. We will now show that the azimuthal variations in the strength of the star formation is very similar to that expected from the models of Figure 2.4. In Figure 2.8 we show an enlarged version of the Ring 2 data presented in Figure 2.7. Unlike the earlier figure, Figure 2.8 connects the points with increasing azimuth. The number associated with each point represents the knot number identified in Figure 2.2. It is clear from Figure 2.8, that a strong azimuthal trend is evident as the star formation rate increases in the north-western quadrant and these data resemble the results predicted in Figure 2.4c. This systematic behavior in the star formation rate as a function of azimuth provides a good indication that the star formation rate is being controlled by a global phenomenon and is not a stochastic process. This confirms our earlier statement that the deviations of the H II regions 19–23 from the linear correlation shown in Figure 2.5 are inconsistent with a random noise process.

2.8.5 The Size of the H II Regions

There is an independent piece of evidence that a threshold process may have changed the nature of the star formation in the overdense region of the ring. In a study of H II regions in galaxies of various Hubble types, Kennicutt (1988) and Strobel, Hodge and Kennicutt (1991) demonstrated that there was a well defined relationship between the size of an extragalactic H II region and its luminosity in the Hα line. Kennicutt chose to define the "characteristic size" of an H II region in an external galaxy as the diameter of the Hα emission contour defined by the level 2×10^{-16} ergs s^{-1} cm^{-2} $arcsec^{-2}$. It was shown that the size increased monotonically with the flux from the H II regions in approximate accord with simple arguments concerning

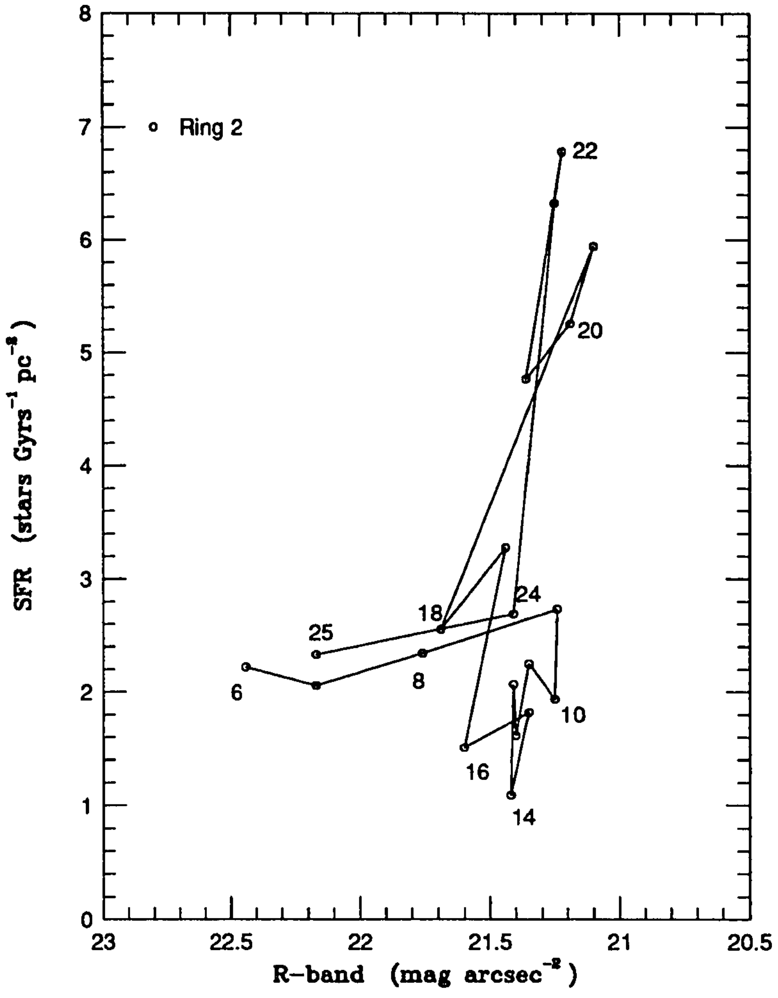

Figure 2.8: The azimuthal behavior of the SFR and R-band continuum for Ring 2. The numbers refer to the Hα emitting regions identified in Figure 2.2 and increase numerically as a function of increasing position angle around the ring. We observe the striking similarity with the threshold model shown in Figure 2.4c.

the size of the Strömgren sphere. In Figure 2.9, we show a contour map of the Hα emission at the level of 2×10^{-16} ergs s^{-1} cm^{-2} $arcsec^{-2}$. What is striking about the map is that the majority of the H II regions which lie below the "threshold" value of R-band flux (Knots 6–16 in Figure 2.2) have angular sizes which are barely or just resolved on at the level of a few arcsec. However, as one approaches the north-western segment of the Ring 2, the H II regions suddenly grow in size until they merge together to form one continuous structure which includes most of the very active parts of the second ring and all of the first ring. It appears that on the basis of the size of the H II regions alone, there is evidence for some form of transition from small to large H II regions which is consistent with our photometric result. Both observational facts indicate that a threshold star formation process is operating in this galaxy.

2.8.6 Consequences for Other Star Formation Threshold Models

We have presented evidence that suggests that the amplitude of the stellar density wave in Ring 2 is a controlling influence in the processes of star formation in the ring. At some critical (threshold) surface density in the red starlight, a change occurs in the properties of the H II regions. The changes are consistent with a sudden increase in star formation rate. We will now discuss possible ways in which such changes may come about in the context of models of star formation in external galaxies.

Kennicutt (1989) has presented convincing evidence for a star formation threshold in a sample of normal disk galaxies. By combining information about the total gas surface density derived from CO and H I measurements, Kennicutt was able to

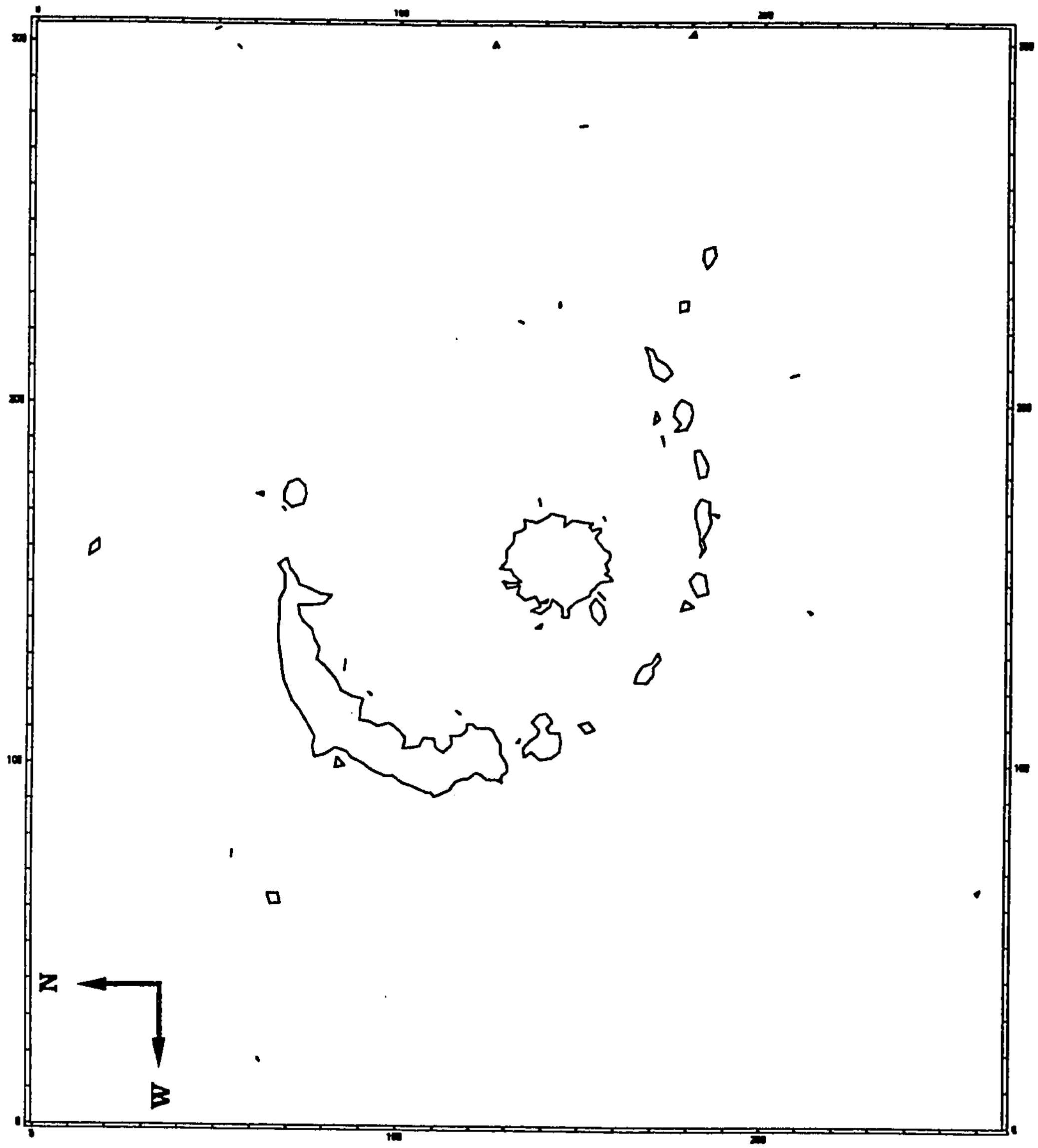

Figure 2.9: A contour map of the Hα emission at the level of 2×10^{-16} ergs cm^{-2} arcsec^{-2}. This isophotal level was used by Kennicutt (1988) to define the “characteristic size” of an ″ II region. Note that the H II region complexes suddenly grow in size in the bright (north-west) region of Ring 2.

demonstrate that massive star formation ($M > 10\,M_{\odot}$) occurs mainly in regions of the disk which lie above a critical gas surface density. The form for the critical density follows from a stability analysis of a thin self-gravitating disk applied to the gaseous component (Toomre 1964, Goldreich and Lynden-Bell 1965). Kennicutt found that in regions above the gas density threshold, the star formation law followed a Schmidt type form (SFR $\propto \rho^n$ with $n \simeq 1.3$), whereas below the threshold, little or no massive stars were being formed.

Firstly, we point out that our observations of Arp 10 cannot be directly compared with the work of Kennicutt unless we make some assumptions about the nature of the rings. We do not yet have information about the distribution of H I or CO observations in this galaxy and therefore we cannot directly compare the star formation rates in the rings to the gas surface densities. However, we can appeal to our theoretical understanding of the ring galaxy phenomenon to help restrict the range of possibilities.

If Arp 10 is a colliding ring galaxy, then the stellar surface density in the ring will be a lower limit to the surface density in the gas component. For example, in the absence of self-gravity in the gas, the density profile of the expanding ring perturbation would closely track that of the stars since both gas and stars are crowded into the density wave (see SMA). In this simplified case, a measurement of the old stellar surface density would be equivalent to a measurement of the gas surface density in the ring. Even in the case where hydrodynamic effects begin to dominate in the gas phase, the strength of the stellar density wave will provide a lower limit to the density in the gas. In general, whereas the gas will tend to occupy a smaller volume than the old disk stars in the wave, the inverse is unlikely to be true.

Since we do observe H II regions in all three rings we conclude that the rings must have already exceeded Kennicutt's critical density over most of their area. However, the marked increase of the Hα flux in the north-west quadrant of Ring 2 suggests that in colliding systems the star forming behavior is more complicated. In particular, the existence of a threshold that depends on the strength of the density wave may provide evidence for a breakdown of the linear instability model which appears to provide a good description of star formation in isolated galaxies. This may not be surprising, since strong gravitational interactions and collisions are expected to drive highly non-linear behavior in galaxies.

2.8.7 Global Star Formation Rate in Arp 10

Under the same assumption as in Section § 7.1, we can calculate the total SFR in the galaxy, including the two rings, the ring-arc and the nuclear emission. The resulting SFR is approximately 0.94 $\mathrm{stars\,yr^{-1}}$ (or 5.4 $M_{\odot}\,\mathrm{yr}^{-1}$). Compared with a typical late-type galaxy, this overall SFR is at the low end of the distribution (GHT; Caldwell et al 1991). This contrasts with the high local SFR within the rings themselves. The apparent paradox is a result of the narrowness of the rings. In comparison, a typical Sc galaxy would have H II regions of similar luminosity to Arp 10, but would be distributed over a larger area of the disk.

2.8.8 IMF Variations ?

There is another way we can interpret the elevated Hα fluxes in the overdense regions without invoking a change in the star formation rate. An equally plausible way of increasing the number of Lyman continuum photons in the "active" regions would be to modify the IMF in those regions. Since the number of Lyman continuum photons N_C in all H II regions is mainly produced by stars in the 30 to 60 $M_\odot$ region, small changes in the slope of the IMF can lead to quite large differences in the N_C. For example in order to increase N_C (and therefore by implication $\sigma_{H\alpha}$) by a factor of 4–5 one only has to flatten the slope of the IMF from a value of 2.35 to 1.95 (assuming an upper mass cut-off of 100 $M_\odot$). This is sufficient to explain the sudden increase in the Hα emission in the overdense regions of Ring 2. However, if the same process is to give rise to much brighter fluxes seen in the inner ring, the slope would have to be modified substantially from 2.35 to 1.55. As discussed by Kennicutt (1983), such large changes in the IMF slope would have noticeable consequences for the broad-band colors of star formation regions. Since we do not yet have multicolor images of Arp 10, the possibility that changes in IMF slope can explain the higher Hα fluxes in the overdense regions cannot be ruled out. The slope of the IMF though, is not the only parameter that can produce this result. If the upper mass cut-off is smaller than 60 $M_\odot$, then this has a direct impact to the number of Lyman continuum photons produced. It has been assumed that $M_{upper} = 100\,M_\odot$. However recent observations (Doyon, Puxley and Joseph 1992) indicate that there are galaxies with $M_{upper} < 40\,M_\odot$. It is not clear what physical mechanism could modify the IMF in the dense parts of the ring-wave.

2.9 Conclusions

We have performed CCD imaging of the peculiar galaxy Arp 10 and have drawn the following conclusions from our observations.

- Arp 10 is shown to contain two massive-star forming rings and an outer star forming ring-arc indicating that star formation is occurring concurrently on a variety of scales. The morphology of Arp 10 is consistent with that of a colliding ring galaxy. We identify a possible small elliptical companion galaxy which lies on the minor axis of Ring 2, which may be the intruder galaxy.

- The strength of the Hα emission in the rings covers a wide range of Hα surface brightness, ranging from extremely luminous in the inner ring (comparable to the most luminous H II regions in the late-type spiral galaxies) to rather faint H II regions in the outer ring-arc (comparable to the most luminous H II regions seen in Sa type galaxies).

- We present evidence for a sudden change in the properties of the ring H II regions as a function of the strength of the underlying stellar density wave. These are:

  a) Taking the three ring structures together, there is evidence for a discontinuous relationship between the logarithm of the Hα surface brightness and the strength of the R-band continuum surface density which support a threshold star formation model. We interpret the sudden increase in Hα emission at a σ_R of 21.3 ± 0.2 mag arcsec^{-2} as either a sudden increase in the SFR or a change in the IMF at a critical matter density in the ring. In either case, the result suggests that the star formation properties are being controlled by the amplitude of the stellar surface density in the ring.

  b) The proposed critical threshold value in σ_R falls within the range spanned by Ring 2. At this apparent threshold level, the star formation properties show a large dispersion, due mainly to an increase by a factor of 5 in the star formation rates in the north-western quadrant of the ring. This is the same quadrant of the ring which was noted as unusual by Vorontsov-Velyaminov (1977). The azimuthal variations of both star formation rate and R-band light show remarkable similarity with model predictions for off-center ring galaxy in which a threshold star formation law holds.

c) The size of the H II regions are observed to grow suddenly in the region of the enhanced star formation discussed in b) above, again supporting the proposed threshold picture.

- The results indicate that the star formation behavior may differ from that of a normal quescient disk system as a result of the existence of strong non-linear waves induced in the disk by a collision. A full comparison with the gas density threshold models of Kennicutt (1989; 1990) will require observations of the cool gas content of the three star forming rings.

2.10 Acknowledgments

We thank C. Struck-Marcell (Iowa State University) for stimulating discussions and L. Fontaine (Graphic Design, ISU) for advice and help regarding Figure 2.4. The authors would like to thank J. J. Eitter (Iowa State University) for invaluable help at all stages of the observations at the Fick Observatory, and G. Aldring (U. of Minnesota) for providing the design for the f/4 focal reducer. PNA wishes to thank the Department of Physics and Astronomy for providing travel funds to KPNO. The authors are grateful to an anonymous referee for suggesting some significant

improvements to the paper.

2.11 Appendix

In this section we compare the R-band image of Arp 10 taken at KPNO with the one that we took at Fick Observatory, as a further check that it has no contamination by hydrogen emission lines. Since the two images had different resolution we convolved them with a gaussian profile down to an effective resolution of FWHM $=$ 3.3 arcsec. A contour graph of each image is presented in Figures 2.10 and 2.11. Our calculations of the intensity distribution along Ring 2 in both images showed that there was no discernible difference between the two, down to a level of$<$ 5%.

2.12 References

Appleton, P. N., & Struck-Marcell, C. 1987, ApJ, 312, 382 (ASM)

Arp, H. C. 1966, Atlas of Peculiar Galaxies (Pasadena: California Institute of Technology)

Caldwell, N., Kennicutt, R., Phillips, A. C., & Schommer, R. A. 1991, ApJ, 370, 526

Carignan, C., & Beaulieu, S. 1989, ApJ, 347, 760

Dahari, O. 1985, ApJs, 57, 643

de Vaucouleurs, G., de Vaucouleurs, A., & Corwin, H. G., Jr. 1976, *Second Reference Catalog of Bright Galaxies* (Austin: University of Texas Press)

Doyon, R., Puxley, P. J., & Joseph, R. D. 1992, ApJ, 397, 117

Gallagher, J. S., Hunter, D., & Tutukov, A. 1984, ApJ, 284, 544 (GHT)

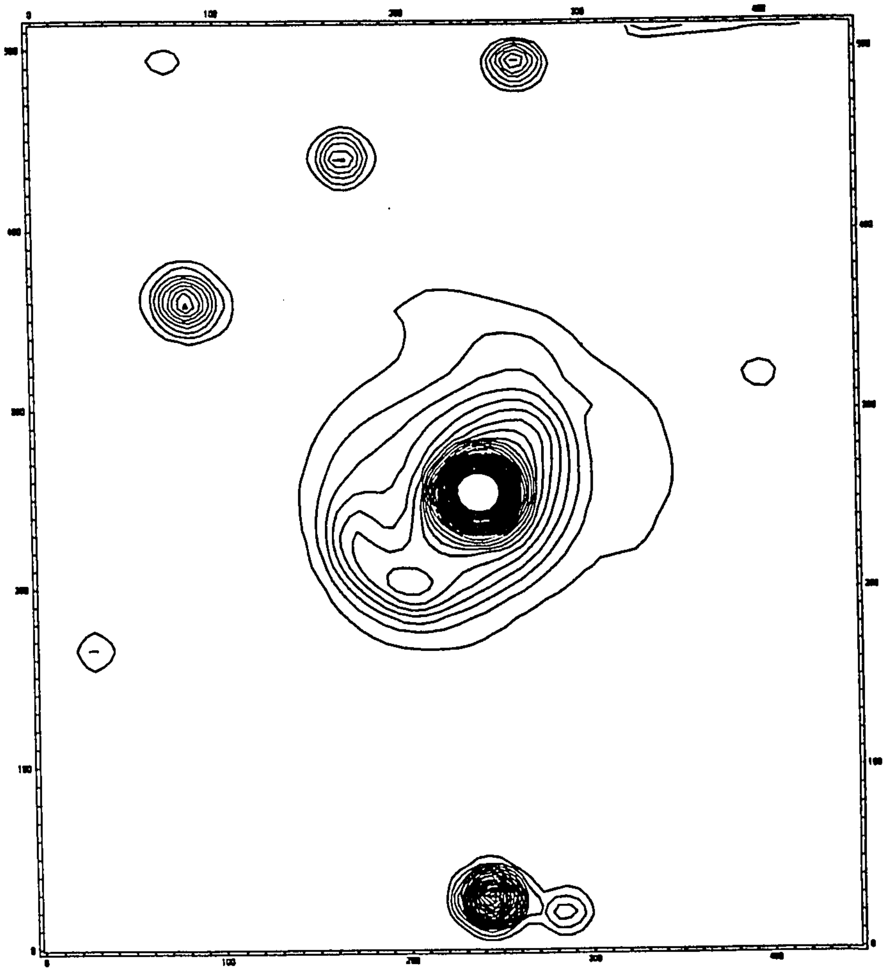

Figure 2.10: A contour map of the KPNO image presented at Figure 2.1 after convolution with a gaussian profile. The resulting effective resolution is 3.3 arcsec (FWHM).

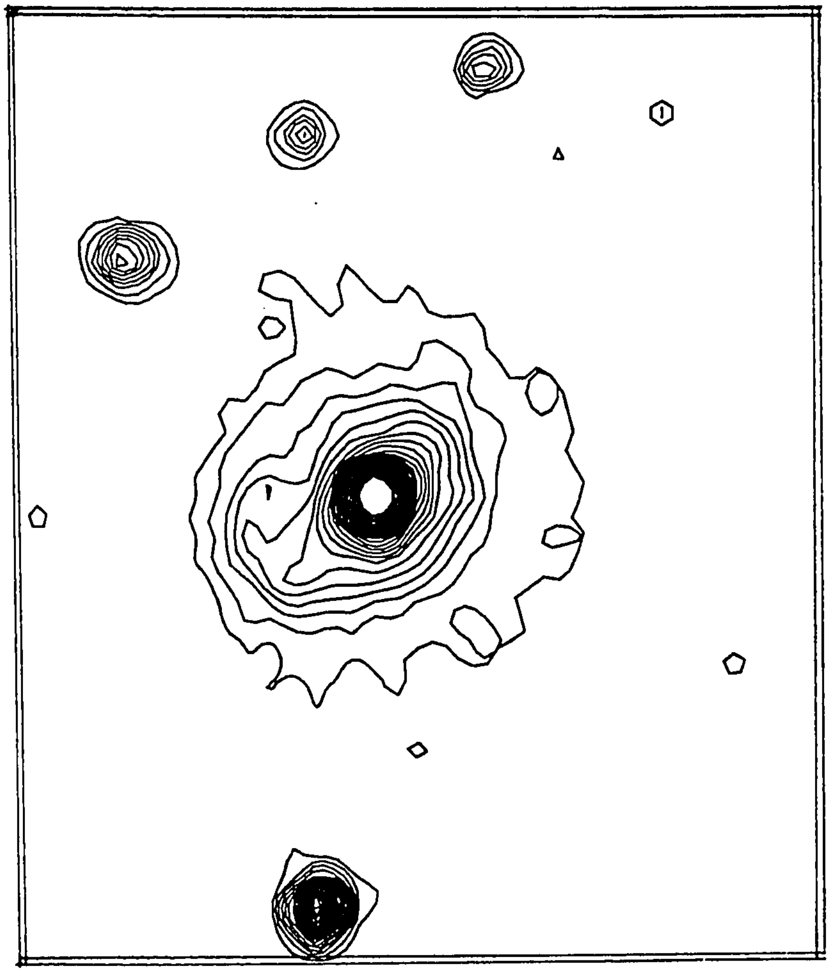

Figure 2.11: Contour map of the Fick Observatory CCD image obtained through a narrow-band filter. The filter is shifted with respect to Hα emission line and as a result is completely free of any possible line contamination (see text). Note the strong similarities (down to a level of $< 5\%$) between this image and Figure 2.10.

Goldreich, P., & Lynden-Bell, D. 1965, MNRAS, 130, 97

Kennicutt, R. 1983, ApJ, 272, 54

Kennicutt, R. 1988, ApJ, 334, 144

Kennicutt, R. 1989, ApJ, 344, 171

Kennicutt, R. 1990, in *The Interstellar medium in Galaxies*, eds. H. A. Thronson, Jr., & J. M. Shull, (Dordrecht: Kluwer), p. 127

Kennicutt, R. 1991, ApJ, 370, 526

Kennicutt, R., & Chu, Y.-H. 1988, AJ, 95, 720

Landolt, A. U. 1983, AJ, 88, 439

Lynds, R., & Toomre, A. 1976, ApJ, 209, 383

Malin, D. F., & Carter, D. 1983, ApJ, 274, 534

Scalo, J. M., & Struck-Marcell, C. 1984, ApJ, 276, 60

Scalo, J. M., & Struck-Marcell, C. 1986, ApJ, 301, 77

Schombert, J. M., & Bothun, G. D. 1988, AJ, 95, 1389

Skillman, E. D. 1987, in *Star Formation in Galaxies*, ed.C. Lonsdale, (NASA Publ. 2466), p. 267

Stone, R. 1977, ApJ, 218, 767

Struck-Marcell, C., & Appleton, P. N. 1987, ApJ, 323, 480 (SMA)

Struck-Marcell, C. 1990, AJ, 99, 71

Strobel, N. V., Hodge, P., Kennicutt, R. C. 1991, ApJ, 383, 148

Sulentic, J. W., & Arp, H. 1983, AJ, 88, 489

Theys, J. C., & Spiegel E. A. 1977, ApJ, 212, 616

Toomre, A. 1964, ApJ, 139, 1217

Toomre, A. 1978, in *IAU Symposium 79, The Large Scale Structure of the Universe*, ed. M. S. Longair & J. Einasto (Dordrec ht: Reidel), p. 109

Vorontsov-Velyaminov, B. A. 1977, Atlas of Interacting Galaxies, A&AS, 28, 1

CHAPTER 3.

THE NEUTRAL HYDROGEN DISK OF ARP 10 (=VV 362) : A NON-EQUILIBRIUM DISK ASSOCIATED WITH A GALAXY WITH RINGS AND RIPPLES

A paper submitted to The Astrophysical Journal (To appear on April 1, 1996)

Vassilis Charmandaris and Philip N. Appleton

3.1 Abstract

We present VLA[1] H I and optical spectra of the peculiar galaxy Arp 10. Originally believed to be an example of a classical colliding ring galaxy with multiple rings, the new observations show a large disturbed neutral hydrogen disk extending 2.7 times the radius of the bright optical ring. We also present evidence for optical shells or ripples in the outer isophotes of the galaxy reminiscent of the ripples seen in some early type systems. The small elliptical originally believed to be the companion is shown to be a background galaxy. The H I disk consists of two main parts: a very irregular outer structure, and a more regular inner disk associated with the main bright optical ring. In both cases, the H I structures do not exactly trace the optical

---

[1] The Very Large Array is operated by Associated Universities Inc. under cooperative agreement with the National Science Foundation.

morphology. In the outer parts, the H I distribution does not correlate well with the optical ripples. Even the inner H I disk does not correspond well morphologically nor kinematically to the optical rings. These peculiarities lead us to believe that the potential in which the H I disk resides is time varying — a situation which would inherently produce rings of star formation. We suggest that Arp 10 is the result of the intermediate stage of a merger between a large H I rich disk and a gas-poor disk system. As such, it may represent an example of a class of mergers which lies intermediate between the "ripple and shell" accretion systems and the head-on collisional ring galaxies.

3.2 Introduction

Arp 10 (= VV 362) is a galaxy containing a bright ring, an off-center nucleus and a faint bar. These features can be easily detected in the photograph presented in the Arp Atlas of Peculiar Galaxies (Arp 1966), suggesting that Arp 10 may be a colliding ring system. This galaxy was chosen as part of a larger study of the dynamics and star formation properties of ring systems (See Appleton and Struck-Marcell,1995 for review).

Recent deep CCD imaging of the galaxy in Hα and R–band by Charmandaris, Appleton and Marston 1993, hereafter CAM, revealed, in addition to the bright ring, an very small inner ring and traces of outer ring arcs. The earlier observations also provided evidence for threshold behavior of the star formation rate along the rings. In that paper we suggested that Arp 10 may be an example of a collisional ring galaxy, in which rings are produced as a result of the passage of a small galaxy through the center of a larger rotating disk (Lynds and Toomre 1976).

Deep broad-band imaging by Appleton and Marston (1995) now show that, in addition to the bright inner rings, the galaxy exhibits faint optical structure reminiscent of shells or "ripples" seen around some early type galaxies (e.g. Schweizer and Seitzer 1988; hereafter SS88). A reproduction of the B–band image of Arp 10 is shown in Figure 3.1. The fact that Arp 10 shows both "ripples" and rings suggests a formation history which may be intermediate between a classical ring galaxy and a merger/mass transfer event which is thought to responsible for most "ripples" or shells (Quinn 1984, Dupraz & Combes 1986, Hernquist and Quinn 1987). The discovery of an extra-nuclear knot by CAM $5''$ to the southwest of the nucleus of Arp 10 (see also Figure 3.9 of this paper) lends further support to the idea that Arp 10 is some form of merging system, since the knot might be the nucleus of a second galaxy. The study of the morphology and kinematics of the H I in this system is therefore of considerable interest in the search for a complete explanation for the formation of rings and shells, but also for the ultimate fate of gas in such systems.

The single dish H I spectrum of the galaxy obtained by Sulentic and Arp (1983; hereafter SA) using the Arecibo radio telescope, exhibits the typical two-horned profile of a rotating planar disk. It was assumed that such a disk would be associated with the bright optical ring.

In order to further study the kinematics of the system we obtained medium resolution H I observations of Arp 10 using the C-array of the Very Large Array. We present a detailed mapping of the galaxy and provide a more complete picture of the internal kinematics of its gaseous content. In § 2 we describe our observations and in § 3 we present the global H I characteristics of the system. In § 4 we elaborate on the H I distribution and the kinematics of the galaxy. In § 5 we present the longslit

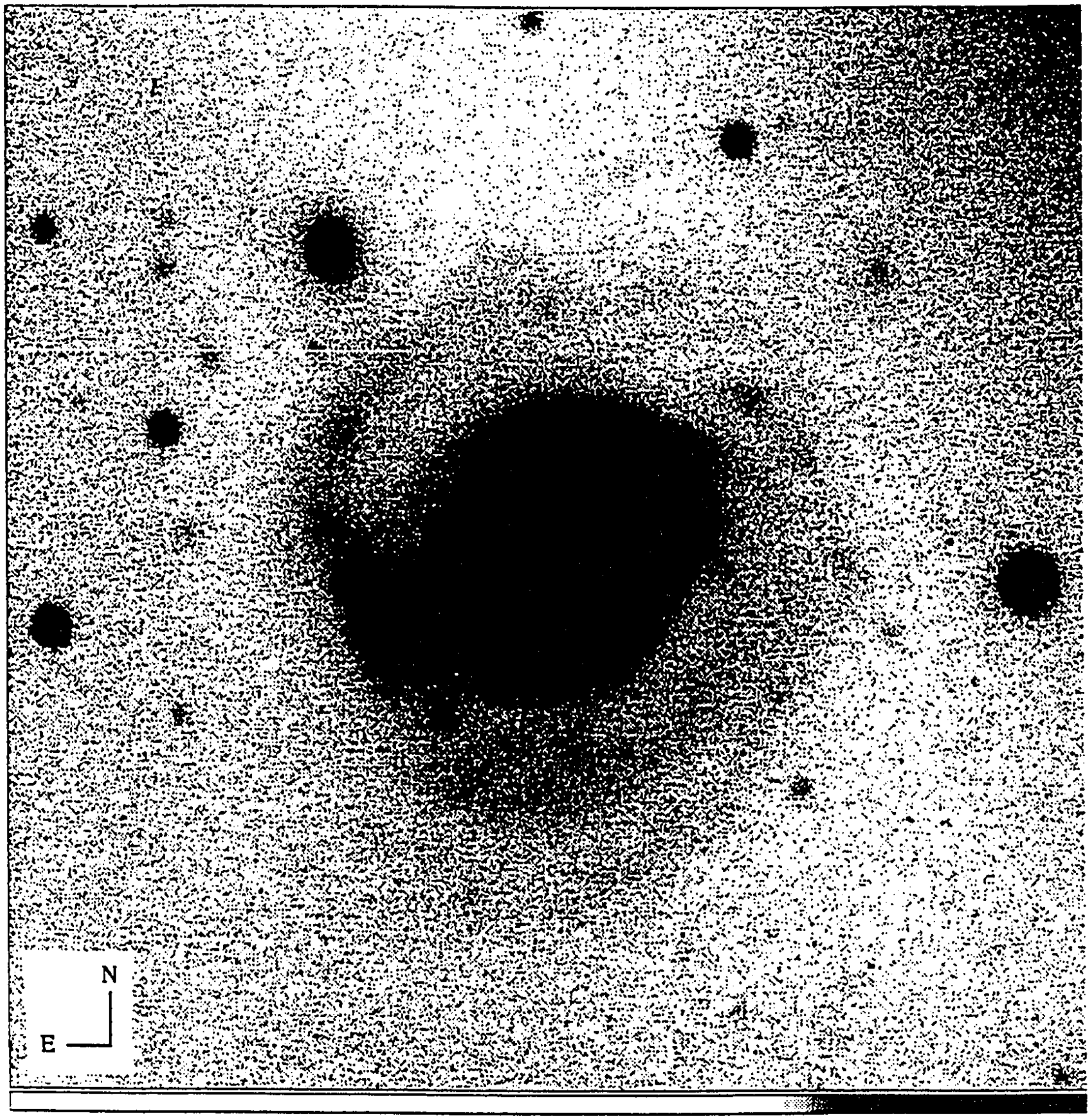

Figure 3.1: Greyscale image of Arp 10 through the B–band filter. Note the faint "ripples" at the south and the well defined loop at the northeastern side of the galaxy.

spectral observations and in § 6 we examine the plausible scenarios that could lead to the formation of this system. Finally, in § 7 we present our conclusions.

We assume throughout this paper a distance to Arp 10 of 121 Mpc, based on a heliocentric velocity for Arp 10 of 9108 $\mathrm{km\,s^{-1}}$ (this paper) and a Hubble constant of 75 $\mathrm{km\,s^{-1}Mpc^{-1}}$.

3.3 Observations

The observations were made on December 4 1994, using all 27 telescopes in the C-array of the VLA. We used a bandwidth of 3.125 MHz centered at 9,104 $\mathrm{km\,s^{-1}}$, the heliocentric optical velocity of the galaxy. The correlator was set in the 2AC mode with on-line hanning smoothing and 64 channels. This provided a frequency separation of 48.8 kHz per channel, which corresponds to 10.94 $\mathrm{km\,s^{-1}}$ in the rest-frame of the galaxy using the optical definition of redshift. The velocity coverage of our observations was 689 km $\mathrm{s^{-1}}$. A total of 4 hours 53 min was spent on source. Flux and phase calibration was achieved using the sources 3C48 and 0202+149 (1950) respectively.

These data were first amplitude and phase calibrated and bad data due to interference were flagged and ignored by the AIPS software. Two separate image cubes were created from the UV data using the AIPS task HORUS. The first image cube (hereafter cube-1), was created by giving more weight to those baselines which sampled the uv plane more frequently (so-called natural weighting). This provided a synthesized beam with a FWHM of $21.5'' \times 20.2''$. For the second (hereafter cube-2) we used the uniform weighting scheme, which gives equal weight to every sampled uv datum. This provided a smaller beam (FWHM of $13.8'' \times 12.2''$) but was less sensitive to extended emission. In this paper we will present the results from cube-1. We analyzed, for completeness, the data for cube-2 and the results were consistent with those derived from the study of cube-1. An inspection of the channel maps of cube-1, showed that there was H I emission from 27 channels covering the velocity range 8,961 to 9,246 $\mathrm{km\,s^{-1}}$.

The subtraction of the continuum emission in each line map was performed using a standard interpolation procedure based on nine continuum maps free from H I at each end of the band. The channel maps were corrected for the effects of the sidelobes of the VLA using the CLEAN procedure described by Hogbom (1974), down to a level of 1.5 times the rms noise. The resulting delta functions were restored with a Gaussian shaped beam of dimensions $21.0'' \times 21.0''$ for cube-1 and $13.0'' \times 13.0''$ for cube-2.

In order to determine the total H I distribution we used the following technique on cube-1 which was the most sensitive in extended emission. Initially, we smoothed all channel maps to a resolution $42.0'' \times 42.0''$. New maps were formed comparing, pixel for pixel, the original full resolution maps to the smoothed ones. The pixel values of original maps were copied to the new ones only if the signal-to-noise ratio of the smoothed map at that point exceeded 2. The total H I surface density map was produced by adding the new maps all together. The same technique was used to create the first and second moment maps of the distribution. Using this procedure we effectively give more weight to points associated with low surface brightness emission.

Optical spectra of Arp 10 were obtained on the nights of 28 and 29 of November 1992. Further spectra were made of the the apparent elliptical companion companion by P. N. Appleton and C. Winrich (Winrich and Appleton 1995) under nonphotometric conditions on the night of January 30 1995. All optical spectra were obtained using the Goldcam spectrograph at the KPNO 2.1 m telescope and a full description of these observations will be presented elsewhere. The spatial resolution of the spectra was 1.56 arcsec pixel^{-1} and the dispersion 1.52 Å pixel^{-1}.

3.4 Global Profile and H I Distribution

The integrated H I profile of Arp 10, is presented in Figure 3.2. The two-horned profile of a rotating disk is well defined. The integrated flux density $\int S(V)dV$ detected by SA using Arecibo was 3.1 Jy km s^{-1}. Our observations detected 2.75 Jy km s^{-1} which accounts for 89% of the total emission quoted by SA. There is a small asymmetry in our profile with the left (low velocity) horn broader and with smaller peak flux value than the right (high velocity) one. This is opposite to the one appearing in the spectrum of the single dish observations (Figure 1 of SA). These differences, though small, may relate to the fact that the C-array is not sensitive to all the flux in the source. We are clearly missing approximately 10% of the flux seen in the single dish data. On the other hand, small differences in the pointing of the Arecibo telescope relative to the kinematic center of the galaxy could account for the differences in the line shapes.

Assuming that the gas is optically thin, the total H I mass M_H, can be calculated using the relation,

$$M_H/M_\odot = F_H D^2 \tag{3.1}$$

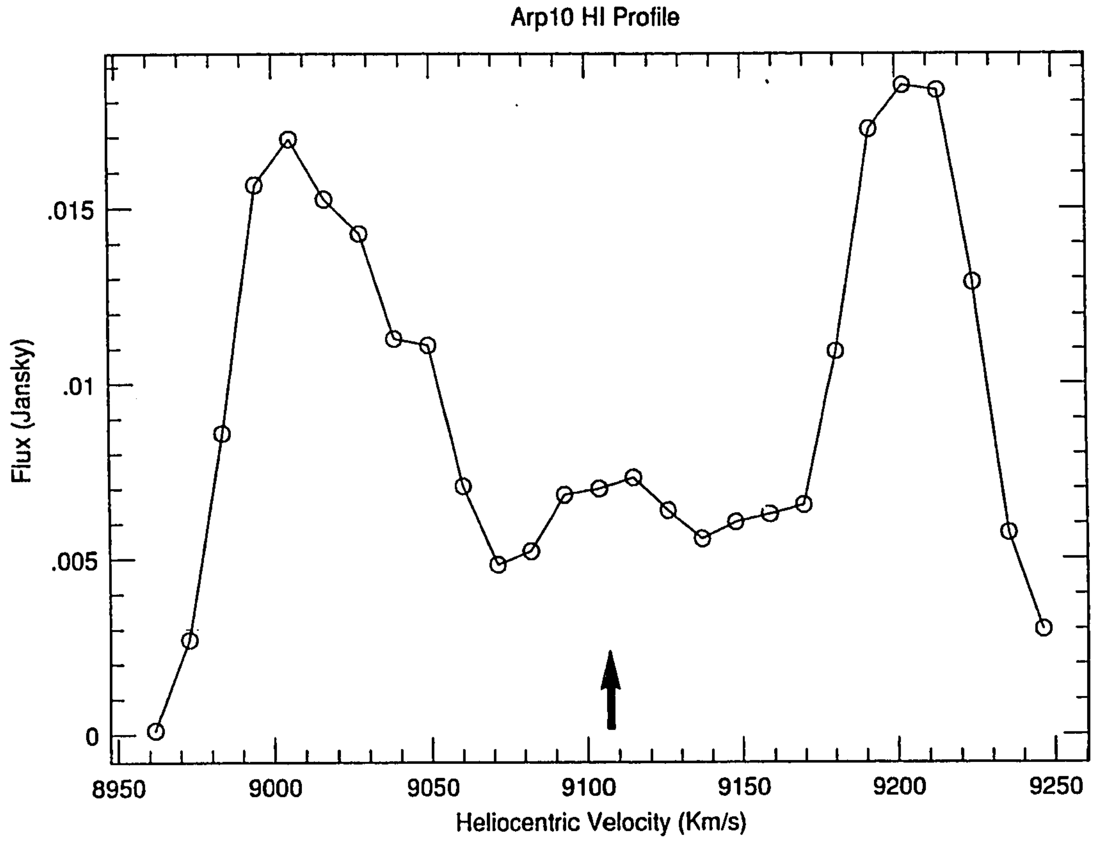

Figure 3.2: The global H I profile of Arp 10. The arrow indicates the systemic heliocentric velocity (9108 $\mathrm{km\,s^{-1}}$) of the galaxy derived from our observations.

where F_H is

$$F_H = 2.356 \times 10^5 \int S(V)dV = 6.48 \times 10^5 \ Jy\, km\, s^{-1} \tag{3.2}$$

and, D is the distance in Mpc, $S(V)$ is the flux density in Jy and V is the velocity in $\mathrm{km\,s^{-1}}$. The total H I mass of Arp 10 detected with the C-array is $M_H = 9.5\,10^9 M_\odot$

We present in Table 3.1 the derived H I properties of Arp 10. The heliocentric velocity of Arp 10, 9108 $\mathrm{km\,s^{-1}}$, is in close agreement with the value obtained by SA of 9093 $\mathrm{km\,s^{-1}}$.

The integrated H I distribution of Arp 10 is presented in Figure 3.3. We observe that the hydrogen emission is very extended and it is distributed over a roughly elliptically-shaped area (see Table 3.1). The H I dimensions are 2.7 times the diameter of the bright ring seen in the Arp (1966) Atlas (Ring 2 of CAM) and extends well outside the dimensions of the faint optical "ripples" seen in Figure 3.1. The H I emission exhibits strong peaks in two areas, one southeast and northwest of the nucleus. The northwestern peak seems to coincide with the part of Ring 2 which also displays strong Hα emission (CAM).

3.5 The Kinematics of Arp 10

We will show in this section that the kinematic behavior of the gas in Arp 10 is rather complex. We can begin to appreciate the complexity by inspection of the sequence of channel maps shown in Figure 3.4. Each map represents the H I surface density observed over a single channel of velocity width of 10.8 $\mathrm{km\,s^{-1}}$.

Unlike the channel maps presented for normal galaxies (see for example the

Table 3.1: Properties of Arp 10

$\alpha(1950)$	$2^{\mathrm{h}}15^{\mathrm{m}}48.9^{\mathrm{s}}$
$\delta(1950)$	$+5^{\circ}25'26.0''$
Distance	121 Mpc
Inner ring diameter	$5.6'' = 3.2$ kpc
Bright ring diameter	$43.0'' = 25.2$ kpc
Outer isophotes	$80'' = 46.9$ kpc
H I dimensions	$120'' \times 90'' = 70.4 \times 52.7$ kpc
V_{opt}	9160 ± 30 km s^{-1}
V_{HI}	9108 ± 10 km s^{-1}
$\Delta V_{1/2}$	249 ± 15km s^{-1}
$\Delta V_{1/5}$	272 ± 15km s^{-1}
F_H	6.48×10^5 Jy km s^{-1}
M_H	$9.5 \times 10^9\, M_\odot$
M_T[a] $= \frac{(\Delta V_{\frac{1}{2}})^2 R_{HI}}{G}$	$4.9\times 10^{11}\, M_\odot$
M_H/M_T	0.019

[a] M_T is an estimate of the the total dynamical mass of the galaxy.

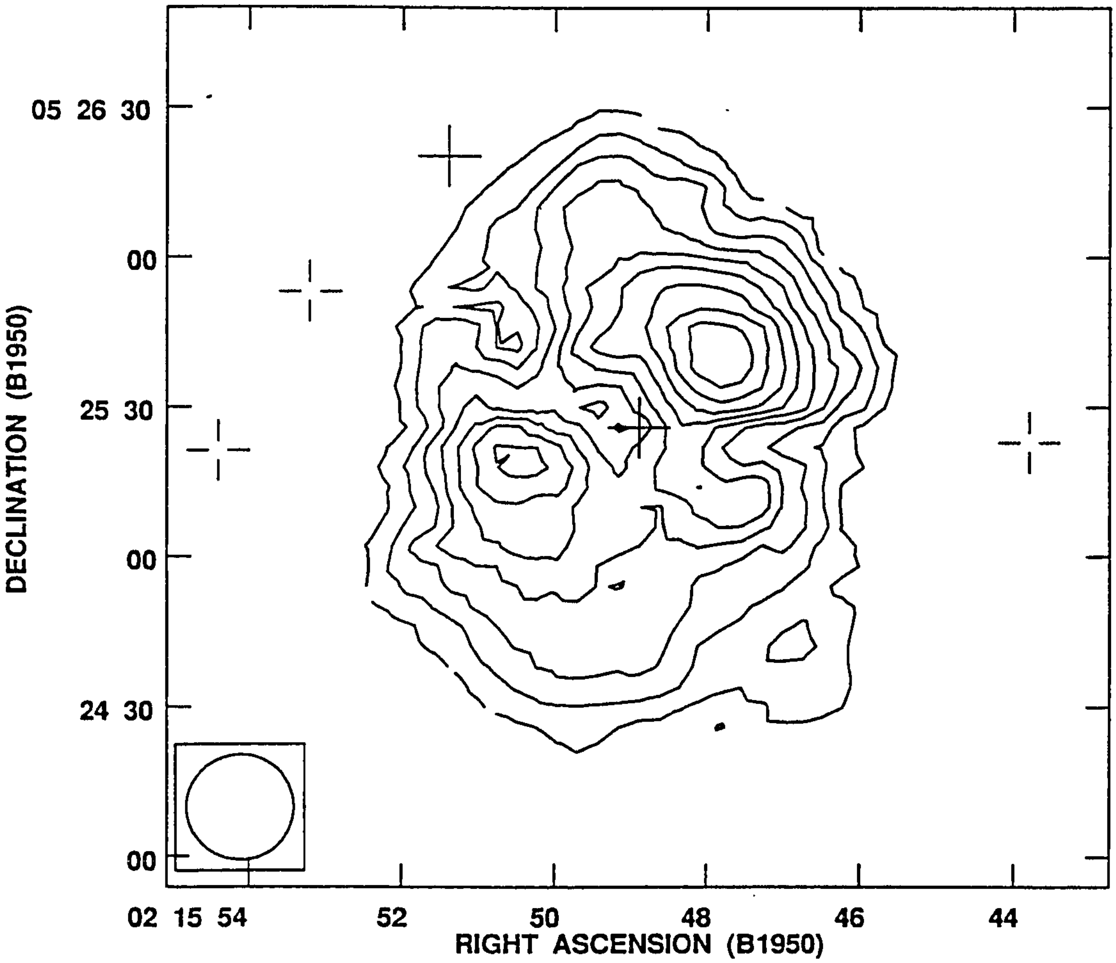

Figure 3.3: A contour map of integrated H I distribution. The contour increment is 37.22 Jy beam^{-1} m s^{-1} and the Level of the first contour is also 37.22 Jy beam^{-1} m s^{-1}. The three open crosses indicate the position of foreground stars and the two solid crosses mark the location of the background elliptical galaxy and the nucleus of Arp 10.

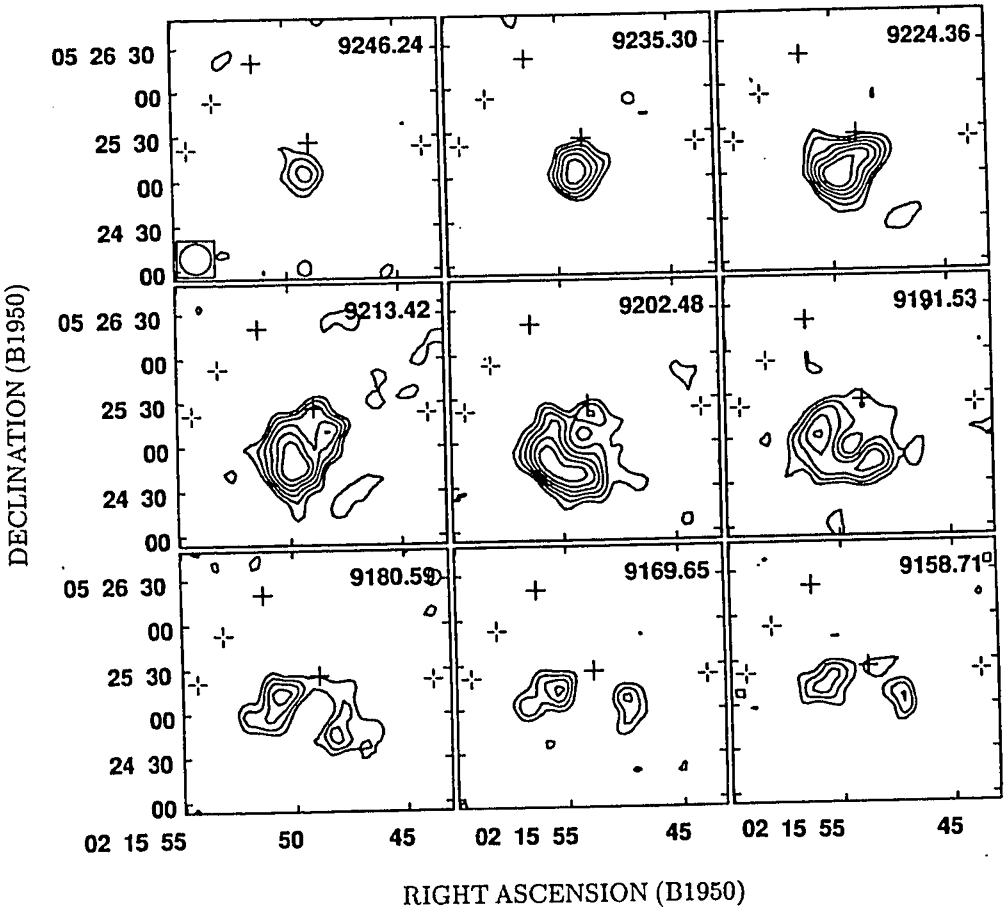

Figure 3.4: Contour plots of the 27 channel maps of Arp 10. The velocity of each channel is displayed in the upper right corner. The contour increment is 4.24×10^{-4} Jy beam^{-1} (one σ level) and the lowest contour displayed is at 3σ.

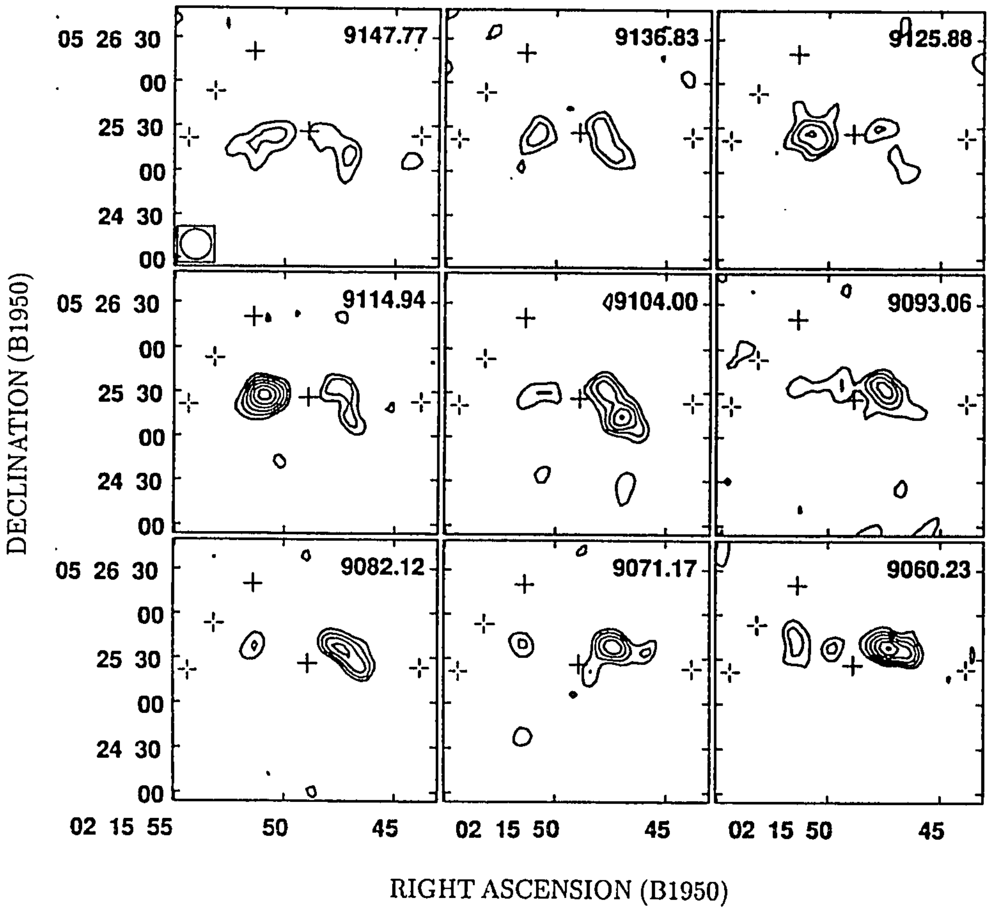

Figure 3.4 (Continued)

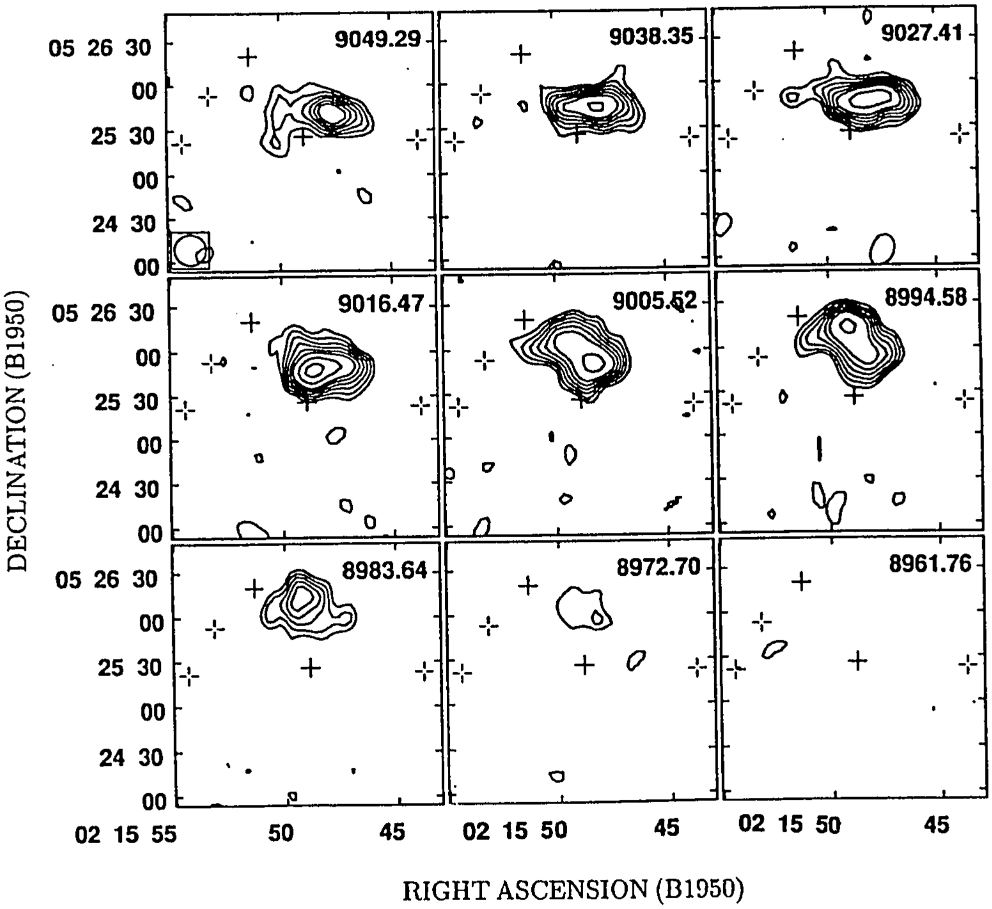

Figure 3.4 (Continued)

work of Wevers, 1984), the results in Figure 3.4 show a complex behavior indicating a disturbed or possibly warped system. We summarized the content of the channel maps in Figures 3.5a and b by splitting the emission features seen in the channel maps into two parts. Those which occur principally in the OUTER regions of the galaxy are shown in Figure 3.5a and those which are associated with the INNER disk and ring in Figure 3.5b. The dark lines indicate the approximate extent of the H I emission ridge-lines or centroids in each channel map superimposed on a deep B–band image of the galaxy (See Appleton and Marston 1995 for further details of the optical observations).

3.5.1 The Outer H I Structure

We will begin by discussing the outer H I structures in Figure 3.5a (Color Plate). An interesting aspect of the outer H I structures is the degree to which the H I structure fails to correlate with the faint optical "ripples" seen in the outer regions. The highest velocity emission, around 9350–9150 $\mathrm{km\,s^{-1}}$, develops into a major horseshoe-like loop [2] (seen especially at velocities around 9170–9192 $\mathrm{km\,s^{-1}}$). This H I structure feature extends much further south than any of the faint optical loops or filaments. As we proceed to lower velocities (9115–9000 $\mathrm{km\,s^{-1}}$) this outer structure breaks up into knots and arclets of emission to the west of Arp 10. The overall

---

[2] We note that the appearance of the horseshoe loop in the channel maps at these extreme velocities is a symptom of the apparently falling rotation curve of Arp 10 in its southern quadrant. In a simple disk with a falling rotation curve, features similar to horseshoe (but more closed at one end) would be expected. However, in this case, because of differences between the inner and outer disks, the horseshoe shape is much more open than would be normally expected giving it the appearance of a partial ring or loop.

Figure 3.5: The velocity structure of the outer (a) and inner (b) regions of Arp 10 superimposed on a deep B-band image. The dark lines indicate the approximate extent of the H I emission ridge-lines or centroids on each channel map.

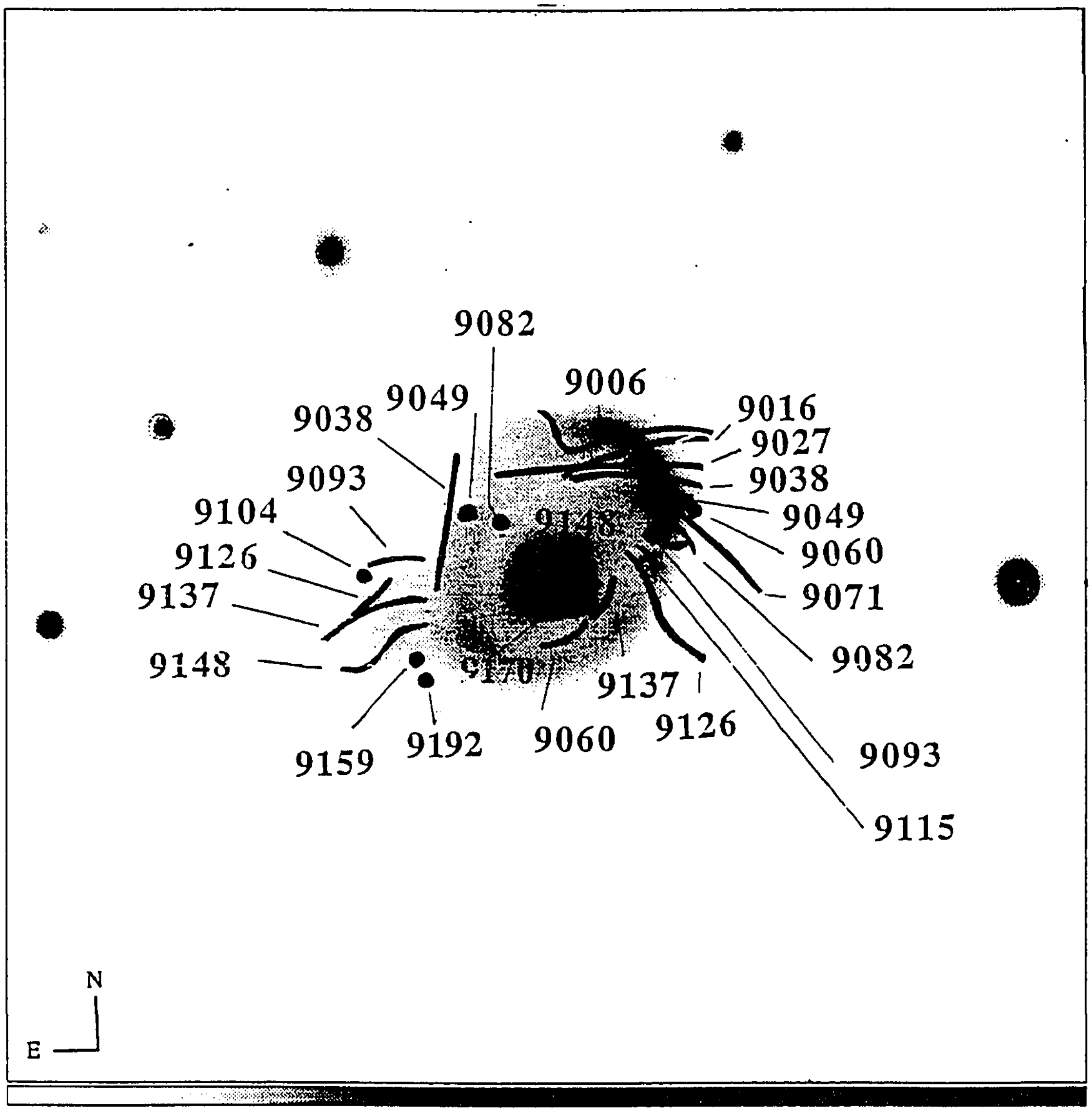

Figure 3.5 (Continued)

impression is that of an irregular outer H I disk which does not show any kinematic peculiarities which correlate strongly with wisps of faint optical emission.

There is considerably more coherence to the run of position with velocity on the eastern side of the galaxy were we see one of the few H I/optical correlations of the entire system. This occurs in the velocity range 9170 to 9016 km s^{-1}. In this interval the H I centroids at each velocity follow very closely the faint "arm-like" structure which protrudes from the southeastern end of the bright ring. The velocity gradient along this feature is quite constant (around 5.6 km s^{-1} kpc^{-1}) . As one proceeds to lower velocities, emission is seen over a considerable region around the northwestern end of the ring. The most striking aspect of the H I structure is seen at the lowest velocities when loop-like structures are again seen in the channel maps, almost mirroring the high velocity emission described earlier. These loops, seen at velocities of between 8995–8962 km s^{-1}, again have no direct optical counterparts. Unlike the high-velocity "horseshoe", these loops cannot be ascribed as an artifact of a falling rotation curve. One end of these kinematic loops connects to eastern end to the optical "arm" giving the appearance of a giant shell in the channel maps. Our main point here is to show that, although the outer H I disk of Arp 10 exhibits no obvious enhancements in H I surface density near optical features, there is evidence in the northern disk for correlations between kinematic features and the peculiar optical "arm". This is important because it suggests that at least some parts of the outer H I disk may be causally connected to the faint outer optical emission.

3.5.2 The Inner Regions of Arp 10 near the Bright Optical Ring

Are there better correlations between H I features and optical structures in the inner regions of Arp 10 ? In order to investigate this, we present in Figure 3.5b the inner H I ridge-lines and emission centroids superimposed on a grey-scale representation of the bright inner regions of the optical galaxy. Firstly, as was obvious from the integrated H I map presented earlier, there is strong H I associated with the northern bright region of the optical ring. H I emission can be traced from around 9006 $\mathrm{km\,s^{-1}}$ at the northwestern end of the ring around both sides of the ring to about 9071 $\mathrm{km\,s^{-1}}$ which follow approximately the optical ring. However, as we proceed to higher velocities, the spatial coincidence of the H I with the optical ring breaks down. The emission centroids along the western edge of the ring cross over the optical ring and are seen projected on the inside of the ring at velocities of 9170 $\mathrm{km\,s^{-1}}$. On the eastern side there is almost no correlation with ring position. In fact very little H I is seen distinctly associated with the southern end of the ring (this corresponds to a marked depression in the integrated H I map of Figure 3.3). The "arm-like" structure which was discussed above, is seen to develop to the east of the southern end of the ring but seems quite separate from the ring itself and shows no coherence with the ring. In one channel, an anomalous H I cloud is seen in the southwest quadrant of the ring at a velocity of 9060 $\mathrm{km\,s^{-1}}$.

Given the loopy and peculiar nature of the H I features traced in the channel maps, and the lack of obvious correlation between the H I and optical structures (except for the northern end of the bright ring and the eastern "arm"), it is perhaps surprising to find that the overall velocity field of the system looks, superficially, like a normal rotating disk. The mean velocity field of the H I emission is shown in

Figure 3.6. The overall impression is that of a single coherent rotating disk of H I with a kinematic major axis close to a PA of 0°. The northern end of kinematic major axis shows contours of increasing velocity with radius, symptomatic of a solid-body rotation curve, whereas the southern end of the galaxy shows a turn-over on the peak velocity and a slow decline thereafter with radius. A close inspection of Figure 3.6 will show that deviations from this simple picture are apparent at the approximate radius of the bright ring and in the outer regions of the disk, especially to the NE and the SW. The magnitude of the deviations are approximately 30–50 $\mathrm{km\,s^{-1}}$. It is clear from our earlier discussion of Figures 3.5a and 3.5b that the reason for the change in the isovelocity field at this radius is due to the shift in emphasis from the loopy outer structures, which have an approximate north-south kinematic axis, to an inner structure dominated by emission from the northern end of the ring and the inner stem of the eastern "arm". However, as Figures 3.5a,b show, the emission in both regions is far from normal for a simple rotating disk.

A velocity dispersion map of the H I was constructed but was not found to be helpful in the interpretation of the kinematics of Arp 10 and is not shown here. The map showed that the highest velocity dispersion in the H I was 76 $\mathrm{km\,s^{-1}}$ and it was located $5''$ north of the nucleus.

3.5.3 Attempts to fit a simple disk model

We devoted an extensive amount of effort in order try to explain the overall kinematics of the H I in terms of a) a simple rotating disk (with possible tilted rings), or b) a set of rotating and expanding rings of material, as might be expected from a collisional ring galaxy model (see Appleton and Struck-Marcell 1987 for example). In

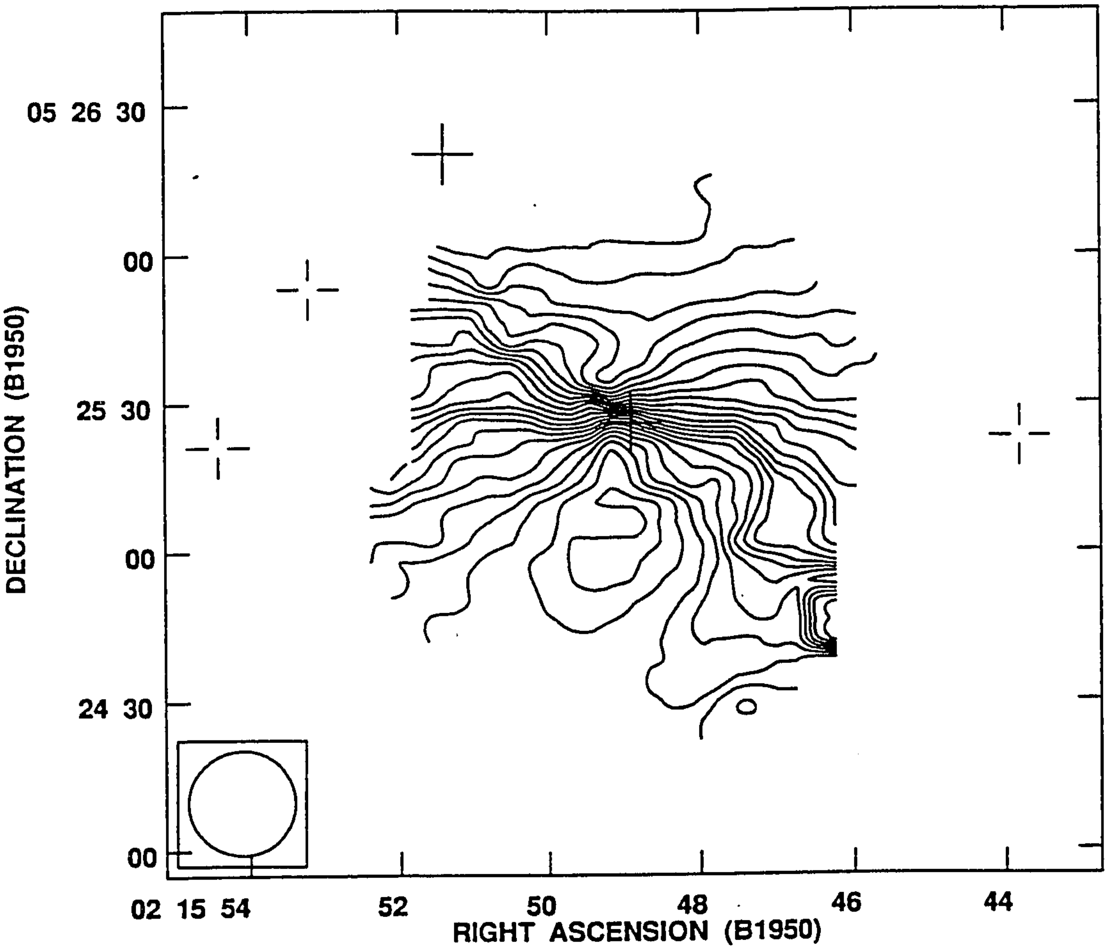

Figure 3.6: The mean velocity field of Arp 10. The isovelocity contours are at increment of 10 $\mathrm{km\,s^{-1}}$ starting at 9000 $\mathrm{km\,s^{-1}}$ at the north and reaching a peak value of 9220 $\mathrm{km\,s^{-1}}$ at the south. The three open crosses indicate the position of foreground stars and the two solid crosses mark the location of the background elliptical galaxy and the nucleus of Arp 10.

all cases these simple models failed to provide a good description of the H I kinematics. We outline below these unsuccessful attempts and argue that the failure to model the system is indicative of a disk which is extremely disturbed.

- Our first attempt was to fit a set of rotating tilted rings of increasing radius to the galaxy mean velocity field. Here we used the AIPS task GAL. The disturbed morphology of the northern region of the velocity field made it impossible to use a single model for the whole galaxy. Deviations of the order of 50 to 100 km s^{-1} were found if both the northern and southern ends of the galaxy were included. The fit was only moderately acceptable when we restricted the fitting to a wedge area between PA=140° and PA=200°. We note that the position angle for the kinematic axis in this case was found to be 175° which is significantly different from the major axis of the ring systems (130°). We conclude that a simple model is only a very rough approximation to the overall kinematics of the disk.

- The second attempt was to explore a model which assumes that at each radius the disk may be both rotating and radially expanding. Such a model has been successful in explaining the kinematics of the bright star forming ring in the Cartwheel ring galaxy (Fosbury and Hawarden 1977; Higdon 1993). Assuming reasonable values for the eccentricity and inclination of the rings we calculated the velocity v as a function of the deprojected azimuth ϕ, along a series of 14 elliptical rings of increasing radius. The position angle of the major axis of the rings was forced to be identical to the optical rings (i.e. PA=130°) Then, we performed a three parameter fit to each ring using the following function :

$$v = a_0 + a_1 sin(\phi + \phi_0) \tag{3.3}$$

where a_0, a_1 and ϕ_0 were the free parameters. A rotating and expanding ring would exhibit a simple sinusoidal shape, whose phase offset from the major axis is related to the amplitude of the expansion. The fits were generally poor, with calculated χ^2 per degree of freedom for each ring ranging from 0.39 to 0.53. We used a range of values for the eccentricity and the inclination of the rings, but no satisfactory fit was found. We concluded that velocity asymmetries of the order of 30–50 $\mathrm{km\,s^{-1}}$ were the primary cause of the failure of this approach.

The above results reinforce our belief that Arp 10 is a more complex collisional system that it was originally thought.

3.5.4 A Comparison between the Optical and H I Velocities

As discussed in Section 2 we obtained optical spectra along three slit positions with the KPNO 2.1m telescope. Two were through the center of the galaxy, along the major and minor axes of the rings, and a third was parallel to the minor axis but was offset to the extremely bright H II regions in the northwestern quadrant of the ring.

In Figures 3.7a and b, we show position-velocity diagrams through the center of the galaxy along both the major and minor axes of the rings (major axis assumed to be at PA=130°). The solid lines show the H I velocities (derived by taking slices through the H I velocity field at the appropriate positions of the optical slits) and the black dots show velocities measured in the H II regions using our KPNO spectra (derived from the Hα line). Within the errors of the optical observations (30 km s^{-1}), there is generally good correspondence between the optical and H I velocities for the major axis slice. There is a slight suggestion that the optical velocities are systematically higher by 50 km s^{-1} than those obtained in the H I. Our average optical velocity for the galaxy is 9160 km s^{-1} compared with the H I velocity of 9108 km s^{-1}. This velocity difference could be explained by a slight misalignment between the slit position and the nucleus during the optical observations, or alternatively could reflect a real difference between the velocity of the optical nucleus and the H I disk.

The asymmetry in the shape of the rotation curve is obvious. The northwestern disk shows a rising rotation curve, whereas the southeastern side of the galaxy flattens out at a radius of about 10 arcsecs. The position-velocity slice along the minor axis (Figure 3.7b) is peculiar in that large velocity gradients are observed (of order 150 km s^{-1} over an angular scale of $10''$). The optical velocities in the southwest quadrant of the galaxy seem to be higher than those found in the H I, even taking into account the systematic effect discussed above. Higher resolution spectra taken along different position angles in the system would be highly desirable to confirm these apparent differences.

3.6 The Search for a Nearby Companion to Arp 10

In our earlier purely optical study of the photometric properties of Arp 10 (CAM), we presented evidence of collisionally induced star formation in the galaxy. Based on the optical appearance of the bright regions of Arp 10 we had hypothesized that the dwarf elliptical galaxy located $60''$ northeast of the nucleus of Arp 10 was the "intruder" galaxy responsible for the formation of the ring structure by the process

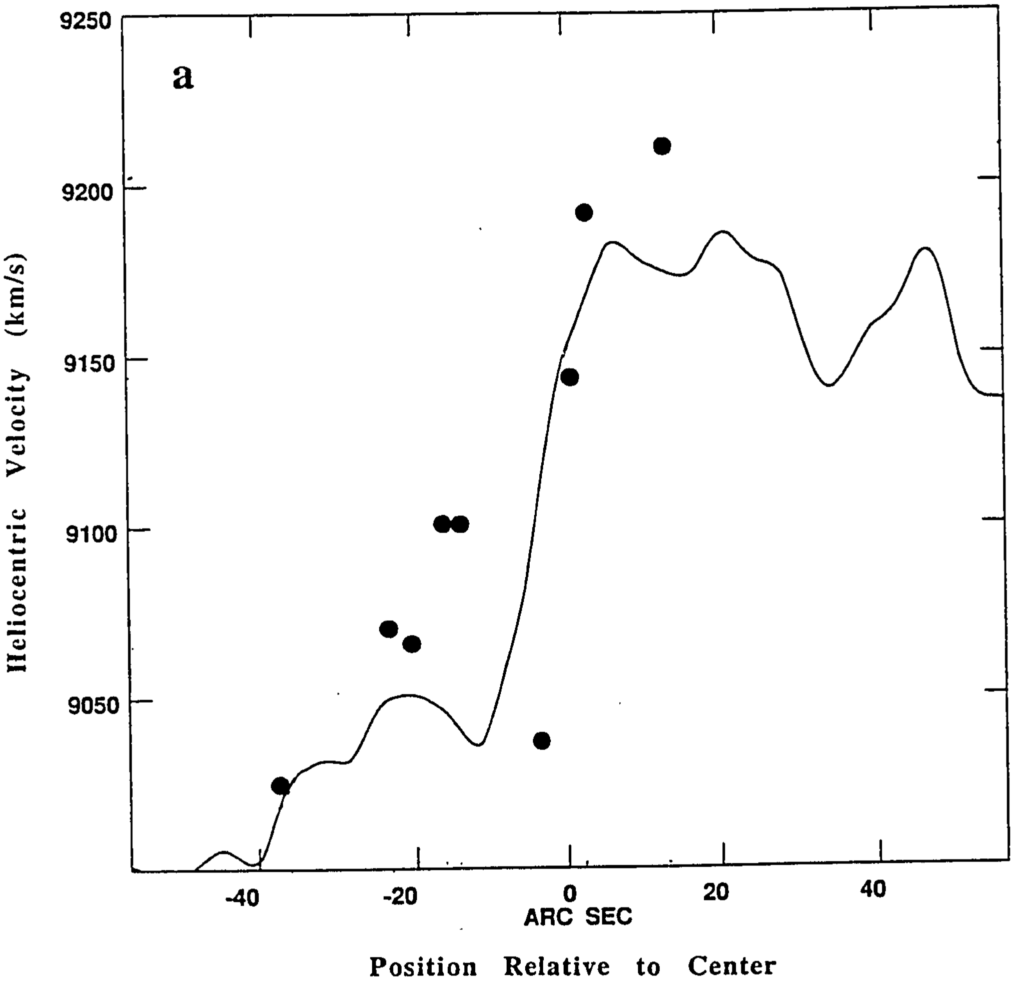

Figure 3.7: The position-velocity diagrams through the center of the galaxy along the major (a) and minor (b) axis. The solid lines show the H I velocities and the black dots show velocities measured in the H II regions using our KPNO spectra.

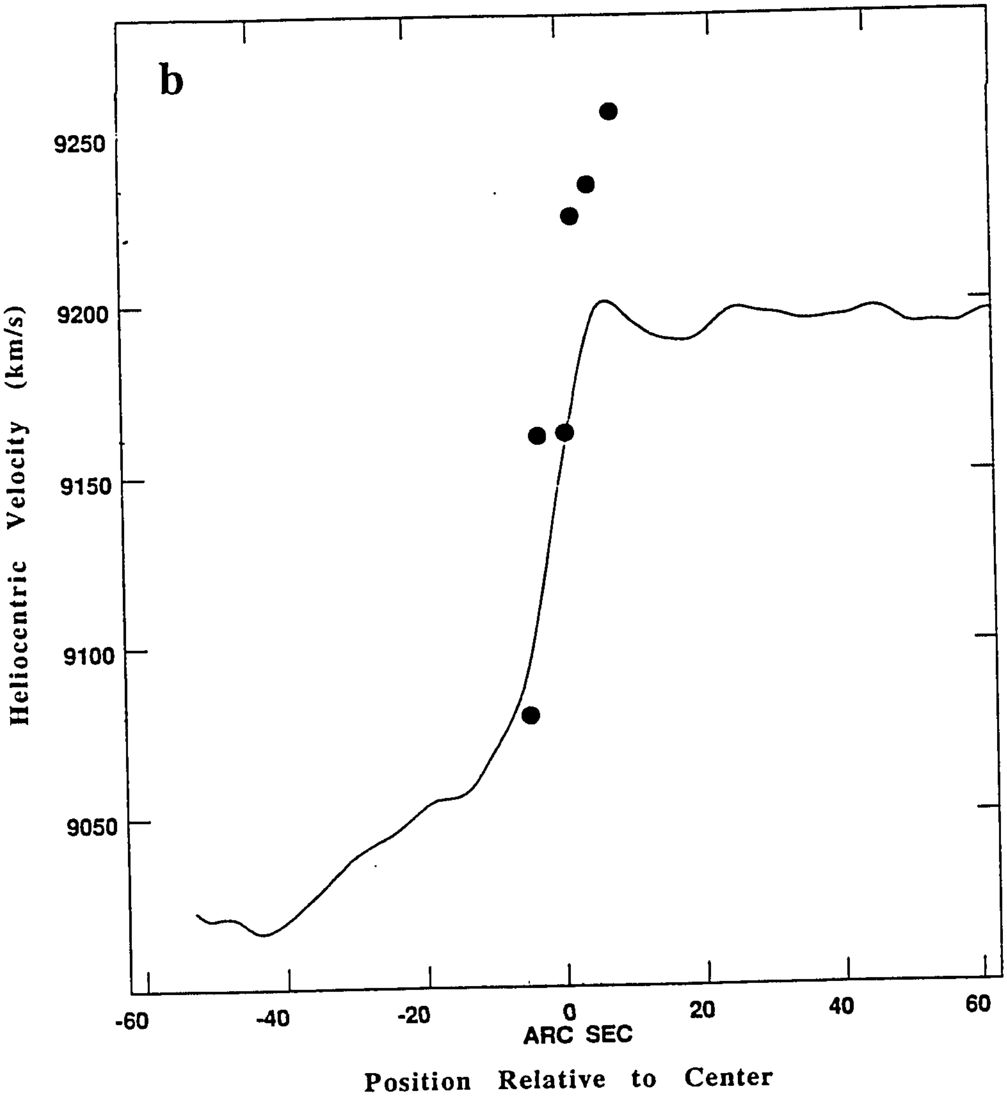

Figure 3.7 (Continued)

discovered by Lynds and Toomre (1976). However, optical longslit spectral observations of the elliptical galaxy presented here show that the elliptical is a background galaxy. As one can see in Figure 3.8, the spectrum of the elliptical galaxy clearly shows the Ca II H and K lines, and the G-band in absorption. The estimated velocity of the galaxy based on these lines is 26,680 km s^{-1} (z=0.089). This contrasts sharply with Arp 10 which has a redshift of z=0.03, indicating that the elliptical galaxy is not the companion to Arp 10. However, we will argue below that the presence of shells or "ripples" in the outer regions of the galaxy may be evidence for the disruption of a companion which may be in the process of merger.

3.7 Arp 10: Disk Formation or a Severely Disturbed Disk?

Arp 10 is not a normal galaxy. Optically, its appearance alone placed it in the peculiar galaxy catalogs of Arp (1966) and Vorontsov-Velyaminov (1977). If we consider the spatial distribution and kinematics of the H I alone, without regard to the optical image, we would conclude that Arp 10 consists of a large, quite disturbed, rotating gas disk. Because of our inability to fit a simple rotating disk model to the system and the fact that it appears, superficially at least, to have no nearby companion to stir the disk, it is natural to ask whether this could be an example of a primordial H I cloud which is just organizing itself into a disk system. This argument would appear to break down when the optical galaxy is considered. Broad-band photometry (Appleton and Marston 1995) of the galaxy show it to be one of the reddest ring systems in a sample of 12 such galaxies studied ($B-V$=0.8), suggesting a substantial old stellar population. The existence of a weak bar, star forming rings and shells in the outer parts of the galaxy suggest a collisional interpretation for the

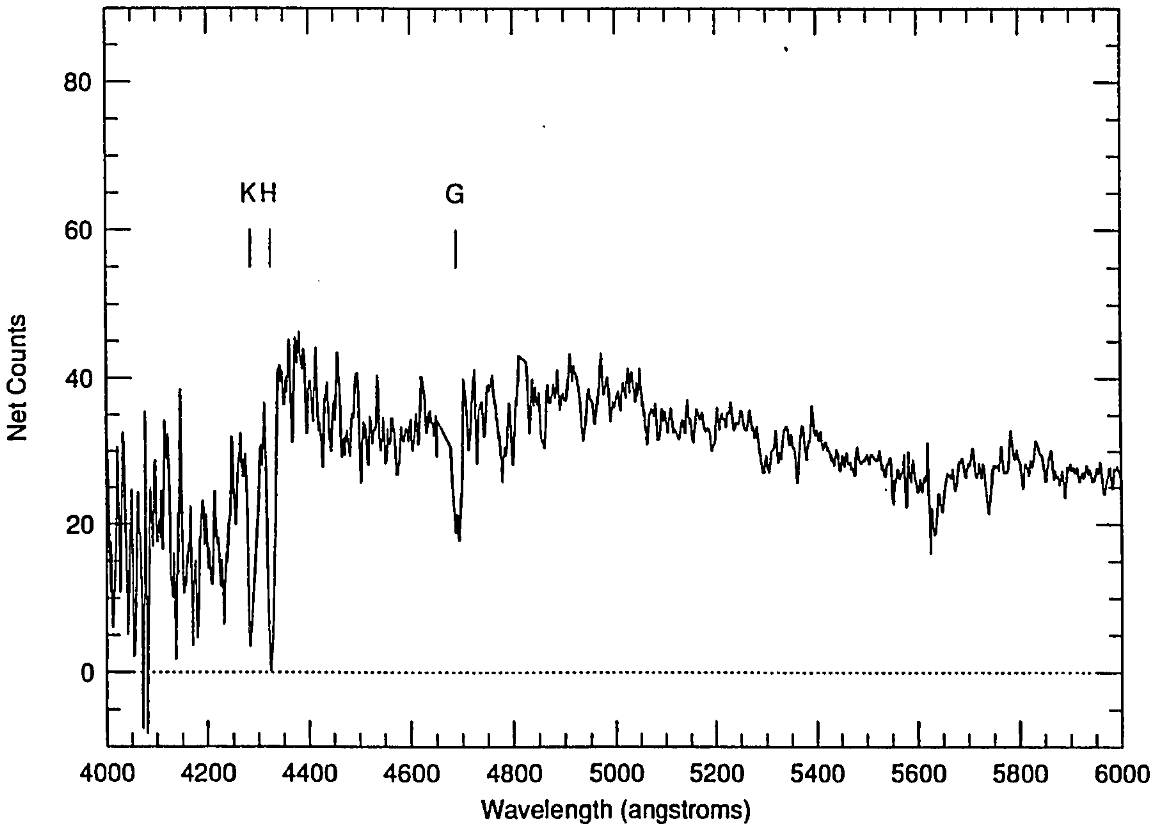

Figure 3.8: An integrated spectrum of the "companion". We mark the position of Ca II H and K lines, and the G–band.

disturbed H I kinematics. We will therefore not consider the primordial hypothesis further.

The discovery of faint loops and ripples in the outer optical isophotes suggests that the system may have much in common with the "ripples around disk" systems of SS88. These authors discovered that, like the shells around elliptical galaxies (Malin and Carter 1980), early-type disk galaxies can also be surrounded by shells or ripples of faint optical emission. Schweizer and Seitzer argued convincingly that the ripples were external in origin and probably were the result of debris from a major accretion event onto a disk from a nearby companion. The implication from their work is that significant mass transfer or even mergers involving a low-mass companion may not always lead to the complete disruption of the larger disk system. As we discussed in Section 4, Arp 10 also has a loopy outer H I distribution. Recent work by Schiminovich et al. (1994,1995) has shown that weakly correlated H I/optical structures have been seen in shell elliptical galaxies.

We believe that the evidence is strongly in favor of Arp 10 being primarily a disk system which is in a non-equilibrium state. The existence of relatively large non-circular motions in the H I disk, combined with the very unusual distribution of the H I loops and filaments and their mismatch with the equally anomalous optical "ripples" is clear evidence for a disturbed system. **The overall kinematics of the large H I disk suggests a system in which rotation dominates over radial motions, but only just.** Various parts of the galaxy are experiencing quite large non-circular motions of the order of 30 to 50 $\mathrm{km\,s^{-1}}$ (approximately 25–30% of the rotational velocities). The discovery by CAM of three successively nested rings or ring-arcs of star formation in Arp 10 was interpreted by them as evidence for a central perturbation of the potential via the ring galaxy mechanism (e.g. Lynds and Toomre 1976). Although the H I velocity field does not support such a simple picture, the existence of the rings is consistent with a disk system in which the gravitational potential is time varying. Such transients might be introduced by an ongoing accretion/merger of a disk system with a lower-mass (say 1/3 mass) companion in which the disk has been disturbed but not quite disrupted (as suggested for other ripple galaxies by Schweizer and Seitzer 1988).

The most likely explanation for Arp 10 is that of a disk system which has been strongly disturbed by a recent large accretion event which has created the ripple-like structures in the outer optical galaxy. Since no large companion is known associated with Arp 10, we suggest that the companion has been almost completely disrupted by the accretion/merger. In the SS88 "ripple galaxies", mass transfer rather than two-body merging is believed to be the dominant mechanism for setting up the ripples. On the other hand, it can only be a matter of time before the companion is so strongly disrupted that its identity is lost. In their sample of ripple galaxies, SS88 show numerous examples of companionless ripples. We suggest that Arp 10 will soon become such a case.

Our earlier optical observations (Figure 1 of CAM) showed that there is a bright extra-nuclear knot between the first and second star forming rings in Arp 10, which we suggested might be in some way related to the nature of the rings. In Figure 3.9 we show a J–band image of Arp 10 which clearly shows the knot which may be slightly extended in the direction of the nucleus of Arp 10. No obvious H I component was found associated with the knot (except perhaps the peculiar velocity component at 9060 $\mathrm{km\,s^{-1}}$ mentioned in Section 4.2) and our optical spectra did not sample the region. Hence, the velocity of the knot is unknown. However, we consider it possible that the knot is a remnant nucleus of a second galaxy which has been disrupted by the collision/merger with the more massive "target". If the collision was close to head-on (in order to set up the rings seen in the inner regions of Arp 10) and the collision was slow, the disruption and merger of the nucleus would be quite rapid (perhaps of the order of two crossing times, or approximately a few × 10^8 years). The nucleus would fall quickly into the center by the mechanism of tidal friction (Binney and Tremaine 1987) leaving the ripples behind as evidence of a disruptive collision. The fact that the ripples are somewhat asymmetric (the optical ripples are seen mainly in the south) might suggest that only one or two passages of the infalling galaxy have occurred since the initial collision. This would be consistent with the perturbations to the H I velocity field which would be expected to be damped quite quickly as a result of dissipation in the disk.

It is interesting that Arp 10 exhibits both star forming rings similar to those seen in collisional ring galaxies, and faint outer ripples like those seen in the accretion-dominated merger systems. Our observations suggest that when the accreting galaxy is massive enough it can not only produce ripple-like debris, but also drive waves through the disk of the target galaxy. As such, Arp 10 seems to represent an interesting transition case between accretion-driven shell and centrally perturbed disk systems. Very little modeling of this sort of merger has yet been performed. Taniguchi and Noguchi (1991) showed that a collision between two galaxies in which one travels through the center, but co-planar to the disk target disk, can produce shell-like structure and rings not too dissimilar from the structure of Arp 10 (They called these galaxies "Wing" galaxies because of the shape of the debris of the galaxy that was

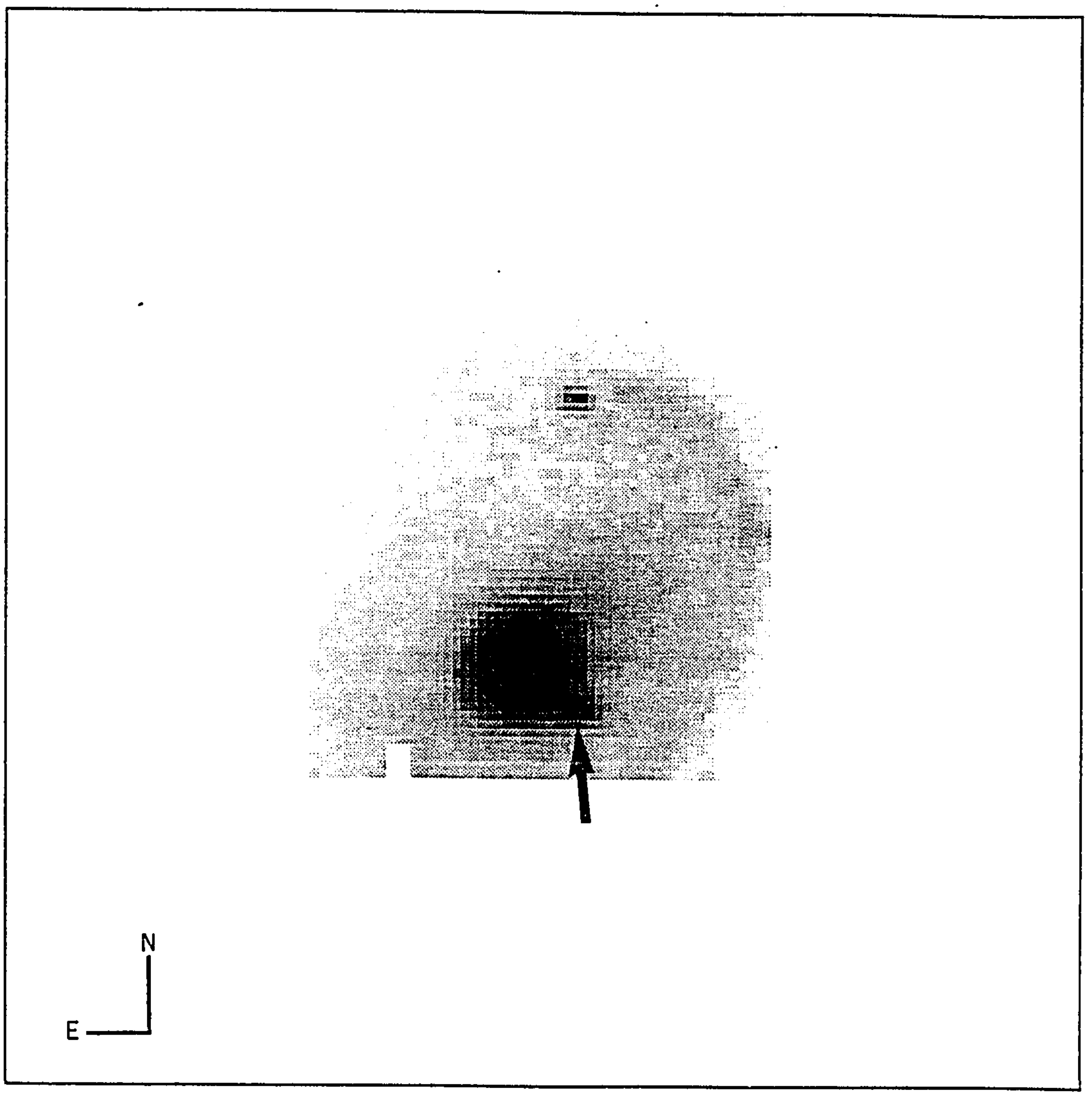

Figure 3.9: A J–band (1.25 μm) near-IR image of the central regions of Arp 10. The arrow indicates the extra-nuclear knot which we suspect is the remnant nucleus of a merging second galaxy (Data from 2.1m IRIM photovoltaic array from unpublished work of P. N. Appleton and A. P. Marston).

disrupted in the collision). Although Arp 10 is not well represented by this model, the observations do remind us of the huge parameter space that remains unexplored by numerical modeling, especially those involving the disruption of lower-mass galaxies. The observations also underline the importance of obtaining 21cm H I observations, which in this case, led to a different explanation for the origin of the rings from those based on optical observations alone.

Finally, it is worth returning to the horseshoe like structures seen in the H I channel maps of Figure 3.4 at the most extreme velocities seen in Arp 10. As we discussed in Section 4, these structures are associated with the outer H I disk only. They are not, at present, distinctly separate structures from the rest of the H I disk of Arp 10, but are identifiable only as loops in the velocity-position phase-space of the channel maps. However, it is interesting to note that if the entire **inner** H I disk of Arp 10 was removed (perhaps as a result of the ultimate collapse of the gas towards the center of the system due to cloud–cloud collisions), these loops would then become isolated from the rest of the system. It is perhaps significant that isolated "horseshoe-like" H I emission features, similar to those found in Arp 10, are seen in the outer parts of NGC 2865 and Centaurus A — both shell elliptical systems (Schiminovich et al. 1994, 1995). These structures may therefore be remnants of huge neutral hydrogen disks which preceded the shell-making collisions. If this is true, then those H I loops may contain important information about the progenitors of shell and ripple galaxies[3].

---

[3] We note that if the central regions of a "normal" H I disk were to be removed, the remaining outer filaments of H I would not have the same interesting "horseshoe" character of those found in Arp 10.

3.8 Conclusions

Our optical and H I study of the peculiar galaxy Arp 10 has led to the following conclusions:

- The optical imaging shows evidence for faint filaments and loops suggesting of a merging system similar to the "ripple" galaxies discovered by SS88.
- Optical spectra of the nearby elliptical galaxy, originally suspected of being the colliding companion show it to be a background galaxy.
- The H I emission from Arp 10 shows a disk which extends to 2.7 × the radius of the bright ring. The H I extends outside of the faintest optical features seen in deep CCD images. The most notable feature of the H I emission is that it seems to be composed of two different, but related structures. In the outer regions, the H I "disk" has no clear optical counterpart. Its kinematics suggests distinctly different motions than those found in the inner disk, although the entire H I disk seems to suggest a single coherent structure.
- The inner H I disk shows some correspondence with the optical ring. At least 50% of the ring shows regular rotation, half of the H I ring is either missing or has been severely warped away from the optical ring.
- A simple kinematic model of a rotating disk fails to reproduce the observed velocity field.
- Deviations of the order of 30–50 km s^{-1} (25–30% of the observed velocity field) are found which suggest that the disk is out of equilibrium. Attempts to fit the

velocity field with a set of nested rotating and expanding elliptical rings also failed to reproduce the observations.

- The picture most consistent with the observations is that Arp 10 is a disk system which has been strongly disturbed by a recent large accretion of a gas poor galaxy. Such a scenario would explain both the disturbed velocity field of the H I disk and the faint optical "ripples" seen at the outer parts of the system. A possible remnant nucleus of the accreted galaxy is seen near the center of the system.
- The observations of the disturbed, but not completely disrupted H I disk underlines the robustness of large disks to disruption by massive accretion events. Arp 10's H I disk extends out further than the optical ripples and yet has been able to maintain a moderate degree of overall coherence from its outer loopy regions to the inner disk. The galaxy represents an interesting class of merging system which lies intermediate between the classical ring galaxies and the classical shell or ripple systems.
- We note that if the inner part of the H I disk was removed from Arp 10, the properties of the outer loops seen in H I channel maps would strongly resemble features seen in H I maps of shell elliptical systems (Schiminovich et al. 1994, 1995). This suggests that some shell-elliptical systems may still contain the remnants of large H I disks similar to the one discussed here. The strong dissipation of angular momentum in the inner disk during a shell-making collision may have caused the gas in the inner regions to fall towards the center, leaving only the outer disk to orbit the remnant. If this is plausible, then Arp 10 is an

interesting laboratory for studying the early stages of this transient process.

It would be desirable to obtain high resolution spectroscopy of the possible second nucleus of Arp 10 in order to determine its radial velocity relative to the disk. We note that high resolution VLA observations of the radio continuum emission in Arp 10 have recently been made (Ghigo and Appleton, in preparation) and these contribute further to our understanding of this fascinating galaxy.

3.9 Acknowledgments

We thank C. Struck and R.J. Lavery (Iowa State University), K. Taylor and D. Malin (AAO) for stimulating discussion. The authors enjoyed interesting discussions with J. van Gorkom and D. Schiminovich (Columbia University) in connection with the similarities between Arp 10 and a number of published and unpublished observations of shell elliptical galaxies. We are grateful to E. Brinks (NRAO, Socorro) for useful suggestions during the VLA data reduction process and T. Marston (Drake University) for assistance during the acquisition of the optical spectra. We also thank an anonymous referee for helpful comments about the manuscript. This work is funded under NSF grant AST-9319596.

3.10 References

Appleton, P. N. & Marston T. 1995, ApJ, (preprint)

Appleton, P. N. & Struck-Marcell, C. 1987, ApJ, 312, 566

Appleton, P. N. & Struck-Marcell, C. 1995, Fundamentals in Cosmic Physics, (In Press)

Arp, H. C. 1966, Atlas of Peculiar Galaxies (Pasadena: California Institute of Technology)

Binney, J. & Tremaine, S. 1987, "Galactic Dynamics." (Princeton: Princeton University Press)

Bosma, A. 1981, AJ, 86, 1791

Charmandaris, V., Appleton , P. N. & Marston T. 1993, ApJ, 414, 154 (CAM)

Dupraz, C. & Combes, F. 1986, A&A, 166, 53

Fosbury, R. A. E. & Hawarden, T. G. 1977, MNRAS, 178, 473

Hernquist, L. & Quinn, P. 1987, ApJ, 312, 1

Higdon, J. L. 1993, Ph.D. Thesis, University of Texas at Austin

Hogbom, J.A. 1974, A&A, 15, 417

Lynds, R. & Toomre, A. 1976, ApJ, 209, 382

Malin, D.F. & Carter, D. 1980, *Nature*, 285, 643

Quinn, P. 1984, ApJ, 279, 596

Sulentic, J. W., & Arp, H. 1983, AJ, 88, 489 (SA)

Schweizer, F. & Seitzer, P. 1988, ApJ, 328, 88 (SS88)

Schiminovich, D., van Gorkom, J., van der Hulst, J. M. & Kasow, S. 1994, ApJ, 432, L101

Schiminovich, D., van Gorkom, J., van der Hulst, J. M. & Malin, D. F. 1995, ApJ, 444, L77

Taniguchi, Y. & Noguchi, M. 1991, AJ, 101, 1601.

Wevers, B.M.H.R. 1984, Ph.D. Thesis, University of Groningen

Winrich, C. & Appleton, P. N. 1995 (preprint)

Vorontsov-Velyaminov, B. A. 1977, Atlas of Interacting Galaxies, A&AS, 28, 1

CHAPTER 4.

OBSERVATIONS OF THE HEAD-ON COLLISION BETWEEN TWO GAS-RICH GALAXIES: THE NEUTRAL HYDROGEN DEBRIS FROM THE "EMPTY" RING GALAXY VII ZW 466

A paper submitted to The Astrophysical Journal

Philip N. Appleton and Vassilis Charmandaris

4.1 Abstract

We present VLA H I spectra of the ring galaxy VII Zw 466. VII Zw 466 is an example of a classical collisional ring galaxy with a single well defined star forming ring. Our observations reveal the kinematics of the neutral hydrogen disk of the ring. The northeast side of the ring is severely disturbed showing evidence of the tidal interaction. The H I distribution is highly asymmetric with fingers of H I gas extending to the east in the general direction of the two major companions. The H I gas corresponding to the optical ring exhibits the typical profile of a rotating-expanding ring. A formal three parameter fit to the data indicates that the expansion velocity of the ring is 32 $\mathrm{km\,s^{-1}}$. We also detect a hydrogen plume from the southern companion pointing towards the ring galaxy. This leads us to believe that this companion may be the one directly responsible for the formation of the ring galaxy. Finally, we

detect H I emission from two previously unknown dwarf galaxies located northeast and southeast of VII Zw 466 respectively. This brings the total number of members of the VII Zw 466 group to five. Using the projected mass method, the upper limit of the dynamical mass of the group was estimated to be $M_O = 3.5 \times 10^{12}$ $M_\odot$, which implies that the mass to light ratio of the group is $(M/L)_{group} \approx 70$.

4.2 Introduction

The idea that galaxies might be transformed as a result of interactions, collisions and mergers was presented by Toomre and Toomre (1972) to explain the diversity of forms seen in many of the images of peculiar galaxies (Arp 1966, Vorontsov-Velyaminov 1979). Observations since that time have further strengthened the view that interactions may play a crucial role in galaxy evolution. In particular, as Toomre has suggested, they may be responsible for the formation of elliptical galaxies through major mergers and collisions. Mergers arise naturally out of most hierarchical models of the growth of structure in the Universe. Observations of rich clusters of galaxies, typically an elliptical rich environment, at redshift of between 0.3 and 0.6 seem to show an increased fraction of blue galaxies, with a significant fraction undergoing an interaction (Butcher & Oemler 1984; Lavery & Henry 1988; Dressler *et al.* 1994). For those blue galaxies which are interacting, there is increasing evidence from HST observations that many have shell-like or ring-like morphologies (Lavery *et al.* 1995; Oemler 1995). Although these may not all be collisional systems, it is interesting to study low-redshift galaxies which show similar morphologies and ask whether these are simply analogs of processes occuring at higher redshift. In this category we would include the shell ellipticals (Malin & Carter 1980), the galaxies with ripples (Schweizer

& Seitzer 1988) and the collisional ring galaxies (Lynds &Toomre 1976; see Appleton & Struck-Marcell 1995 for review). Understanding the formation and evolution of collisionally induced rings and shells at low redshift may help us to disentangle the collisional from non-collisional mechanisms which may be responsible for rings and shell morphologies at higher redshift.

Understanding the details of a collision between two gas-rich disk systems of unequal mass ratio is probably one of the most challenging problems in numerical modeling today (Barnes & Hernquist 1992, Struck 1995). The treatment of shocks in the disks of two inter-penetrating galaxies is quite difficult to simulate and very few examples exist in the literature. Struck (1995) has recently attempted to model both the hot and cold gaseous component during a head-on collision to produce the Cartwheel galaxy and many complicated physical processes are at work during and shortly after the penetration of the "target" galaxy by the "intruder". It is therefore of considerable interest to map the cool and hot components of the gas in a real collision and make comparisons with models. This paper is an attempt to map the distribution and kinematics of the H I (cool) component of gas shortly after a collision between two gas rich galaxies. The H I splatter left behind is a testimony of the rapidity of which the cool gas has reformed after a head-on collision. We will leave it to future X-ray astronomers to map the distribution of the hot gas component in this system.

In this paper we describe the mapping of the neutral hydrogen emission from a classical ring galaxy called VII Zw 466. The galaxy was discussed very early on in the debate about the origin of these peculiar rings (Theys & Spiegel 1976; Lynds & Toomre 1976). An early photometric study of VII Zw 466 was made by Thompson

& Theys (1978) in which the colors and knots within the ring were discussed. This galaxy has also been the subject of a recent optical and infrared study (Marston & Appleton 1995; Appleton & Marston 1995) and strong radial color gradients were found within the ring. The color gradients are consistent with the idea proposed for the Cartwheel ring galaxy (Marcum, Appleton & Higdon 1993; Higdon 1994) that the reddening from the outer ring inwards is due to the effects of stellar evolution in the wake of the expanding ring. In such a scenario, much of the light from ring galaxies has been formed in stars which have been born recently in the ring wave and as such, these galaxies represent "young" galaxies. Some of these large blue ring galaxies may therefore be low redshift analogs of the galaxies seen at higher redshifts.

Throughout this paper, we will adopt a Hubble constant of 80 $\mathrm{km\,s^{-1}}$ $\mathrm{Mpc^{-1}}$. We have determined the heliocentric optical velocity of the galaxy to be 14,465 $\mathrm{km\,s^{-1}}$ and therefore assume a distance to the VII Zw 466 group of 180 Mpc.

4.3 Observations

The observations were made on December 3 1994, using all 27 telescopes in the C configuration of the VLA[1] . The correlator was set in a two IF mode (AC BC) with on-line hanning smoothing and 32 channels per IF. For each IF we used a bandwidth of 3.125 MHz. This provided a frequency separation of 97.6 kHz per channel, which corresponds to 22.66 $\mathrm{km\,s^{-1}}$ in the rest-frame of the galaxy using the optical definition of redshift. To achieve a wider velocity coverage, IF1 was centered at 14,131 $\mathrm{km\,s^{-1}}$ and IF2 at 14,538 $\mathrm{km\,s^{-1}}$. As a result, the velocity coverage of

---

[1] The Very Large Array is operated by Associated Universities Inc. under cooperative agreement with the National Science Foundation.

our observations was 974 $\mathrm{km\,s^{-1}}$. A total of 4 hours 47 min was spent on source. Flux and phase calibration was performed using the sources 3C286 and 01311+678 (B1950) respectively.

These data were first amplitude and phase calibrated and bad data due to interference were flagged and ignored by the AIPS software. An image cube was created from the UV data by giving more weight to those baselines which sampled the UV plane more frequently (so-called natural weighting). This provided a synthesized beam with a FWHM of $23.3'' \times 21.9''$ for IF1 and $21.6'' \times 19.3''$ for IF2.

The subtraction of the continuum emission in each line map was performed using a standard interpolation procedure based on four continuum maps free from H I at each end of the band. The resulting rms noise per channel was 0.27 $\mathrm{mJy\,beam^{-1}}$.

The highest dynamic range in any channel map was 5:1 (at v=14,402.8 km/s) with a peak flux of 1.35 mJy/beam. Even in this bright channel, no sidelobes were detectable and, therefore, we did not find it necessary to use the CLEAN procedure (Hogbom 1974) in our data.

In order to determine the total H I distribution we used the following technique. Initially, we smoothed all channel maps to a resolution $44.0'' \times 44.0''$, twice that of the synthesized beam. New maps were formed comparing, pixel for pixel, the original full resolution maps to the smoothed ones. The pixel values of original maps were copied to the new ones only if the signal-to-noise ratio of the smoothed map at that point exceeded 2. The total H I surface density map was produced by adding the new maps all together. The same technique was used to create the first and second moment maps of the distribution. Using this procedure we effectively give more weight to points associated with low surface brightness emission.

Optical observations of a 16x16 arcmin field were obtained during photometric conditions on April 2 1995, with the Fick Observatory 0.6 m CCD system (Appleton, Kawaler & Eitter 1993). A 500 sec exposure using an R–band filter was taken. Calibration of the photometry was performed using data taken from the star G10 50 (Landolt 1992).

4.4 The VII Zw 466 Group and its H I Distribution

In Figure 4.1 we show the VII Zw 466 group and its environment from a wide field image obtained with the 0.6m E.W. Fick telescope and CCD system (described in Appleton, Kawaler & Eitter 1993). In addition to the ring, there are two nearby companions labeled G1 and G2 as well as a background galaxy B1 (Appleton & Marston 1995). Galaxy B1 (first noted as background by R. Lynds; see Theys & Spiegel 1976) has a velocity of $V_{\odot}$ = 25,042 $\mathrm{km\,s^{-1}}$, determined from our own unpublished optical spectra. Also marked in Figure 4.1 are two new dwarf galaxies, G3 and G4, discovered during the H I mapping of the group, presented in this paper.

In Figure 4.2 we show the integrated neutral hydrogen emission from the VII Zw 466 field superimposed on a B-band image of the group (from Appleton and Marston 1995). The emission from the ring galaxy is highly disturbed. The brightest emission comes from the northern quadrant of the ring and sweeps around in a clockwise direction along the western quadrant of the ring. A filament of H I extends to the south-east pointing to a region between G1 and G2. In addition, there is a marked depression in the H I emission from the south-eastern quadrant of the ring. It is in this quadrant that the optical emission in the ring is rather faint.

H I emission is also detected from the edge-on companion G2. The H I has a

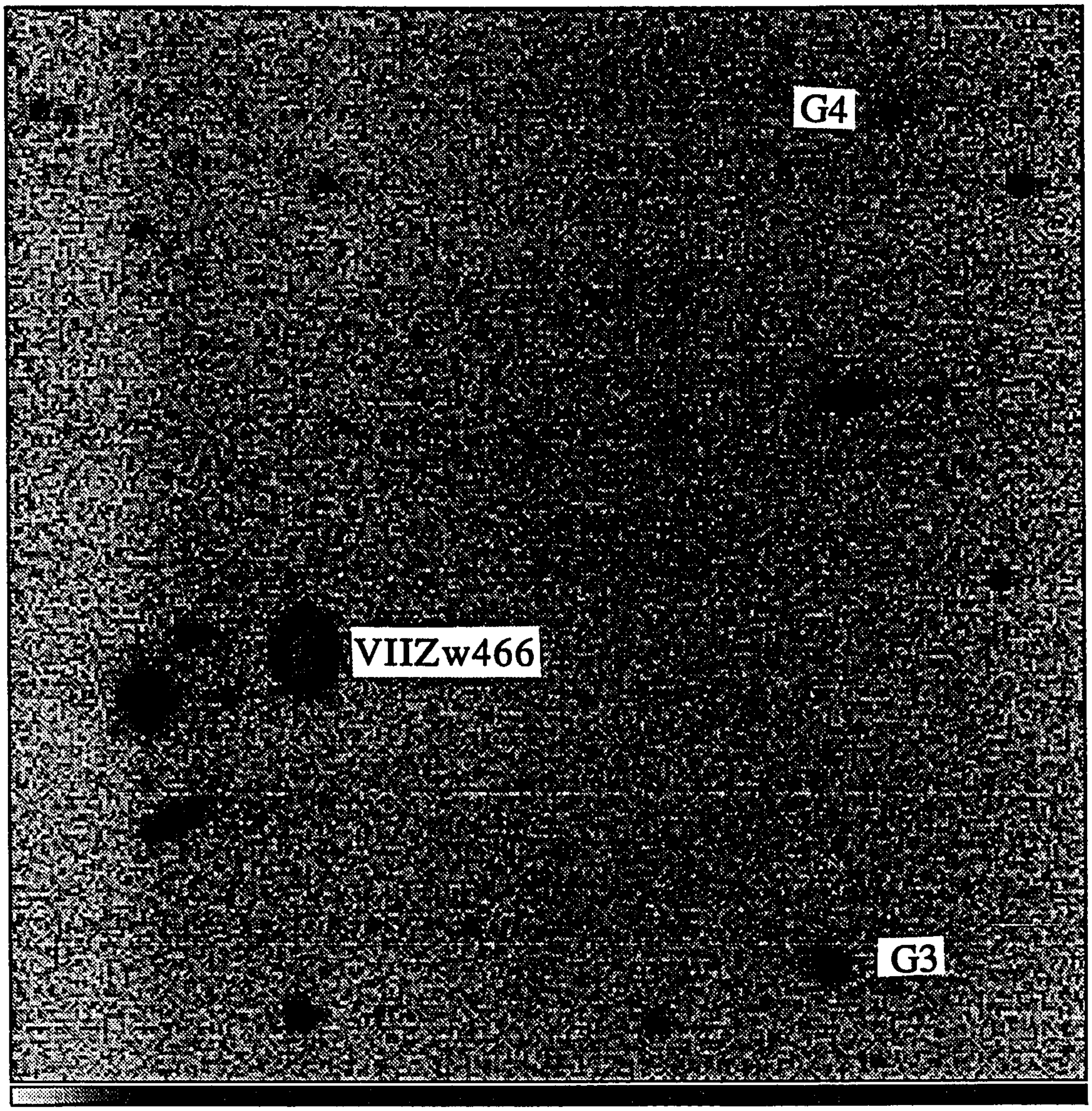

Figure 4.1: Grey-scale image of VII Zw 466 through a V–band filter taken at Fick Observatory. The positions of the two dwarfs are marked as G3 and G4.

large peak centered on the south-eastern end of the major axis with fainter emission extending along the major axis. A very faint filament extends from G2 back towards the ring.

No emission down to a level of 0.68 mJy beam^{-1} (2.5σ) was detected from the peculiar elliptical galaxy G1. If we adopt a typical velocity width of 300 km s^{-1} for the assumed velocity of any gas in the elliptical galaxy, this limit translates into a 2.5σ upper limit of 3.1×10^9 $M_\odot$ for the hydrogen mass of the companion.

We also detected gas from two new group members G3 and G4 located 3.2$'$ and 4.2$'$ to the southwest and northwest of VII Zw 466, respectively. At the distance of the group these correspond to projected linear separations of 166 kpc and 220 kpc from the ring.

4.5 Integrated Properties

Table 4.1 presents the H I and optical properties of VII Zw 466, its two major companions (G1 and G2), and the two newly discovered dwarf galaxies, G3 and G4. The R–band luminosites, L_R, of G1 and G2 are from Appleton & Marston (1995) while the optical properties of G3 and G4 were determined from the Fick CCD images. The upper limit to the H I mass of G1 was inferred assuming a velocity width of 300 km sec^{-1} and a size of two VLA beams.

The velocity profiles of the neutral hydrogen distribution of VII Zw 466, G2 and two dwarfs are presented in the Figures 4.3–4.6.

The H I profile of VII Zw 466 presents the typical two-horned profile of a rotating disk. We estimate the systemic velocity of the ring to be 14,468 ± 15 km sec^{-1}, in close agreement with the optically determined velocity of 14,490 km sec^{-1} (Theys

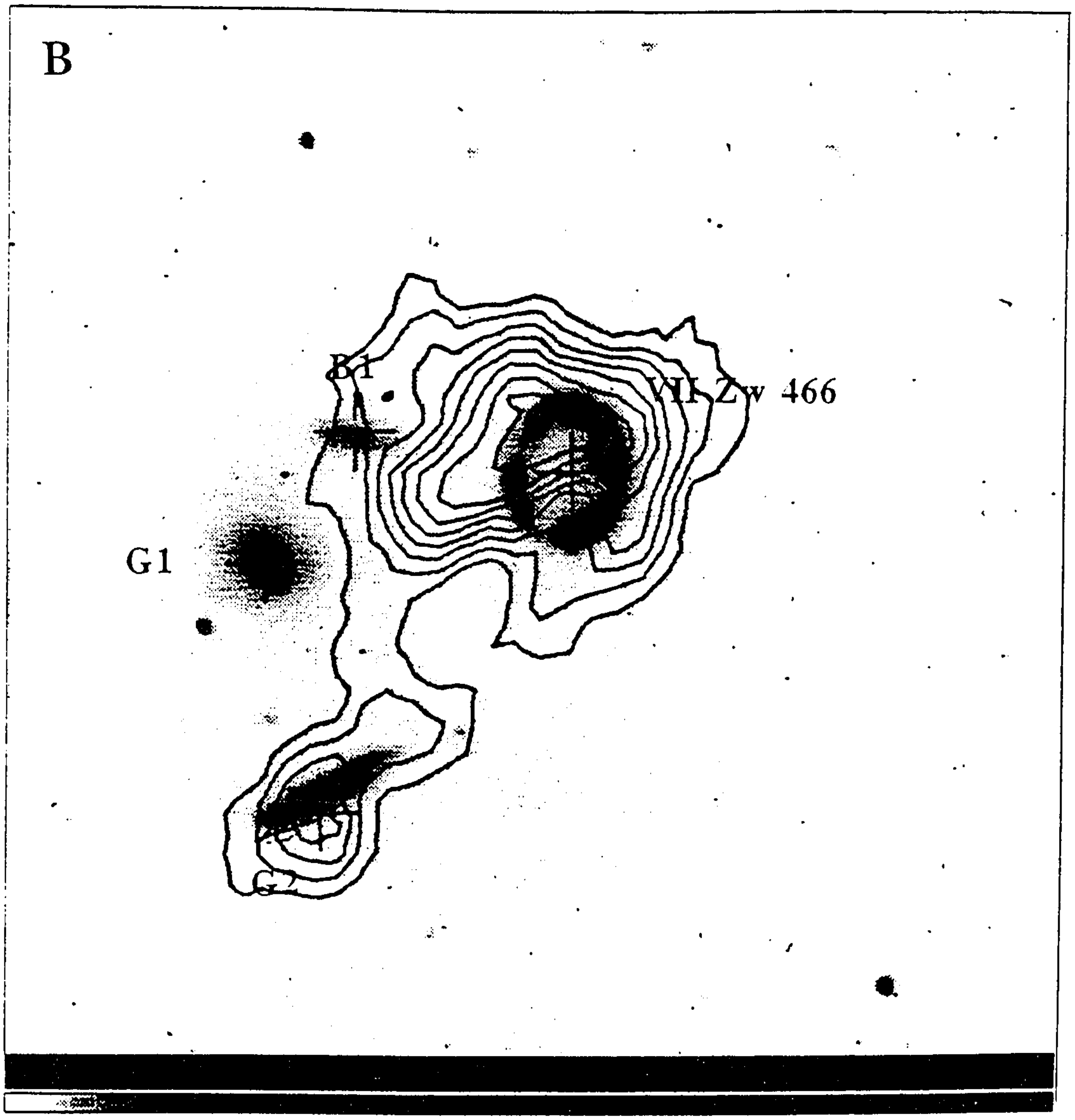

Figure 4.2: Grey-scale image of VII Zw 466 through a B–band filter overlayed with a contour map of the integrated H I distribution. The contour increment is 57.15 Jy beam^{-1} m s^{-1} and the level of the first contour is also 57.15 Jy beam^{-1} m s^{-1}.

Table 4.1: Properties of the VII Zw466 Group

	VIIZw466	Elliptical (G1)	Spiral (G2)	Dwarf-1 (G3)	Dwarf-2 (G4)
α(J2000)	$12^{\rm h}\!.32^{\rm m}\!.05.27^{\rm s}$	$12^{\rm h}\!.32^{\rm m}\!.13.30^{\rm s}$	$12^{\rm h}\!.32^{\rm m}\!.11.95^{\rm s}$	$12^{\rm h}\!.31^{\rm m}\!.37.99^{\rm s}$	$12^{\rm h}\!.31^{\rm m}\!.35.11^{\rm s}$
δ(J2000)	+66°24′13.65″	+66°23′59.80″	+66°23′19.92″	+66°22′35.56″	+66°26′55.26″
V_{HI} (km s^{-1})	14,468 ± 25	[14,100]^{a}	14,457 ± 25	14,046 ± 25	14,223 ± 25
$\Delta V_{1/2}$ (km s^{-1})	202	$\cdots$	84	113	25
$\Delta V_{1/5}$ (km s^{-1})	256	$\cdots$	119	$\cdots$	40
R_{HI} (arcsec)	11	$\cdots$	6.7	9.3	4.6
$\int S(v)dv^{b}$	0.541	$\leq 0.408^{c}$	0.155	0.383	0.092
$M_{HI}/M_{\odot}{}^{d}$	4.1×10^{9}	$\leq 3.1 \times 10^{9c}$	1.2×10^{9}	2.9×10^{9}	7.0×10^{8}
R-band mag.^{e}	14.94	14.64	15.62	16.18 ± 0.05	17.67 ± 0.10
$M_d{}^{f}$ ($M_{\odot}$)	4.2×10^{10}	3.0×10^{11}	2.3×10^{9}	8.2×10^{9g}	1.9×10^{8g}
L_R ($L_{\odot}$)	1.6×10^{10}	2.0×10^{10}	8.2×10^{9}	4.9×10^{9}	1.3×10^{9}
M_H/L_R ($M_{\odot}/L_{\odot}$)	0.26	≤ 0.16	0.14	0.59	0.56
M_d/L_R ($M_{\odot}/L_{\odot}$)	2.59	15	0.28	2.36	0.21

[a] optical velocity from Theys & Spiegel (1976)

[b] where $\int S(v)dv$ is the intergrated flux density in Jy km s^{-1}

[c] assumes a hypothetical velocity width of 300km s^{-1} and a solid angle equal to two VLA beams

[d] where $M_{HI}/M_{\odot} = D^2 \times 2.356\times 10^5 \int S(v)dv$ and D = 180 Mpc

[e] from Appleton & Marston (1995)

[f] $M_d = \frac{(\frac{1}{2}\Delta V_{\frac{1}{2}})^2 R_{HI}}{G}$ is an estimate of the the total dynamical mass of the galaxy.

[g] since the dawrf was unresolved from the B-band image we assumed an inclination $i = 45°$

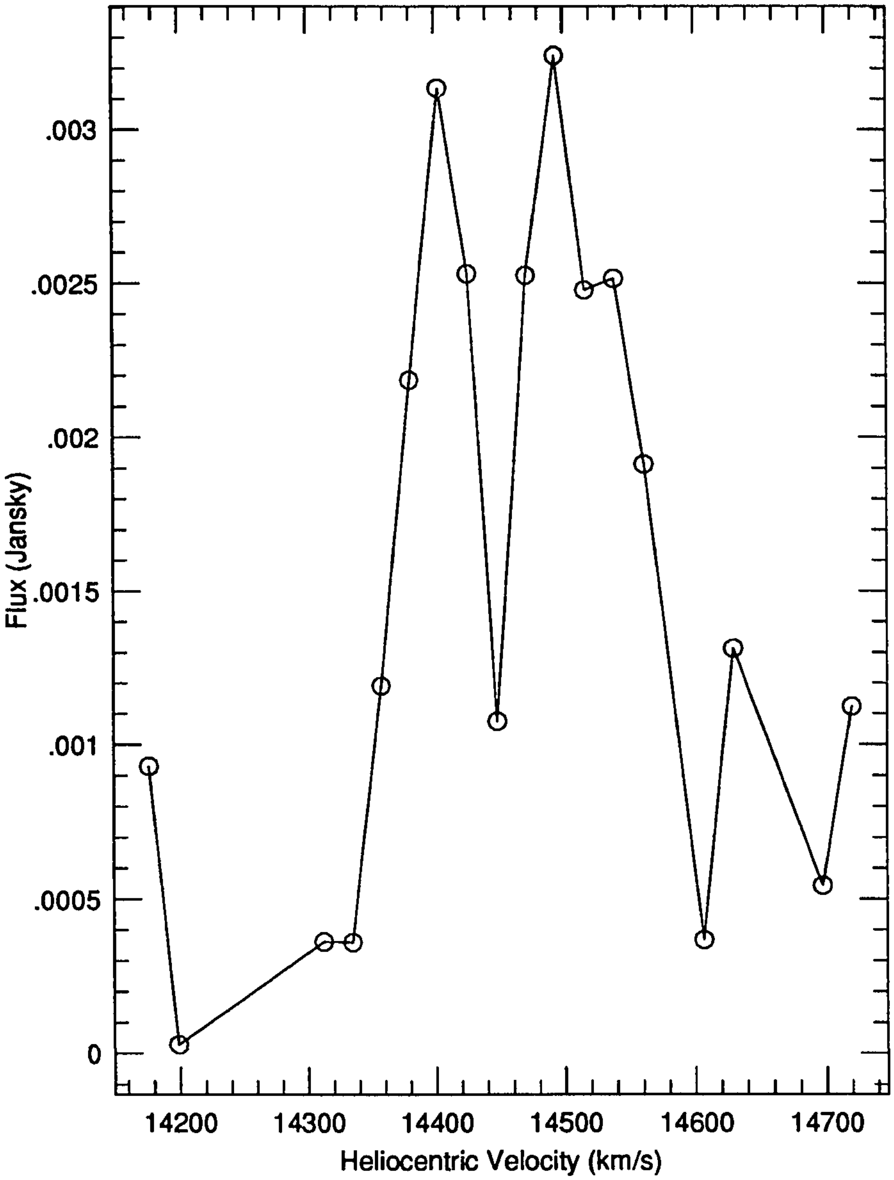

Figure 4.3: The global H I profile of VII Zw 466

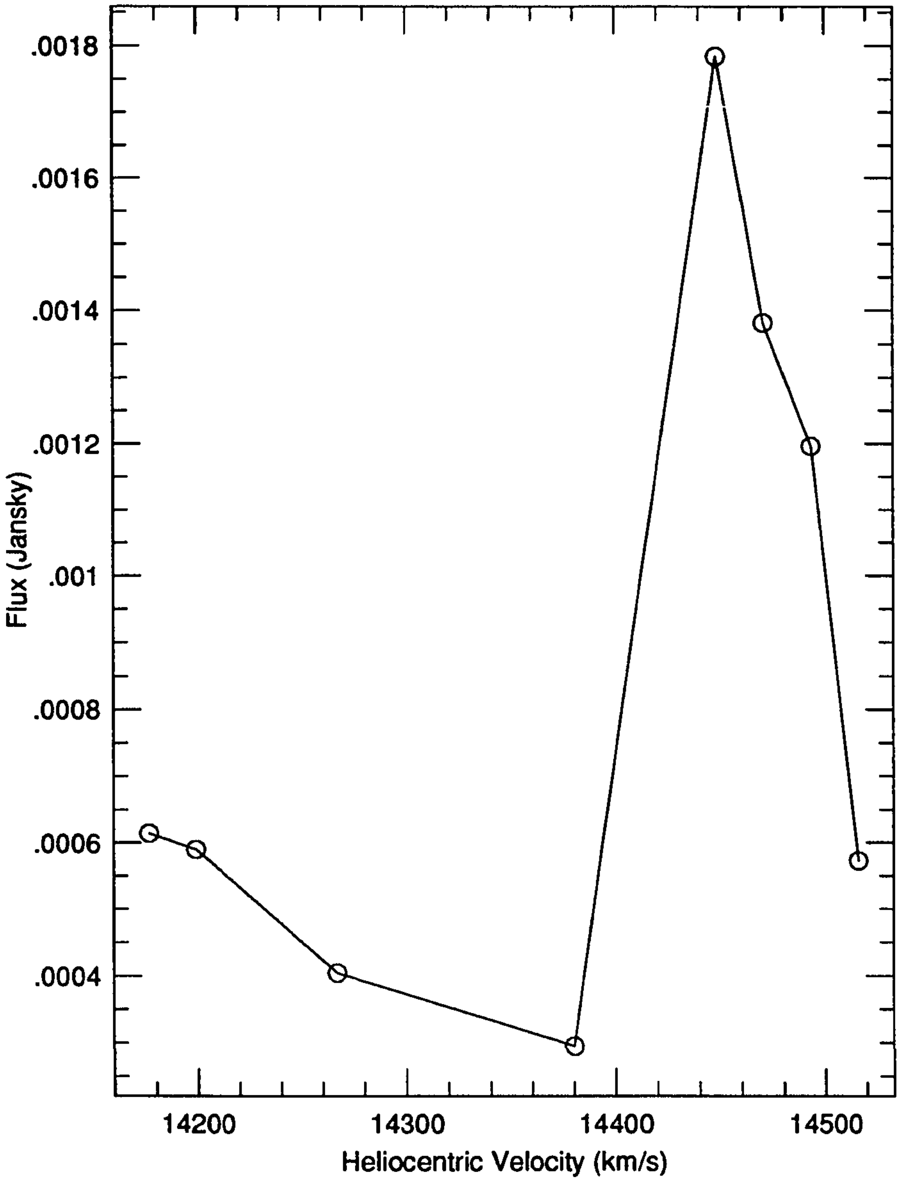

Figure 4.4: The global H I profile of the Companion Galaxy G2

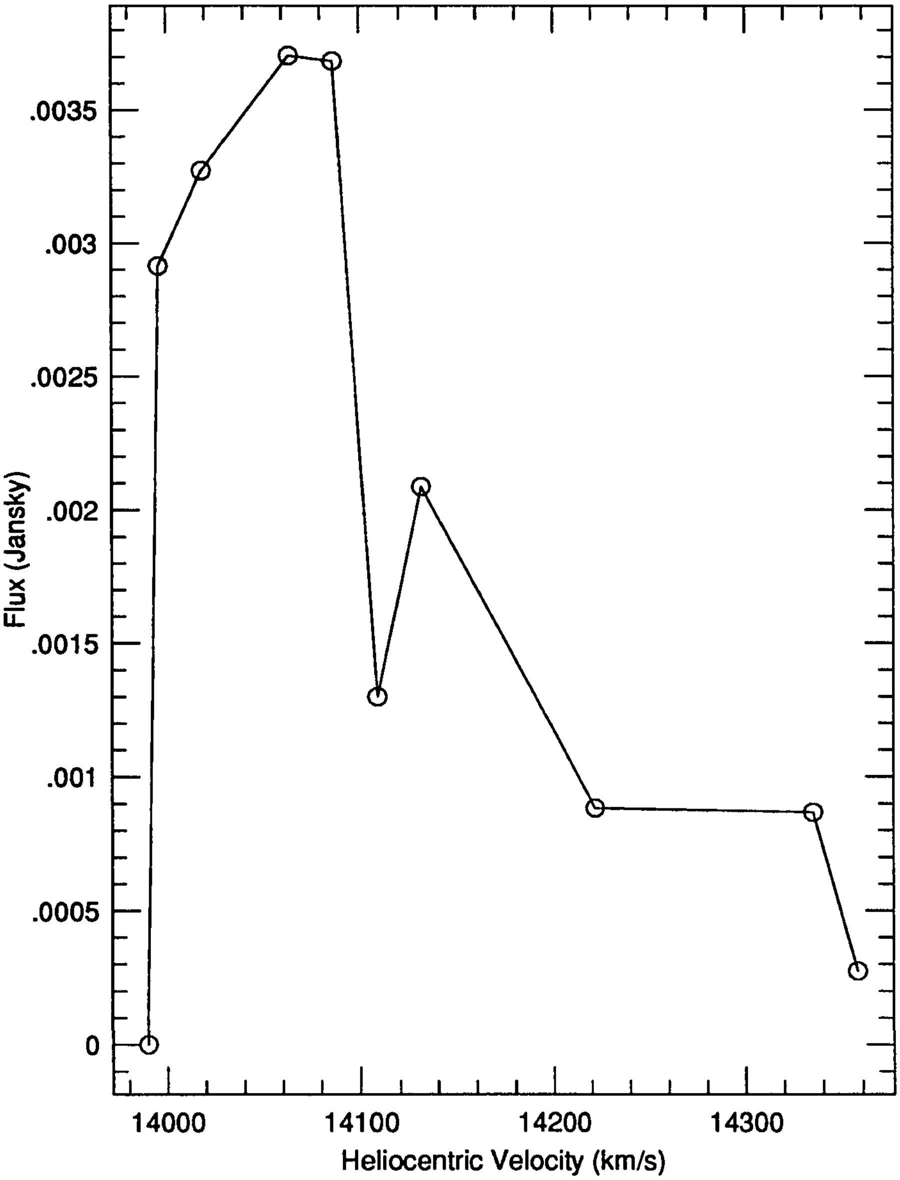

Figure 4.5: The global H I profile of the Dwarf Galaxy G3

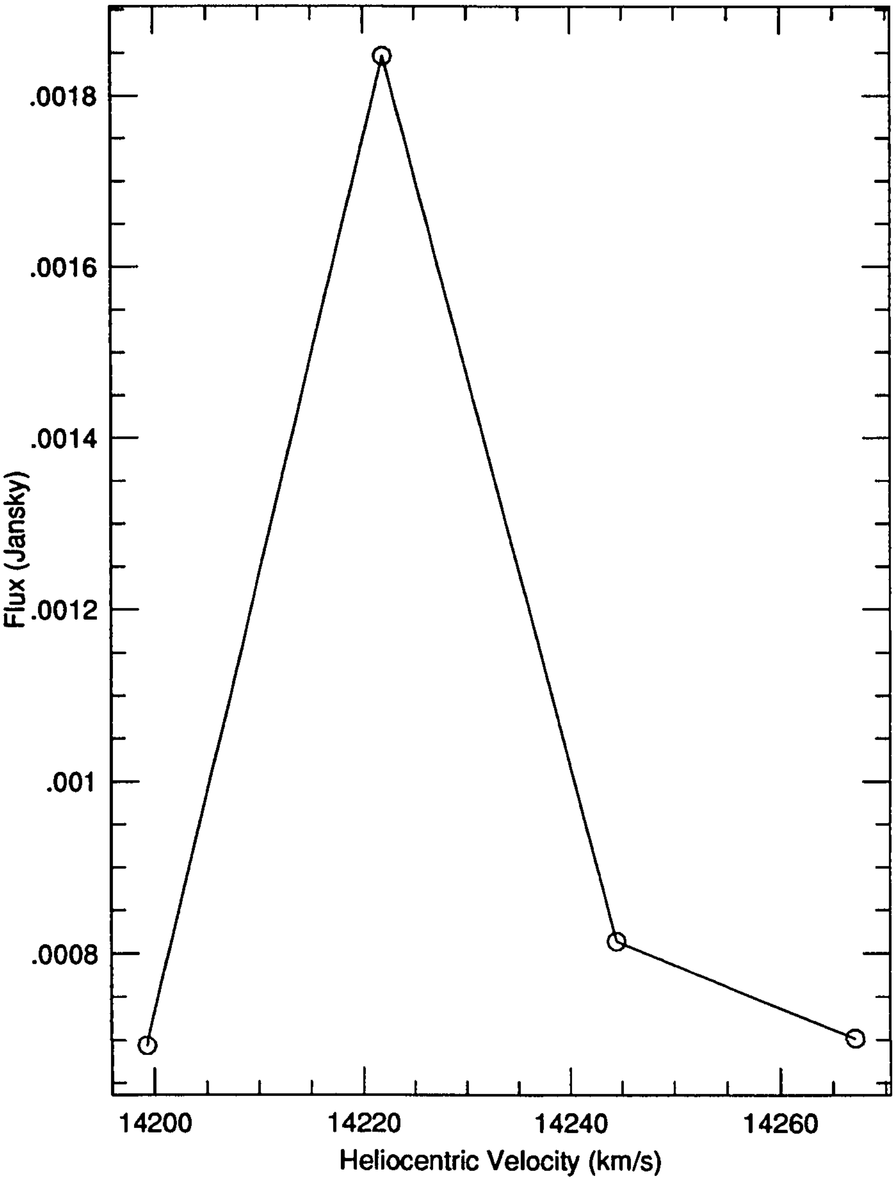

Figure 4.6: The global H I profile of the Dwarf Galaxy G4

& Spiegel 1976). However, the high velocity horn is not completely symmetrical. Emission seen at velocities higher than 14,520 $\mathrm{km\,sec^{-1}}$ is associated with the gas plumes outside of the visible galaxy.

The H I profile of G2 is fairly normal with a $\Delta V_{1/2} = 84$ $\mathrm{km\,sec^{-1}}$. The galaxy appears to be edge-on, so for all calculations we used an inclination i=90°. The two dwarfs, though, have more peculiar H I profiles. G3 exhibits an extended asymmetry around 14100 $\mathrm{km\,sec^{-1}}$ which may be due to the low signal. For this reason, even though we estimated $\Delta V_{1/2} = 113$ $\mathrm{km\,sec^{-1}}$, we did not attempt to calculate $\Delta V_{1/5}$. Finally, G4, the least massive galaxy in the group, has a very narrow H I profile with $\Delta V_{1/2} = 25.3$ $\mathrm{km\,sec^{-1}}$. For both G3 and G4 we assumed an inclination of i=45°, since the disks of the galaxies were not resolved in the optical images of the group.

We also include in Table 4.1 the dynamical mass M_d of each group member. The values of M_d corresponding to the galaxies G2, G3 and G4 were calculated using the formula:

$$M_d = \frac{(\frac{1}{2}\Delta V_{\frac{1}{2}}\,cosec(i))^2 R_{HI}}{G}$$

The estimate of the dynamical mass of VII Zw 466 was produced by the fit to the rotation of the H I ring discussed in Section 6. For completeness, the dynamical mass of G1 was simply estimated from its observed luminosity, using an R–band mass to light ratio of M/L=15, typical for ellipticals (Faber & Jackson 1976). Finally we present the mass to light ratio $\mathrm{M}_{di}/\mathrm{L}_R$ of G2, G3, G4, and VII Zw 466. We note the surprising small values of $\mathrm{M}_d/\mathrm{L}_R$ as well as $\mathrm{M}_{HI}/\mathrm{L}_R$ for the spiral galaxy G2. We believe that this may be related to tidal stripping of its mass. We will elaborate more on that in Section 6.

4.6 The Dynamical Mass of the VII Zw 466 Group

Our observations indicate that there are now four galaxies G1–G4 which form a loose group around VII Zw 466. Since we know the recessional velocities of those galaxies and their angular separations, we can use a dynamical method to get an independent estimate on the total mass of the group and subsequently, its dark matter content. This is the first time that the large-scale dark matter content of a group containing a ring galaxy has been estimated.

The primary method used is the **projected mass estimator** proposed by Bahcall & Tremaine (1981). However, for comparison we also estimated the mass of the group using a mass weighted virial theorem approach.

The projected mass method is based on the idea that, for a dynamically bound system with one massive object and several smaller companions, one can examine two extreme cases on the type of orbits of the group members. The first case assumes isotropic distribution in the velocities of the members which implies that the average value for the eccentricity of the orbits is $< e^2 >= 1/2$. The other extreme is that all orbits of the group members are radial implying that $< e^2 >= 1$. These lead us to define two specialized estimators of the dynamical mass:

$$M_I = \frac{16}{\pi G N} \sum_{i=1}^{N} v_{zi}^2 R_i$$

and

$$M_R = \frac{32}{\pi G N} \sum_{i=1}^{N} v_{zi}^2 R_i$$

where v_{zi} is the difference in the recessional velocity between the group member

i and the central massive object and R_i is its projected distance from the central object (see Bahcall & Tremaine 1981, for details).

When one has no specific information on the distribution of the eccentricities of the group one can use a dynamical mass estimator which is the average of the two extremes, that is:

$$M_O = \frac{1}{2}(M_I + M_R) = \frac{24}{\pi G N} \sum_{i=1}^{N} v_{zi}^2 R_i$$

In the VII Zw 466 group the most massive object is the elliptical G1. However, since its mass is only inferred by the mass to light ratio we will not use G1 as the central massive object. Instead, we chose to get a first estimate on the position and systemic velocity of the barycenter of the group and use the barycenter as the point of reference for our calculations of the dynamical mass of the group. Using the values of Table 4.1 we find that the barycenter is located at α_{cm}=$12^{\mathrm{h}}32^{\mathrm{m}}11.2^{\mathrm{s}}$ and δ_{cm}=$+66^{\circ}23'58.51''$ and its systemic velocity is v_{cm}=14,143 km s^{-1}. Even though this seems to compromise the independence of the method, we found that even if we had selected G1 as the central object, our estimate of the dynamical mass would only be greater by a factor of 1.83. Our tabulated results are presented in Table 4.2.

Using the values of Table 4.2, the estimate of the total dynamical mass of the group is $M_O = 3.5 \times 10^{12}$ M$_{\odot}$. If we compare this value to the sum of the dynamical masses of each individual galaxy from Table 4.1, we see that:

$$M_T = \sum_{i=1}^{5} M_{di} = 3.55 \times 10^{11} M_{\odot}$$

which implies that the amount of dark matter distributed outside the members of the group is:

Table 4.2: Parameters for the Dynamical Mass of the VII Zw 466 Group

Galaxy	$R_i{}^a$(kpc)	$v_{zi}{}^b$ (km s^{-1})	$q = \frac{R_i v_{zi}^2}{G}$ ($M_\odot$)
VII Zw 466	33.7	325	8.00×10^{11}
G1	11.0	-43	4.57×10^{9}
G2	33.9	314	7.51×10^{11}
G3	188.4	-97	3.98×10^{11}
G4	244.1	80	3.51×10^{11}

[a] Projected distance from the barycenter

[b] Velocity offset from the systemic velocity of the barycenter (v_{cm}=14,143 km s^{-1})

$$\frac{M_O}{M_T} \approx 9.9$$

Table 4.1 also shows that the total luminosity of the group is $L_{RT}=5.02 \times 10^{10}$ $L_\odot$, implying that the total mass to light ratio for the group is $(M/L)_{group} \approx 70$. Studies of groups of galaxies (Ramella, Geller & Huchra 1989) show that they have a typical (M/L) ≈ 150-300, while in compact groups (M/L)≈ 50 (Hickson *et al.* 1992). Compact groups are believed to be forming from rich loose groups are in a phase of collapse. The fact that the mass to light ratio of the VII Zw 466 group is similar to that of compact groups and also the presence of a least one observed collisional galaxy pair in the group (indicated by the presence of the ring), suggests that the VII Zw 466 group may also be in a phase of collapse.

For completeness we also calculated the mass of the group using a method based in a mass weighted virial theorem. In this approach the mass of the group is given by the formula:

$$M_{VT} = \frac{3\pi}{2G} \frac{\sum\limits_{i=1}^{5} M_{di} v_{zi}^2}{\sum\limits_{i=1}^{5} \sum\limits_{j=1,j>i}^{5} \frac{M_{di} M_{dj}}{r_{ij}}} \times \sum_{i=1}^{5} M_{di}$$

where M_{di} is again the dynamical mass of a group member i and r_{ij} is the the projected distance between the members i and j. This results to a group mass M_{VT} = 6.2 10^{12} $M_{\odot}$, which is only 1.78 times larger than the projected mass method estimate.

The previous analysis is based in the crucial underlined assumption that the group is in virial equilibrium. To verify that, we estimated the crossing time of the group $t_c = L/V$ (Jackson 1975)

where

$$L^2 = \frac{3\sum\limits_{i=1}^{5} M_{di} R_i}{2\sum\limits_{i=1}^{5} M_{di}}$$

and

$$V^2 = \frac{3\sum\limits_{i=1}^{5} M_{di} v_{zi}^2}{\sum\limits_{i=1}^{5} M_{di}}$$

For the VII Zw 466 group the crossing time is $t_c = 2.1 \times 10^8$ yrs, so the group does fulfill the condition of virial equilibrium ($t_c \ll H_o^{-1}$).

We believe that the projected mass method estimate is more accurate than the one resulting from the virial theorem technique. Bahcall and Tremaine (1981) have shown that the virial theorem technique may be biased and inefficient in particular for systems with small number of members. Their numerical simulations suggest that the projected mass method is much more accurate. In addition, it has the added advantage that it explicitly takes into account the possibility that some or all of the orbits in the group are radial. The later reason is very relevant in this study. Unlike most group studies, we do know that in the VII Zw 466 group, at least two of the galaxies (G2 and VII Zw 466) must have collided radially in order to produce the ring.

However, we would like to caution the reader that both the projected mass method and the virial mass method are valid only if the group is gravitationally bound. If some of the galaxies are leaving the group, or are chance projections of foreground or background galaxies, then the resulting dynamical mass would be incorrect and should be treated only as an upper limit. Due to these uncertainties the values for the dynamical mass and mass to light ratio of the VII Zw 466 group should be regarded as simply our best estimates.

4.7 The H I Kinematics of the Ring

In order to understand the kinematical behavior of the H I gas in the ring of VII Zw 466, we used a model which assumes that the ring may be both rotating and expanding. This model has been used successfully in other ring galaxies, such as the Cartwheel (Fosbury and Hawarden 1977; Higdon 1993). Using the optical B–band image of the group and assuming an intrinsically circular ring, we estimated the inclination of the ring to be $i = 37^{\circ}$and the position angle of the major axis to be -5°(N through E). Then, we measured the velocities of the H I gas along azimuth of the ring and performed a three parameter fit using the following function:

$$v = a_0 + a_1 sin(\phi + \phi_0) \tag{4.1}$$

where a_0, a_1 and ϕ_0 were the free parameters. A rotating and expanding ring would exhibit a simple sinusoidal shape, with a phase offset from the major axis that is related to the amplitude of the expansion. The formal fit for the ring resulted in a χ^2=5.61. However, the points of the northeast quadrant of the ring exhibit a peculiarity indicating a small H I plume, and the errors associated with them are larger. If we exclude those points, (which is reasonable since we are only trying to model the ring) the fit improves considerably, giving a χ^2=2.77 for a_0=14,500 $\mathrm{km\,s^{-1}}$, a_1=83 $\mathrm{km\,s^{-1}}$, and ϕ_0=274°. This fit is presented in Figure 4.7. Since the systemic velocity of the ring is v =14,468 $\mathrm{km\,s^{-1}}$, the expansion velocity of the ring would be v_{exp}=32 $\mathrm{km\,s^{-1}}$. The rotation curve would reach a maximum $v_{max}=a_1/sin(i)$=137 $\mathrm{km\,s^{-1}}$ at radius of the ring.

In Figure 4.8 we also present the channel maps of the H I observations. In the rest frame of the galaxy, the channel separation is 22.66 $\mathrm{km\,s^{-1}}$. The velocity of each channel is displayed in the upper right corner.

H I emission from the VII Zw 466 is detected for the first time around 14,561 $\mathrm{km\,s^{-1}}$ and originates from the southern side of the optical picture. As we move to lower velocities, the emission is typical of a rotating ring. We observe that the emission splits in two centroids located to the east and west of the optical ring. However, the eastern centroid does not overlap spatially with the optical picture of the ring. It resides at the outside of the optical ring structure and at 14,470 $\mathrm{km\,s^{-1}}$ is deformed into a small plume (hereafter "Plume A") pointing to the southeast. The amount of H I gas associated with this plume is M_A=1.6 × 10^8 $M_\odot$. The

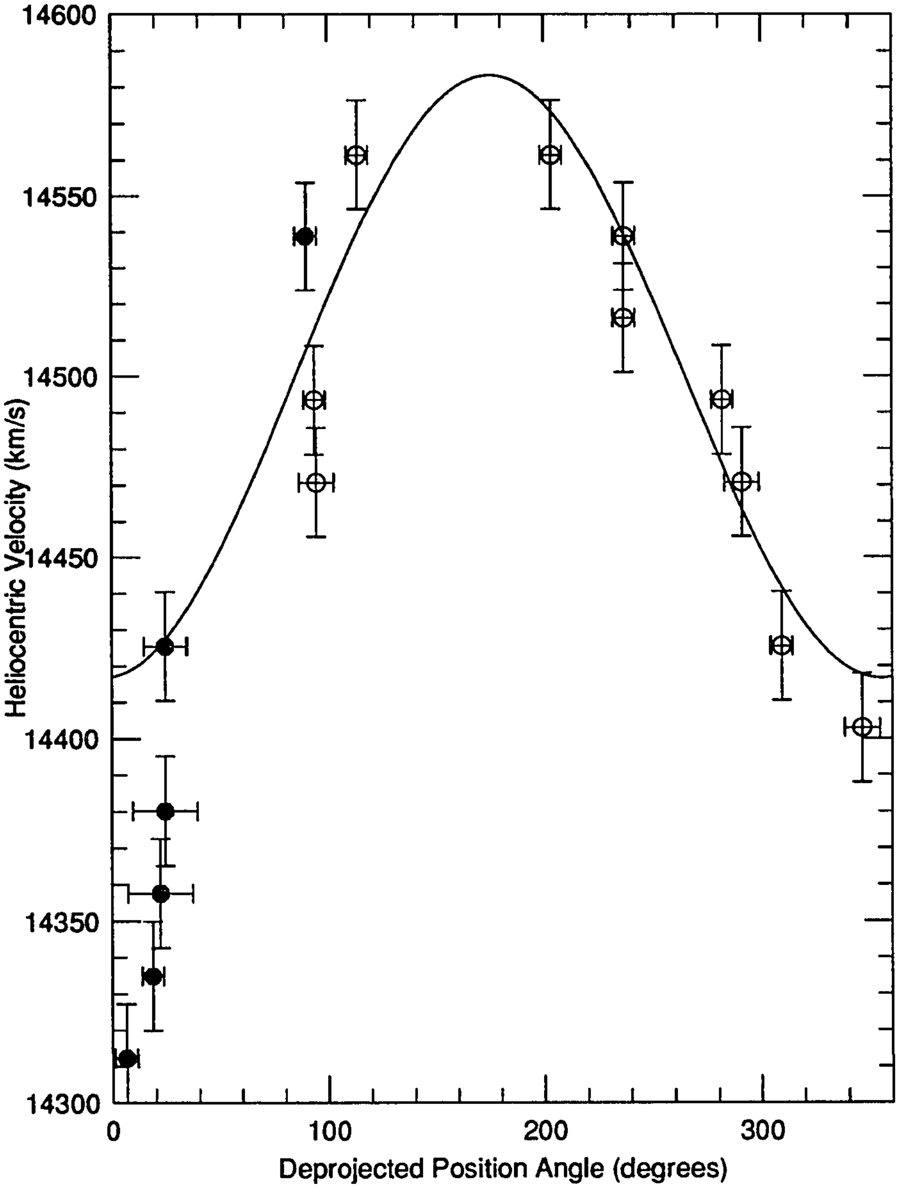

Figure 4.7: The HII velocity as a function of azimuth along the ring. The solid circles were excluded from the fit.

emission from the western centroid does coincide with the optical structure. It is also considerably stronger, indicating large quantities of gas. Strong emission from the west side of the ring was also detected in the radio continuum observations of the galaxy (Ghigo & Appleton, in preparation).

As we proceed to channel maps with velocities below 14,470 $\mathrm{km\,s^{-1}}$, we see a very disturbed behavior of the gas. Firstly, we notice that at 14,448 $\mathrm{km\,s^{-1}}$ there is practically no H I gas associated with the ring. This is very peculiar since there is a strong emission in the preceding and following channel maps. Also, there is a filament (hereafter "Plume B") of H I gas present in three consecutive channel maps (14,402 $\mathrm{km\,s^{-1}}$ - 14,357 $\mathrm{km\,s^{-1}}$). This is the strongest emission that we observe. The filament initially points to the northeast of the ring and as we progress to lower velocities, it points to the east-southeast of the ring in the general direction of the companions G1 and G2. We calculated that the H I gas associated with plume B is M_B=4.2 × 10^8 $M_\odot$.

At this point, it also useful to discuss the H I emission from the companion G2. The emission from G2 is located in the channel maps between 14,516–14,334 $\mathrm{km\,s^{-1}}$. However, we do notice some H I gas at a velocity of 14,584 $\mathrm{km\,s^{-1}}$ and a lack of H I gas at 14,425 $\mathrm{km\,s^{-1}}$. Moreover, the emission centroid from G2 in the channel maps after 14,425 $\mathrm{km\,s^{-1}}$ is rather elongated pointing clearly towards the ring galaxy. Table 4.1 shows that the value of M_{HI}/L_R for G2 is also unusually low for a late-type spiral, suggesting that it has been tidally stripped. (We also note that the total mass to light ratio of G2 is extremely low, implying that the dark matter halo of G2 has also been stripped, a common effect in strong tidal interactions; Barnes & Hernquist 1992).

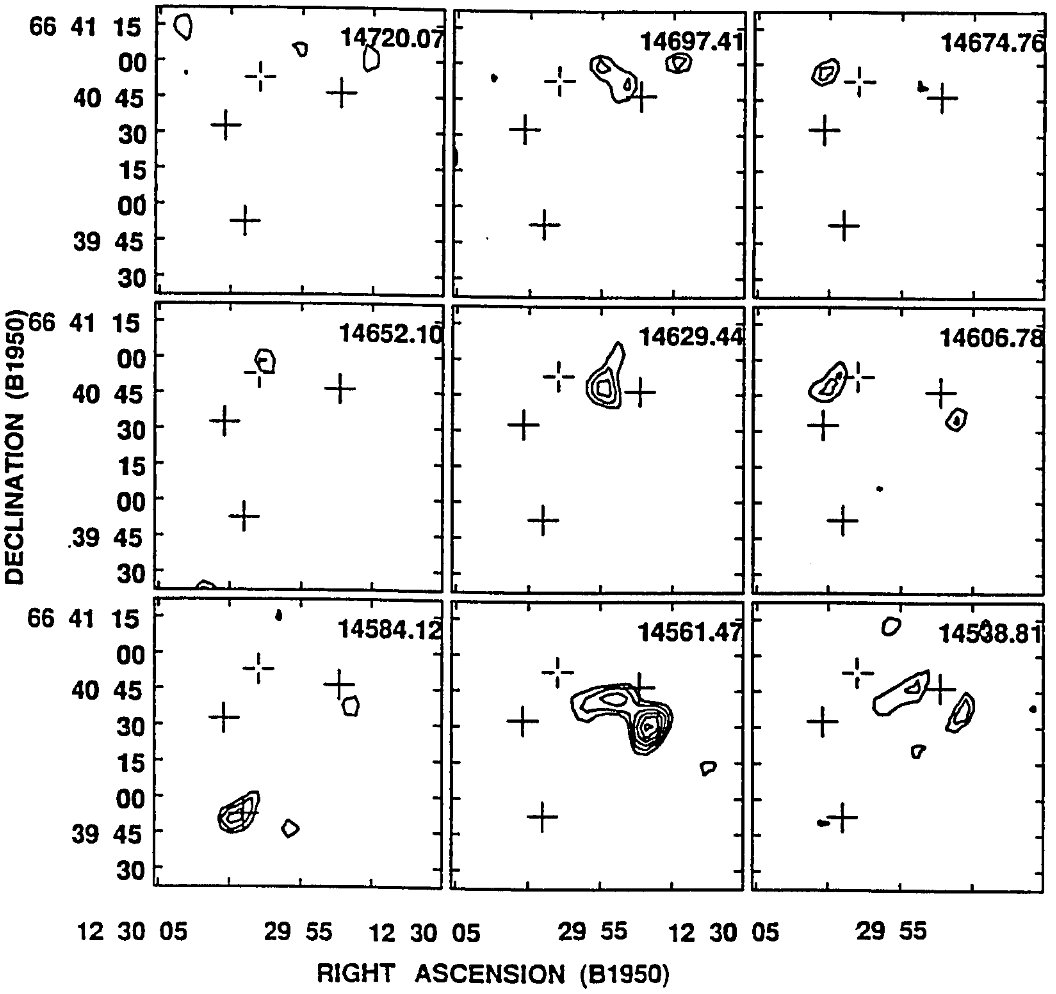

Figure 4.8: Contour plots of the 27 channel maps of VII Zw 466. The velocity of each channel is displayed in the upper right corner. The contour increment is 1.35×10^{-4} Jy beam^{-1} (0.5 σ level) and the lowest contour displayed is at 2.5σ. The solid crosses indicate the position of the ring, G1, and G2, while the open cross indicates the position of the background galaxy B1.

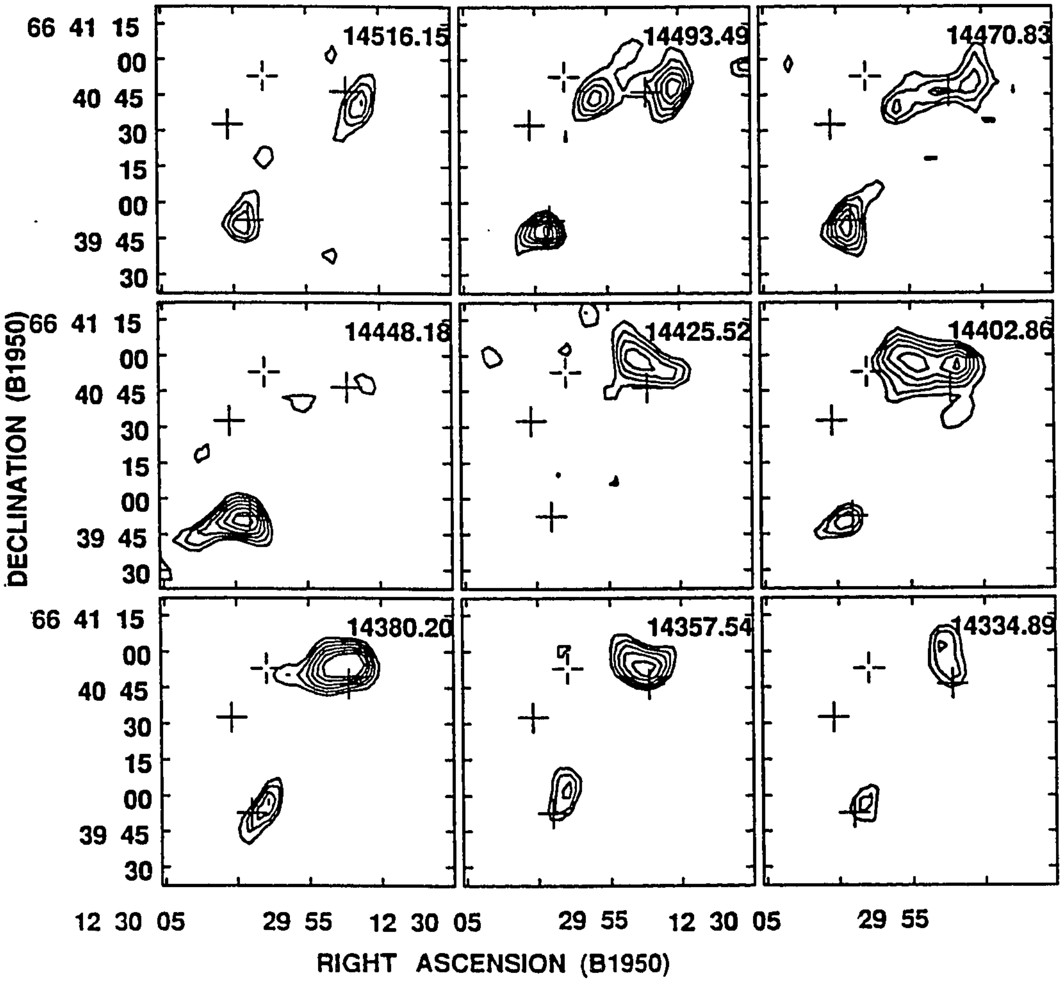

Figure 4.8 (Continued)

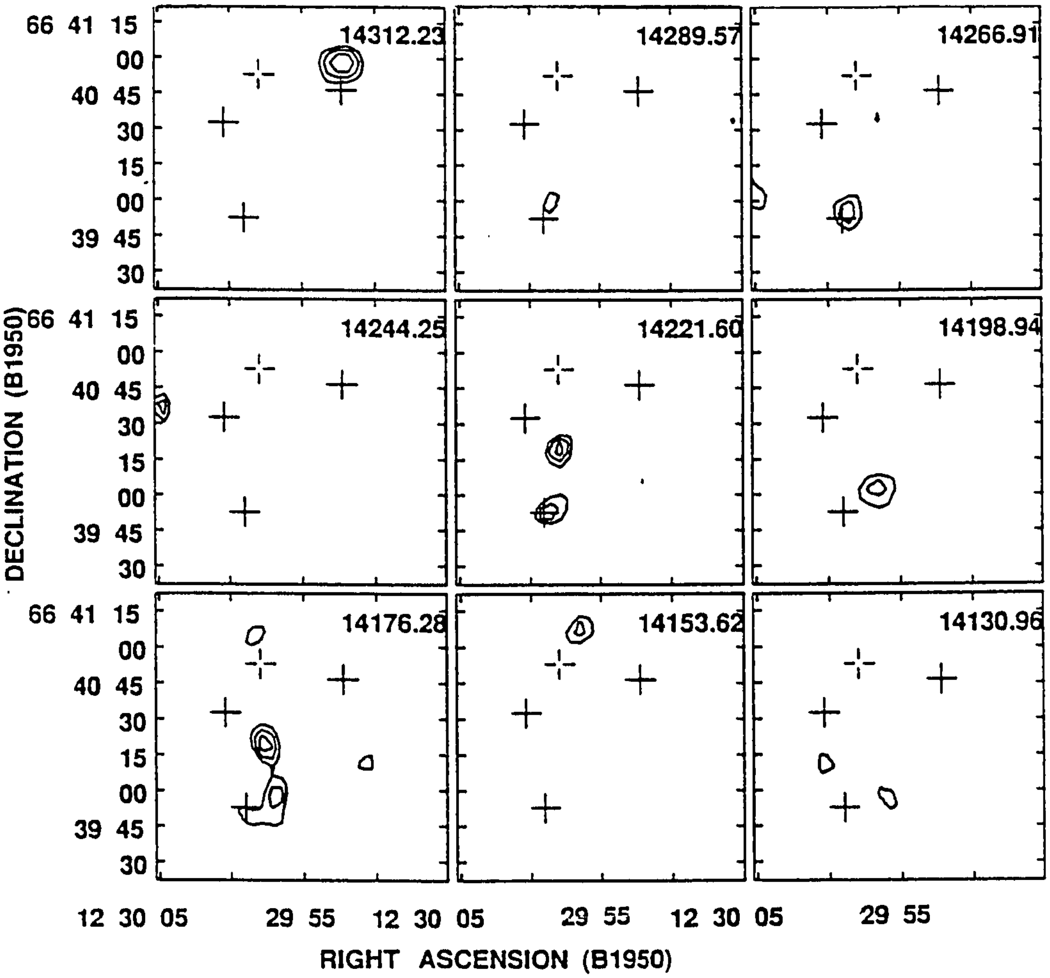

Figure 4.8 (Continued)

The dynamical behavior of the H I gas is consistent with G2 being the galaxy that disturbed the progenitor H I disk of VII Zw 466 and caused the formation of an expanding star forming ring. Numerical simulations of the gas dynamics in nearly head-on collisions between a large gaseous disk galaxy and a smaller companion disk galaxy (Struck 1995) have shown that large quantities of gas are stripped away from the disk of the target galaxy by the companion during the collision. Most of the ejected material either falls back to the large disturbed disk or it spirals towards the smaller companion which eventually accretes it. The lack of H I emission from G2 at 14,425 km s^{-1} and the morphology of the gas at the following channel maps can be explained by considering this gas as material that is falling back to the companion G2. Plume A and plume B may contain the gas of VII Zw 466 which was splattered away from its disk during the collision and now constitutes the relics of an H I bridge which was formed during the passage of G2 through the disk. The total amount of H I gas in plumes A and B is $M_A+M_B = 5.8 \times 10^8$ $M_\odot$, which is approximately 16% of the mass of the H I disk of VII Zw 466.

To further estimate the energy needed to generate the two H I plumes, we performed an order of magnitude calculation of the kinetic energy of the gas in the plumes. We used the H I masses given above and the relative velocities of plumes A and B Δv_A = 14 km s^{-1} and Δv_B = 88 km s^{-1} with respect to VII Zw 466. The kinetic energy associated with their gas was found to be $KE_A = 3.1 \times 10^{53}$ ergs and $KE_A = 3.2 \times 10^{55}$ ergs respectively. Although projection effects are not included, this implies the energy required to displace the plumes from VII Zw 466 is of the order of 10^{55} ergs. This is approximately 10% the gravitational potential energy of the VII Zw 466 - G2 pair, indicating that the collisional scenario is plausible.

From this energy estimate, it is most likely that G2 collided with VII Zw 466 while moving in a near parabolic orbit from the west to the southeast. Some of the H I gas from both G2 and VII Zw 466 has been ejected from the disk plane forming an H I bridge connecting the two galaxies. As G2 moved further away from the ring, the H I bridge broke apart (or became too faint to be detectable). All that remains is the disturbed emission observed in the channel maps with velocities between 14,402–14,357 km s^{-1}.

4.8 Conclusions

In the previous sections we presented our H I observations of the VII Zw 466 group. Though only at moderate resolution due to the large redshift (z=0.048) of the group, we were able to draw the following conclusions :

- The H I emission from VII Zw 466 is consistent with that of a rotating and expanding ring. A simple kinematical model fits the ring sufficiently well and indicates a rotation curve with v_{max} = 137 km s^{-1} at the radius of the ring, and an expansion velocity v_{exp}=32 km s^{-1}. However, one quadrant of the ring has anomalous velocities.

- The northern part of the ring shows evidence of the tidal interaction. Plumes of H I gas (5.8×10^8 $M_\odot$, or 16% of the total H I disk) lie outside the ring and point in the general direction of the two nearby group members. The dynamics of this gas is consistent with a collisional origin for the ring. The plumes may represent either gas ejected from the progenitor of the ring galaxy or may be material tidally stripped from the suspected intruder galaxy (see recent models of Struck 1995; Appleton and Struck 1995).

- From the two known companions, only the edge-on spiral (G2) contains neutral hydrogen above our detection limits. The H I emission from the companion G2 also shows a plume towards the direction of VII Zw 466. This fact, in addition to the peculiar global properties of the galaxy (e.g. very low M_{HI}/L_R and M_d/L_R), strongly indicate that G2 is the intruder galaxy that collided head-on with VII Zw 466 and created the ring (Lynds & Toomre 1976). It is likely therefore that the elliptical galaxy G1 has played little role in the ring formation, despite its unusual "boxy" optical isophotes (Appleton and Marston 1995).

- We identified two new members of the VII Zw 466 group. These galaxies are dwarfs and are detected for the first time in H I.

- The upper limit of the dynamical mass of the group was estimated using the projected mass method and was found to be $M_O = 3.5 \times 10^{12}$ $M_\odot$. We would like to emphasize that even though we calculated the group mass using other techniques, such as mass and non-mass weighted virial theorem methods we consider this estimate the most reliable (see Section 5). The resulting mass implies that the dark matter, not associated with the group members, is 9.9 times greater than the sum of the dynamical masses of all group members. The resulting mass to light ratio for the group is $(M/L)_{group} \approx 70$.

Overall, the H I emission from VII Zw 466 is not very strong. It would be very difficult to improve our resolution by observing the group with the B Configuration of the VLA, since one would have to observe the galaxy for more than 15 hours. However, high resolution VLA observations of the radio continuum emission have recently been made (Ghigo and Appleton, in preparation), which will further help in understanding the dynamics of this galaxy.

4.9 Acknowledgments

We thank C. Struck and R.J. Lavery (Iowa State University) for stimulating discussions on general galaxy interactions. We are grateful to E. Brinks (NRAO, Socorro) for useful suggestions during the VLA data This work is funded under NSF grant AST-9319596.

4.10 References

Appleton, P. N. Kawaler, S. D. & Eitter, J. J., 1993, AJ, 106, 1973

Appleton, P. N. & Marston T. 1995, AJ, (submitted)

Appleton, P. N. & Struck, C. 1995, In *Fundamentals in Cosmic Physics* (Amsterdam: Overseas Publishers Association), (in press)

Arp, H. C. 1966, Atlas of Peculiar Galaxies (Pasadena: California Institute of Technology)

Bahcall, J. N & Tremaine, S., 1981, ApJ, 244, 805

Barnes, J. & Hernquist, L. 1992, Ann. Rev. Astron. Astrophys., 30,705

Butcher, H.R. & Oemler, A.,Jr., 1984, ApJ, **285**, 426

Charmandaris, V. & Appleton , P. N. 1996, ApJ, (in press)

Charmandaris, V., Appleton , P. N. & Marston T. 1993, ApJ, 414, 154 (CAM)

Dressler, A., Oemler, A.,Jr., Butcher, H. R. & Gunn, J. E. 1994, ApJ, 430, 107

Faber, S. M. & Jackson, R. E. 1976, ApJ, 204, 668

Fosbury, R. A. E. & Hawarden, T. G. 1977, MNRAS, 178, 473

Ghigo, F. & Appleton, P. N. 1996 (in preparation)

Hickson, P., de Oliveira, C. M. Huchra, J. P & Palumbo G. G. C., 1992, ApJ, 399, 353

Higdon, J. L. 1993, Ph.D. Thesis, University of Texas at Austin

Hogbom, J.A. 1974, A&A, 15, 417

Jackson, R. E. 1975, MNRAS 173, 41

Landolt, A. U., 1992, ApJ, 104, 340

Lavery, R. J. *et al.* 1995, ApJ, (submitted)

Lavery, R. J. & Henry J.P.,1988, ApJ, 330, 596

Lynds, R. & Toomre, A. 1976, ApJ, 209, 382

Malin, D.F. & Carter, D. 1980, *Nature*, 285, 643

Marcum, P. N, Appleton, P. N & Higdon, J. L 1992, ApJ, 399, 57

Marston T. & Appleton, P. N. 1995, AJ, 109, 1002

Oemler, A.,Jr., 1995, IAU Symposium No. 171, Heidelberg, Germany

Ramella, M., Geller, M. J. & Huchra, J. P. 1989, ApJ, 344, 57

Schweizer, F. & Seitzer, P. 1988, ApJ, 328, 88 (SS88)

Struck, C., 1995, "Radial Density Waves", in *Minnesota Lectures on Extragalactic HI* ed. E. Skillman (ASP, San Francisco)

Theys, J. C & Spiegel, E. A. 1976, ApJ, 208, 601

Thomson, L. A & Theys, J. C 1978, ApJ, 224, 796

Toomre, A. & Toomre, J. 1972, ApJ, 405, 142

Vorontsov-Velyaminov, B. A. 1977, Atlas of Interacting Galaxies, A&AS, 28, 1

CHAPTER 5. COMPUTATIONAL TECHNIQUE

5.1 Introduction

The study of galaxy interactions by means of computer modeling has been an ever expanding research area over the past 25 years. The seminal paper of "Galactic Bridges and Tails" by Toomre & Toomre 1972, which contains a series of numerical experiments clearly demonstrated for the first time that dynamical effects of galaxy interactions can have profound effects on the morphology and evolution of galaxies.

Initially the numerical studies of galaxies were unable to model the stellar and gaseous content in a self-consistent manner (Hockney & Eastwood 1988). The studies of the stellar dynamics were performed using either direct N-Body (e.g. Aarseth 1972;1985) or restricted three-body codes (e.g. Toomre and Toomre 1972). The N-Body codes had problems achieving high resolution since they scale as O(N^2) where N is the number of particles. Even with the current resources, running such codes is extremely expensive computationally. The restricted three-body codes treated each galaxy as a rigid halo with test particles that did not affect the potential. As a result, they could not fully explain the dynamics of mergers and violent interactions since they underestimated the effects of dynamical friction. Several models were also developed using Particle Mesh techniques (e.g. Sellwood 1987; Gerin, Combes and Athanassoula 1990). These types of models enabled the use of large N, but had problems treating large density gradients. The study of gas dynamics in galaxies is performed using a variety of numerical techniques. One of the most popular, though somewhat controversial, methods is Smooth Particle Hydrodynamics (SPH) (Monaghan 1985; Monaghan and Lattanzio 1985). This is a grid-less particle method for solving the Lagrangian equations of hydrodynamics.

A major step in the numerical galactic dynamics was the development of new approximation methods, known as hierarchical tree methods. Using tree methods the computation time of force calculations scales as O(N*log(N)), a fairly dramatic reduction relative to direct N-Body calculations for large N. A well known algorithm is the one developed by Barnes and Hut (1986). The algorithm was written in Fortran for scalar and vector processors by Hernquist (1987). A tree version of SPH was also developed by Hernquist and Katz (1989).

Currently, most researchers perform studies of interacting galaxies using scalar or vector codes which combine N-body and SPH (Gerber, Lamb, and Balsara, 1992; Weil and Hernquist, 1993; Horellou and Combes, 1993). Their results give strong indications that the simultaneous modeling of both stellar and gas component in the numerical experiments is essential if we want to understand fully the physical processes that dominate during the interaction. There have been some first attempts to include simple star formation in simulations of interacting systems (Mihos, Richstone and Bothun 1992; Mihos and Hernquist 1994)

The latest advances in parallel computing provide us for the first time with parallel algorithms for hierarchical tree codes. The pioneering work of Warren and Salmon (1994) using the 512-processor Intel Touchstone Delta at Caltech showed that this non-trivial problem could be solved. Using a similar technique, Olson and

Dorband (1994) developed a highly efficient N-Body tree code for MasPar, a SIMD parallel computer.

In this chapter I will present in detail the way one can study the dynamics of the stellar component of a galaxy by means of numerical modeling. I will give more emphasis to the code that was developed here and highlight several important issues that need to be considered in order to develop an efficient high performance code. In the Appendix, I also provide a copy of the code which resulted of our work.

5.2 Galaxies as Collisionless Stellar Systems

A self-gravitating system is collisionless if the granularity of its mass distribution does not influence its evolution. Gas poor galaxies fit fairly well the definition of a collisionless system. This can be easily seen if one makes a back on the envelope calculation of the mean free path of a star in a galaxy before it collides with another star (Binney & Tremaine 1987, §1.1). For a group of stars moving along a straight line the mean free path is $\lambda = 1/(n\ \sigma)$, where n is the number density of the stars and σ is their typical cross section. Assume that all stars are similar in radius to the Sun ($R_\odot = 6.96 \times 10^{10}$ cm) , their number density is similar to the average number density of the disk of our Galaxy $n = 0.3$ pc^{-3} (1 pc = 3.086×10^{18} cm) and that the typical stellar velocity at a given location is $v \approx 40$ km s^{-1}. Then the mean free path between two star collisions will be $\lambda = 1.5 \times 10^{33}$ cm and the characteristic time interval between the two collisions will be $\lambda/v \approx 10^{19}$ years. This is 9 orders of magnitude greater than our current estimate of the age of the Universe. Hence, it is obvious that we can treat the stellar component of a galaxy as a collisionless system of N particles bound together by their mutual gravitational attraction.

Before we discuss how one can dynamically model such a system we need to keep in mind two associated time-scales, t_c the crossing time and, t_r, the relaxation time (Binney & Tremaine 1987,§4.1). These are given by :

$$t_c \simeq \sqrt{\frac{1}{G\rho_h}} \qquad \text{and} \qquad t_r \simeq \frac{N}{8 ln N} t_c$$

where G is the gravitational constant and ρ_h is the average density within the contour containing half the mass. The crossing time t_c corresponds to a typical orbital period of a star in the galaxy, while the relaxation time t_r is the time over which the orbit of the star changes significantly by the cumulative effects of the interactions with the other stars of the systems. Over intervals much smaller than t_r, one can neglect the effects of two body interactions and if $t_c \ll t_r$, it is safe to consider that the system evolves collisionlessly.

In this case, and for large N, we can describe the dynamical evolution of the galaxy in the phase-space using the statistical approach of the Collisionless Boltzmann Equation (hereafter CBE) :

$$\frac{\partial f}{\partial t} + \vec{v} \cdot \frac{\partial f}{\partial \vec{r}} - \nabla \phi \cdot \frac{\partial f}{\partial \vec{v}} = 0$$

where $f(\vec{r}, \vec{v}, t) d^3\vec{r} d^3\vec{v}$ is the total mass of the stars in the phase-space volume $d^3\vec{r} d^3\vec{v}$ centered on $(\vec{r}, \vec{v})$ at time t. The distribution function f completely describes the dynamical state of the system (Binney & Tremaine 1987, § 4.1).

The gravitational potential $\phi(\vec{r}, t)$ of the distribution at any given time t can be calculated by Poisson's equation :

$$\nabla^2 \phi = 4\pi G \int f d^3\vec{v}$$

5.3 Solving the CBE

There are several methods that can be used to solve the CBE. The most efficient computationally is the Monte-Carlo approach (White 1983) where one constructs an *N-body realization* of the system by choosing the phase-space coordinates $(\vec{r}_i, \vec{v}_i)$ of all N particles with probability proportional to $f(\vec{r}_i, \vec{v}_i, t)$. Then a mass is assigned to each one so that the CBE is satisfied. Then the N-body realization is evolved solving the Newtonian equations of motion,

$$\frac{d\vec{r}_i}{dt} = \vec{v}_i, \qquad \frac{d\vec{v}_i}{dt} = -\nabla\phi|_{\vec{r}=\vec{r}_i}$$

Even though this process seems fairly simple, there are two major obstacles to this approach.

- The first is the development of the initial N-body realization. Galaxies are fairly complicated multicomponent structures. They usually have a bulge, a disk and a halo component. It is not trivial to set up a distribution of particles in the phase-space which satisfies the CBE and in the same time approximates the appearance of the physical system (i.e. galaxy) which one wants to study. Only recently has a satisfactory theory been proposed which addresses the issue and presents a recipe on how to construct multicomponent N-body systems (Hernquist 1993). We will not elaborate on this technique since it is beyond the scope of this chapter, though we will briefly refer to it in the end.

- The second is the actual calculation of the acceleration (which requires the knowledge of the potential ϕ) at the position of any given particle.

A naive approach in the calculation of the acceleration on a given particle would be to simply sum up the contribution of all other particles. Then the acceleration of the whole system would be computed by a simple double loop. Since the stellar component of galaxies is $O(10^{11})$ it is very desirable to construct models using as many particles possible. As we have mentioned though in the introduction of this chapter, an approach of a direct summation is impractical for large values ($\gg O(10^5)$) of N since it scales as N^2. Even with the computational power available today, it would be impossible to do any meaningful numerical experiments due to the extreme expense in CPU time.

Several other methods for calculating the gravitational acceleration have been described in the literature (Sellwood 1987; Hockney & Eastwood 1988). Many of these methods (PIC, P3M, etc), especially those developed for systems with simple geometry, are very fast computationally. However the gain in speed leads to sacrificing the generality of the problems that can be solved (in case of expansion techniques), or the spatial resolution that can be achieved(for 3-D Fast Fourier Methods).

Another group of fairly fast and completely general methods have been developed over the past 10 years. They are known as *Hierarchical N-body Methods.* The code that we developed was based on such a method and we elaborate more on the those methods in the following section.

5.4 Hierarchical "Tree" Methods

The basic idea of the hierarchical "tree" methods is that the contribution to the potential at the position of a particle i from a group of particles "sufficiently far away" can be approximated as a contribution due to a single mass point (plus perhaps few small correction terms). More formally, the gravitational potential due to a distribution of particles with a center of mass at position $\vec{r}$ can be be written in a form of multipole expansion :

$$\phi(\vec{r}) = -4\pi G \sum_{l=0}^{\infty} \frac{1}{2l+1} \sum_{m=-1}^{l} Y_{lm}(\theta, \phi) \sum_{i=1}^{N} m_i Y^*_{lm}(\theta_i, \phi_i) \frac{r_i{}^l}{r^{l+1}}$$

where Y_{lm} are the spherical harmonics. Since the terms of the expansion scale as $r^{-(l+1)}$ only a small error results if we truncate the expansion to only a few terms (monopole or quadrupole term) when we compute the gravitational field of the distribution far away from its position $\vec{r}$.

The way to proceed then is to group the particles of the N-body realization in such a way that we can use the above approximation. This is done by arranging our particles in a "tree" structure.

5.4.1 The Tree Structure

Even though "trees" were fairly recently introduced in computational astrophysics, they have been used by computer scientists for years in order to manipulate data structures. The formal and rather abstract definition of a tree (Knuth 1973) is a finite set T of nodes such that :

1. There is a single node r that is the root of the set T.
2. All other nodes are divided into $m \geq 0$ disjoint sets $T_1, ...T_m$, each of which is also a tree; T_i is the i^{th}*subtree* of T.

Simply put, a tree is a hierarchical data structure which consists of pointers from a set of data to other sets of data, which in turn points to another set of data. A graphical visualization of a tree is presented in Figure 5.1.

As one can see trees are usually drawn upside down with the root of the tree (root node) at the top. Very often "family" terms are used to describe a tree structure. Every node i on a tree structure may have a "parent", many "children" and "siblings". A "parent" of a node i is the node which points to i. All nodes with the same parent are called "siblings", and all other nodes where the node i points at are its "children". The root node has no parent. The nodes with no children are often called the "leaves" of the tree.

There two different types of tree structures that are being used in tree codes today.

5.4.2 The Barnes-Hut Tree

In **Eulerian codes** (Barnes & Hut 1986), the tree is constructed **top-down** as shown in Figure 5.2 for a 2-dimensional and Figure 5.3 for a 3-dimensional distribution of particles (Barnes 1995). In the general 3D case, the Barnes-Hut method begins by building a cube which surrounds the physical space of all particles of the system and corresponds to the root node of the tree. The first particle is placed in the box and the total mass, the center of mass and higher orders of the mass distribution are calculated. Then a second particle is placed in its position in the box and the same quantities are calculated. Then the algorithm asks the question. Is there more than one particle in the box ? Since the answer to this question is yes the box is subdivided into eight boxes of equal volume by bisecting its sides. Suppose that the two particles of the first box are now in the corresponding sub-boxes. Then the same quantities, (i.e. center of mass etc.) are calculated for each sub-box. The sub-boxes are the

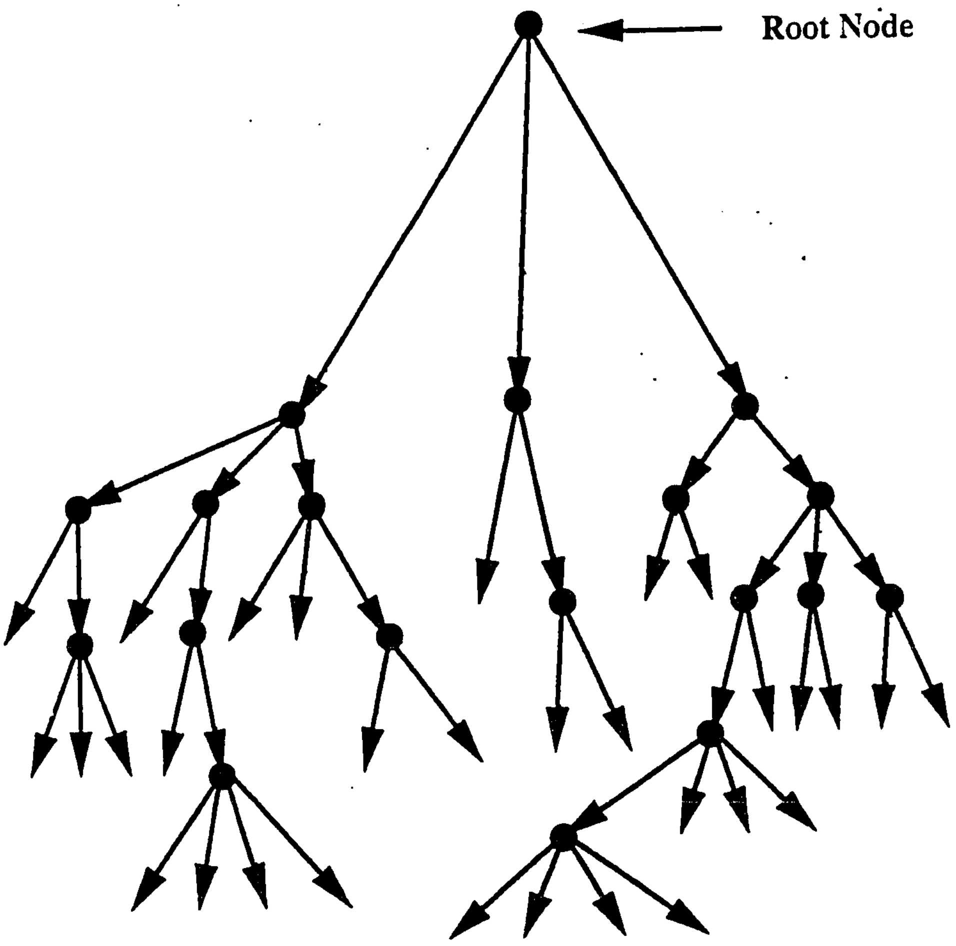

Figure 5.1: A typical tree data structure. the nodes of the tree are shown as filled circles. The links between child and parent nodes are shown as arrows. (Graph from K.Olson's lectures on trees. NASA/GSFC Summer School in High Performance Computational Physics.)

intermediate nodes of the tree structure. This process continues by cycling through the list of particles of our N-Body realization by subdividing boxes whenever a box has more than one particle. Each time a box is subdivided we create links between that (parent) and its sub-boxes (children).

As one can see from Figure 5.3 this algorithm creates an *oct tree*, a tree where every parent has eight children. Also this type of tree is **unbalanced**. This means that regions of high spatial density require many subdivisions into boxes in order for each sub-box to contain only one particle. Such a method of tree creation can be programmed efficiently for vector machines but is not appropriate in the case of parallel architectures such as the one we were using.

After the creation of the Barnes-Hut tree, the gravitational acceleration/force at each particle can be calculated. For each particle i of the distribution, the tree is searched starting at the root node and descending through the nodes. The **criterion** on whether the calculated values of the mass distribution of a specific node can be used to approximate its contribution to the gravitational field at the position of particle i, is set by examining the quantity :

$$\theta = b/r$$

where b is the length of the size of the sub-box which defines the current node and r is the distance between the particle i and the center of mass of the node.

If θ is less than a fixed tolerance (usually 0.6-0.8) the node is accepted and the potential and the force are calculated from the data stored in the current node of the tree. Then a sibling node is examined or if there are no siblings, we proceed with a sibling of the parent node.

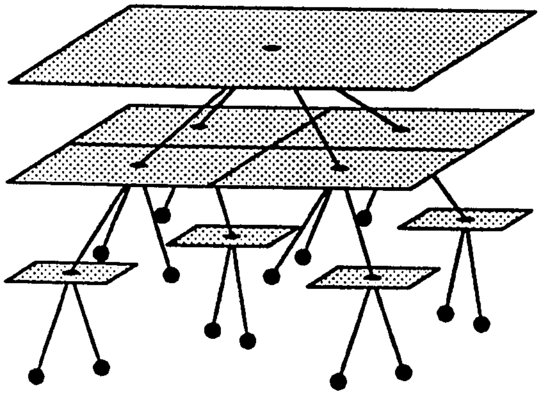

Figure 5.2: A Barnes-Hut tree generated from a 2 dimensional system. Filled circles are bodies and shaded squares are cells (Barnes 1995)

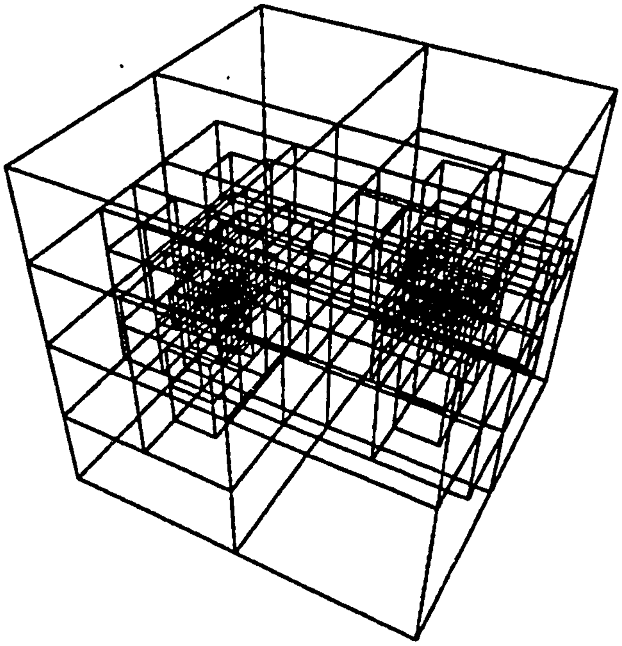

Figure 5.3: Hierarchical box structure created from a particle distribution with two density pairs (Barnes 1995)

If the node is not accepted, then the particle accesses the links stored on the current node and proceeds examining the validity of the criterion on the children of the current node.

A schematic representation of this process is shown in Figure 5.4. In Figure 5.5 we see an example of the same algorithm for the simple case of a homogeneous distribution of N particles in a sphere.

It can be shown (Hernquist 1988) using this algorithm that the number of operations to compute the force on all N bodies of our distribution scale as $O(NlogN)$.

5.4.3 The Binary Tree

In **Lagrangian codes** (Appel 1985; Jernigan & Porter 1989), the tree is constructed **bottom-up** by pairing particles which are near neighbors in 3D space to construct a node. This process continues until a root node is reached. Our code closely follows this approach which can be expressed in the following manner :

1. Find mutual nearest neighbors for all particles, and create a node for each a pair of neighbors.

2. Compute the total mass and center of mass of the pair and store them as node data. Also store the links between the children and the parent node as well as the *size* of the node which is defined as the maximum of the distances between the children and the parent node plus the sizes of the children.

3. Remove the particles or nodes just paired from further consideration.

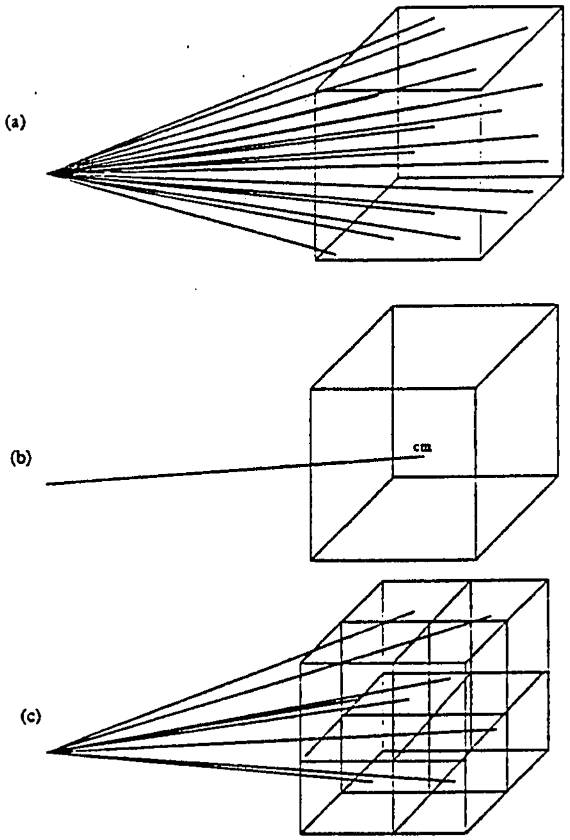

Figure 5.4: Schematic representation of the recursive structure of the Barnes-Hut treecode, in the calculation of the gravitational field due to the distribution of mass particles inside a box. (a) The exact force on a body outside the box is the result of the direct summation over all particles in the box. (b) If the **criterion** for the multipole approximation is valid, the summation can be replaced by a single interaction. (c) Otherwise the cell is subdivided into eight children and the procedure i.e. steps (b) and (c) is recursively applied to the children (Fullagar *et al.* 1992).

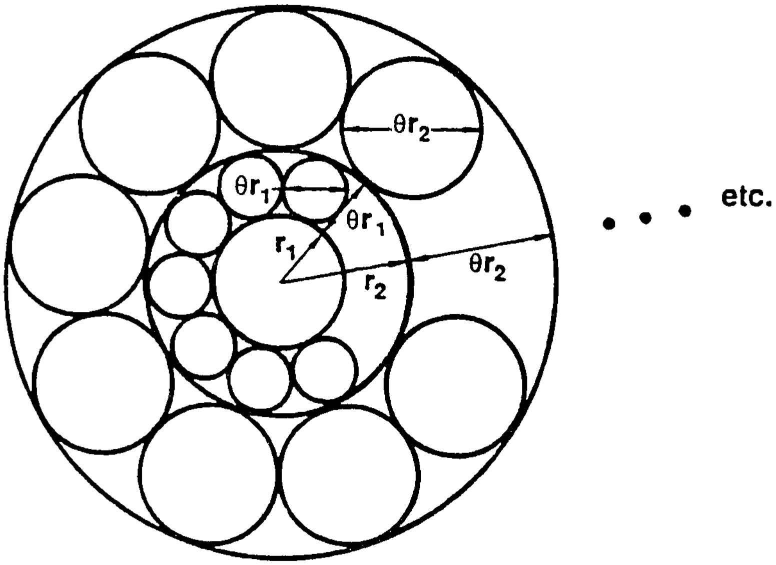

Figure 5.5: Schematic representation of the force computation on a particle at the center of a homogeneous sphere of particles, using the Barnes-Hut hierarchical tree method. The influence of subregions of linear dimensions θr_n, each containing many particles, is calculated using multipole expansions (Hernquist 1988)

4. Go back to (1) and find the nearest neighbors among the newly created nodes and the left over particles[1].

A graphical representation of the resulting binary tree is shown in Figure 5.6.

After the binary tree is created, one can search the tree in a fashion similar to the Barnes-Hut tree. A graph of this search for a gravitational system of 20 particles is presented in Figure 5.7

Another way to compute the accuracy criterion is to compare the acceleration produced by the current node on a particle i to the one produced by the two children of the node. One can see that the worst case scenario in not resolving the node and using its children is when the two children are lined up on the line connecting the particle i to the current node. In this case the difference between the acceleration produced by the average center of mass of the node and the one created by the two children of that node is

$$\Delta\alpha_{max} = \frac{GM}{r^2} - \frac{G(M/2)}{(r+S)^2} - \frac{G(M/2)}{(r-S)^2}$$

where M is the mass of the node and S its size as was defined earlier. This can be rewritten as :

$$\Delta\alpha_{max} = \frac{GM}{r^2}\left\{\frac{1+(S/r)^2}{\left[1-(S/2)^2\right]^2} - 1\right\}$$

This approach was originally introduced by Jernigan & Porter (1989) and has an advantage over the θ Barnes-Hut criterion. When we use the θ criterion, we can

---

[1] Note that in this algorithm we demand that the particles are nearest neighbors and as a result some particles may not be paired with each other at every loop

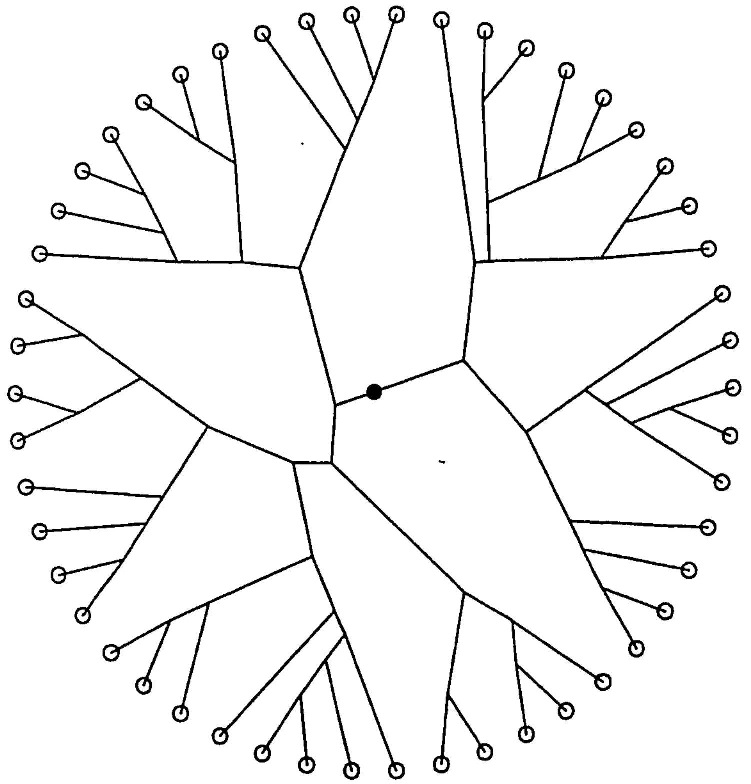

Figure 5.6: Binary tree of an N-body system rearranged to show the hierarchy. The root of the tree is at the center, indicated by the solid circle and the particles are the open circles at the edge

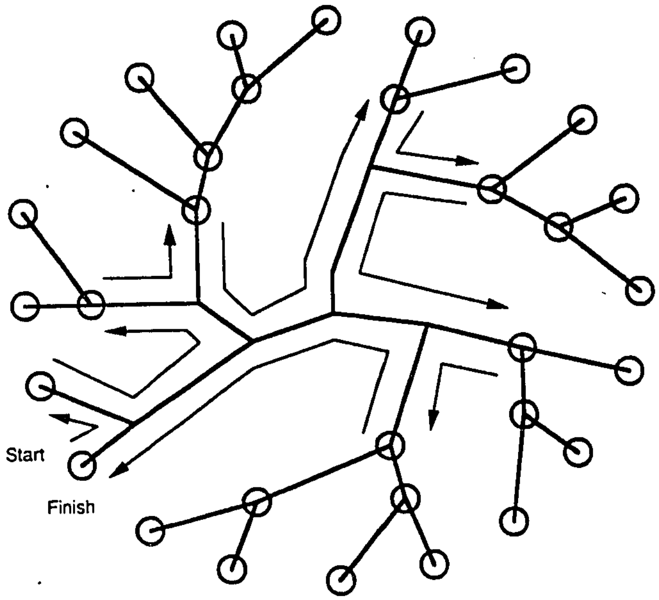

Figure 5.7: Partial search of the binary tree starting from a particle. Circles at the edge indicate the particles and nodes which would generate sufficiently accurate force terms for the particle from which the search starts. The tree scan never examines details under any circled nodes

only control the average error of our approximation of the gravitational field due to the use of the multipole expansion instead of the direct sum. The Jernigan & Porter (1989) criterion lets us calculate a physically meaningful quantity (i.e. acceleration) and it has been proven that using it one can set an absolute upper boundary on the acceptable error on our approximation of the gravitational field.

An extra complication introduced in the binary tree is the need to find the near neighbors of all particles using an extra algorithm. There are several ways that this can be done. The one that we used was given by Benz *et al.* (1990) and proceeds as follows :

1. Sort the particles into 3 sorted lists, on x, y and z. this way if one particle is physically close to another, it will be close in all three lists. This way one has built a "brick shaped" region around each particle.
2. Find the nearest "wall" of this brick for each particle. Compute and store the distance to the particle represented by this wall.
3. If the distance to this particle is less than the nearest wall, the nearest particle has been found.
4. Continue expanding walls until the nearest one is found.

However, binary trees are **balanced trees** which proves to be a major advantage when one tries to port the algorithm in a parallel computational environment.

5.5 The Computational Method

The code we developed is a hierarchical code based on structure of the binary tree described in the previous section. It was built in a fashion that would make it easily portable in parallel architectures and was originally introduced by Olson & Dorband (1994). We expanded and improved the original version with the guidance of one of the authors (Olson priv. com.) and we provide the source at the Appendix of this dissertation.

Our code was optimized for use on the MasPar 1 and MasPar 2, the SIMD supercomputers at the Scalable Computing Lab, of Ames Laboratory. SIMD (Single Instruction Multiple Data) computers are composed of many ($\sim$ 10,000) small (10 KBytes) processors. Every processor executes the same instruction at the same time but on different data. This results in highly synchronized communications but inability to keep long interaction lists in each processor due to lack of memory. Hence the data must be distributed and fetching date over the communication network must be done frequently. The advantages of SIMD computers are that they are easier to program than other parallel machines and they are also cheaper.

The main characteristics of our code are described in following sections.

5.5.1 Building our Tree Structure

The tree that we developed had the basic structure of the binary tree (Jernigan & Porter 1989). However, instead of grouping pairs of nearest neighbors in order to create the first parent nodes, we used groups of eight nearest neighbors. This was done since our testing showed that it maximized the performance of the code.

As we mentioned in the previous section, in a binary-like tree one needs to introduce an algorithm which will provide us with the nearest neighbors of all particles of our distribution. We used the method of orthogonal bisection described in the previous section. The list of particles is sorted on one of the coordinate directions (the one which spans to the largest spatial range). The sorting is done using the primitive scan functions discussed in Bleloch (1991). This list is then split into two halves. Each of the sublists is sorted again on the coordinate direction which spans the largest within the sublist. The particles in each of the sublists become the nodes in the next level of the tree. This process continues until the number of particles in a sublist is 1. Once this is done the node quantities (total mass, center of mass, size and quadrupole moments) can be computed and stored in the node. More details on that can be found in the comments of the subroutine "make_tree" in the Appendix.

5.5.2 Tree Search

In our tree we take the approach that all particles begin their search of the tree at the leaves (see Figure 5.7). Since the parallel computer that we were using (MasPar 1) had 16,384 processors, each processor was keeping position and velocity information on only a few (usually 2 to 8) particles. As a result, if two processors would request the same data from another processor, the computer would resolve the request but could only do one at a time. Therefore if all N particles started at the root of the tree, the processor which contained the root data would have to resolve N conflicts and this would take $O(N)$ of the CPU cycles.

The accuracy criterion that we used was the one of Jernigan & Porter (1989). When searching the tree, the quantity $\Delta\alpha_{max}$ was compared with a calculated average acceleration of the system. Once the criterion was satisfied, the potential and acceleration at each particle was calculated and the system was advanced forward in time.

5.5.3 Time Integrator

Our code uses a time-centered leap-frog algorithm (Hockney & Eastwood 1988; Hernquist & Katz 1989), a fairly fast second-order integrator. In the leap-frog integrator the velocities are offset with respect to the positions by half a timestep. The integrator starts by calculating the accelerations ($\vec{a}$) from the initial positions ($\vec{r}$) and then by advancing the system by half a timestep using the formula

$$\vec{r}_{\frac{1}{2}} = \vec{r} + \frac{1}{2}\vec{v}_o \Delta t + \frac{1}{8}\vec{a}_o \Delta t^2$$

where Δt is the value of the timestep. Then the velocities are advanced one timestep

$$\vec{v}_1 = \vec{v}_o + \Delta t \vec{a}_{\frac{1}{2}}$$

As one can notice, the velocities are offset by half a timestep with respect to the positions. From this point, the positions at timestep n+$\frac{1}{2}$ are updated using the velocities at timestep n, and the velocities at timestep n are updated by calculating the forces at timestep n-$\frac{1}{2}$. This algorithm can be written as

$$\vec{r}_{n+\frac{1}{2}} = \vec{r}_{n-\frac{1}{2}} + \Delta t \vec{v}_n$$
$$\vec{v}_{n+1} = \vec{v}_n + \Delta t \vec{a}_{n+\frac{1}{2}}$$

For diagnostic purposes, the positions and velocities can be synchronized at the timestep n+1 with the correction

$$\vec{r}_n = \vec{r}_{n+\frac{1}{2}} + \frac{1}{2}\vec{v}_{n+1}\Delta t - \frac{1}{8}\vec{a}_{n+\frac{1}{2}}\Delta t^2$$

5.5.4 Optimizations

Our computational method was optimized to the specific parallel computers (MasPar) in order to increase the speed of the calculations. As we mentioned earlier the main problem one encounters when programming in parallel architectures is the communication time — the time it takes to transfer data from one processor to the other. This problem is even more serious in the MasPar since each processor has a small local memory. To address this problem we worked on two techniques.

5.5.4.1 Multiple Copies We developed an algorithm which enabled us to keep multiple copies of the information of the root node as well as several hundred of the upper level parent nodes on many processors. This way it was not always necessary to invoke inter-processor communication in order to fetch the data to the processor which had to perform a calculation with the values of the node. Since the algorithm is machine specific and rather complex, I will not elaborate more on it, but refer the reader to the Appendix and the comments in the source code. The use of multiple copies improved the performance of the code by a factor of 15.

5.5.4.2 Speeding up Fetching We also worked in speeding up the actual time in moving data from one processor to the other. To transfer a real number between two processors, time is lost in opening and closing a communication channel.

If we compress four real numbers into a double precision complex number we can transport the same information by one opening and closing the connection only once . This process is done by the subroutines "cast1" and cast2" and led to an improvement of a factor of 3 in the performance of the code.

5.6 Conclusions

The parallel version of the treecode developed was initially tested in simulations of dynamical relaxation of an isothermal sphere. The timing analysis of a single timestep is presented in Table 5.1

Table 5.1: Timing Analysis of the Treecode for MasPar 1

	Monopole	Quadrupole
Particles	32768	32768
Accuracy	$\leq 1\%$	$\leq 1\%$
Total # of nodes	37449	37449
Average # of neighbors	429	429
Time to make tree	5.5 sec	5.5 sec
Time to fetch values	4.1 sec	9.8 sec
Time to calculate the force	8.6 sec	20.3 sec
RMS error	6.30×10^{-3}	3.01×10^{-3}
Average error	4.97×10^{-3}	2.34×10^{-3}
Maximum error	1.36×10^{-1}	5.73×10^{-2}

One can easily see that using this the treecode and for the given accuracy parameter the force on a typical particle is calculated by simply summing 426 terms instead of 32767. Even though the maximum error in the calculation of the force on a few particles may reach 10 %, both the rms and average error of the distribution of N particles is of the order of 10^{-3}. Simulations where the particle distribution was evolved for 2000 timesteps showed that the total the energy, and angular momentum of the system were conserved within 0.1%. Further simulations of construction and time evolution of disk galaxies were performed and both energy and angular momentum were conserved in the same levels.

At the present stage the code is fully functional. It is being used in simulations off-center collisions between disk galaxies with rising rotation curves and spherical companions in near parabolic orbits.

CHAPTER 6. CONCLUSIONS

6.1 General Discussion

The title of the present dissertation is “A study of galaxy interactions”. As such, a major part of this thesis was the presentation and interpretation of multi-wavelength observations of two interacting systems, the VII Zw 466 group and Arp 10. We also presented the numerical method that we developed for simulating the dynamics of the stellar component. This method can be used as a tool which will enable us to explore further the dynamical implications of the observational data. Such a merging of theoretical modeling and observations is essential in order to avoid over-interpretation of either observations or models and to further our understanding of interacting systems.

The reason why we selected Arp 10 as the prime candidate to study and its importance in the general picture of galaxy interactions will be discussed in detail in the next section. However, reading the chapters two and three, it should be evident that Nature has many surprises in store for us. As a result one needs to collect all data possible and be conservative when one draws the final conclusions.

The VII Zw 466 group was selected in order to take the reader a step further and present a more global picture of the dynamics of a group of galaxies. We did not get into many details of the ring system itself, as we did with Arp 10, partly because some of this work has already been done by other researchers (Theys & Spiegel 1976; Thomson & Theys 1978; Appleton & Marston 1995; Marston & Appleton 1995).

6.2 The VII Zw 466 Group

In chapter four we presented a dynamical study of the classical ring galaxy VII Zw 466 and its group. This system is in the early stages of its evolution with the first star forming ring propagating through the disk. We calculated the velocity distribution of the H I gas in the ring and estimated its rotational and expansion velocity. We also described the distribution of the H I gas of the group members, identified two new group members, and presented a plausible scenario for the collision. Finally using dynamical arguments we estimated the amount of dark matter of the group.

6.3 What did we Learn from Arp 10 ?

After reading this thesis one can easily ask the question : "Why did we study Arp 10 after all?". Arp 10 is just one galaxy, from a sample of ring galaxies, which represent a small fraction of the interacting systems, which themselves are a small fraction of the total number of observed galaxies. Most galaxies seen in the sky are either spirals or ellipticals.

The answer to this question lies in the actual peculiarities of this system and its uniqueness. As it was mentioned in the first chapter, one of the major problems of extragalactic astronomy is the understanding of the evolution of galaxies. As it is often the case for other dynamical systems in nature that evolve with time, galaxy evolution is a violent process. The transition from one stage of dynamical equilibrium to another takes only a short time ($\approx 10^8$ years) compared with the Hubble time ($\approx 10^{10}$ years). In order to study galaxy evolution, one needs to be able to quantify the physical processes that control this transitional period. However, this period is only 6 orders of magnitude longer than the history of extragalactic astronomy itself. As a result one expects that only a small fraction of galaxies will be undergoing these changes at the current epoch. Of those galaxies, only few will have simple dynamical properties, appropriate orientation and be close enough to perform detailed observations so that we can develop our models.

This brings us back to the importance of the ring galaxies, which, as it was mentioned in the introduction, fullfil these "ideal conditions" for dynamical study. Arp 10 was originally classified as ring galaxy. As such, it was an ideal object for research : a galaxy with a large well defined hydrogen disk which was disturbed by a companion passing through the disk. This led to the formation of the density wave in the disk and resulted in collisionally induced star formation in a ring. One could try (as we did in the second chapter) to study the dynamics of the system and calculate the star formation properties of the rings. Then, one could examine their implications in more general problems of astronomy such as the behavior of the gas in the case of triggered star formation and their effects on the metallicity and enrichment of interstellar medium in galaxies due to the enhanced formation of a young stellar population.

Unfortunately, our detailed analysis of Arp 10 (see chapter 3) revealed, to our surprise, that it was not a simple classical colliding ring. First, the galaxy originally thought to be the intruder that caused the formation of the ring proved to be a background galaxy. Second, the neutral hydrogen disk was very extended and severely disturbed. The dynamics of the gaseous disk did not follow the behavior of the stellar component determined by the optical imaging and spectrophotometry. Third, deep CCD B-band imaging revealed the presence of "ripples", similar to the ones observed in "Shell" galaxies by Carter *et al.* (1982) and Schweizer and Seitzer (1988). This was very peculiar given that typical shells are observed around elliptical and S0 galaxies which by nature are gas poor systems. The current view on galaxies with shells is that they form as a result of a merger between an elliptical and a disk galaxy (Prieur 1990). Numerical simulations of the stellar component have shown that the shells are created either by "phase-wrapping" of debris on nearly radial orbits (Quinn 1984), or by "spatial-wrapping" of matter in thin disks (Dupraz and Combes 1987, Hernquist and Quinn 1989; Quillen et al. 1993). These numerical models have shown that shells can be easily created during interactions.

Recently, though, there have been observational evidence of two shell galaxies (Cen A and NGC 2865) by Schiminovich et. al (1994 ; 1995) that do not fit the standard picture. Instead they present H I gas which is unambiguously associated with the optical shells, and is located to the *outside* of the stellar shells.

Arp 10 on the other hand, is a galaxy which has most of the characteristics of a ring galaxy, that is, a gaseous disk and star forming rings as well as several faint "ripples" in its outer structure. As such, it may be a transitional early stage of an intermediate type of merger, formed in a slightly off-center collision between a gas poor galaxy and a gaseous disk system.

One can now envision a picture of several types of galaxies that can be members of an colliding pair. In a rather simplified description one can consider the following three cases :

1. *Gas Poor - Gas Poor:* The "Shell Ellipticals" are such a case. A small gas poor disk galaxy merges with a big elliptical in a radial orbit. The stars of the companion form density waves with sharp edges at a location near the apocenter of their orbits. No or small quantities of H I gas is associated with the interacting galaxies.

2. *Gas Rich - Gas Rich:* This is the case of the classical "Collisional Ring" galaxies, like VII Zw 466. A small companion passes through the center of a gaseous disk. This perturbs the potential of the galaxy driving low amplitude density waves through the disk. Star formation is induced in the areas of overdensity, resulting in a bright star forming ring propagating towards the edge of the disk.

3. *Gas Rich - Gas Poor:* This may well be the case of Cen A, NGC 2865, or Arp 10. For Arp 10, a gaseous disk may be disturbed by a gas poor companion. The density wave on the disk results in collisionally induced star formation and the stellar population of the companion leads to the formation of the ripples.

The first two cases have been studied extensively, both observationally and numerically through the years (see chapter 5 and references therein). The last case, in which Arp 10 probably belongs, has not been explored, since there were few (if any) candidates that could be used in order to get some observational feedback for the modeling. However, they may be very interesting for several reasons :

- As the simple dynamical exercise this type of interaction is very challenging. It presents the study of the dynamics of a system of point masses when it interacts with a gaseous component and leads to the formation of stars, hence to a depletion of the gaseous material. The physical properties of gas and stellar dynamics involved are strongly coupled and have to be treated in a self-consistent manner. Heating of the gas by the young stellar population and supernovae explosions add an extra complication to the study of this problem.

- Observationally, it may also be possible to probe the dynamics of the individual members of the pair, because the two interacting galaxies would have two distinctly different stellar populations. The gas poor galaxy would probably have an evolved old stellar population, contrary to the star forming young gaseous disk.
- Since most galaxies are formed in groups with more than two members one would expect that over a Hubble time, several of the galaxies would interact, leading to an increase in the star formation efficiency of the interacting members. We should then expect, that when the first mergers occur, the galaxy types of the group members would become less homogeneous. If more interactions occur between the group members, then the probability of a collision between a gas-poor and gas-rich system would be higher than before. This implies that one may observe more "Arp 10 like" collisions. This type of interaction would probably be observed in fairly young groups and clusters of galaxies that have not yet become virialized.

6.4 The Status of the Modeling

A major part of this dissertation was the development of the numerical code which would enable us to model specific galaxy interactions. This process took a much longer time than expected for two basic reasons:

- The construction of numerical models of galaxies with more than one component (i.e. galaxies with bulges, disks and halos) has proven to be a non-trivial task. In order to create a multicomponent galaxy which can be used later in interactions, one needs to create a system with the desired profile in phase-space (that is, specific mass-density profile, velocity dispersion and rotation curve) in **near equilibrium**. This is critical since one has to be confident of the initial conditions and characteristic before the interaction. The process was computationally expensive since it required the dynamical relaxation of the components of the isolated galaxies. Only recently a method that would speed up this procedure was developed (Hernquist 1993).
- In our initial simulation efforts, we were using a serial treecode and the campus computing facilities. This set a limitation to the number of particles that we could use in our models (N<10,000). This small number of particles introduced "statistical noise" in our models, which proved to be a serious complication when we tried to create multicomponent systems.

Those problems and the availability of the parallel computers of the Scalable Computing Lab led us to redirect our efforts in developing a more efficient parallel treecode. The collaboration with Dr. K. Olson (NASA/GSFC) played a crucial role in this effort, since he introduced us to the concepts of parallel programming and guided us through the whole code development. The code is finally ready for production runs and we expect that within the next few months we will be able to get scientifically significant results.

6.5 Future Plans

In the future I would like to continue the study of the Arp 10 system with more observations and modeling, in order to resolve in the best way possible the dynamics of this type of galaxy interaction.

I am already working on analyzing further the data from our longslit spectrophotometry of the system. So far, we have only used the spectra to get estimates on the dynamics of the stellar component at different regions of the galaxy. However, using the ratios of different emission lines, one can also estimate the metalicities as well as the stellar populations of those regions. We could also compare those results with the ones of the other classical ring galaxies of our sample.

We have submitted a proposal to use the Hubble Space Telescope to perform high resolution B–band, I–band and Hβ imaging of the galaxy. The high resolution capability of the HST is essential in order to probe the structure of the nuclear region, map the luminosity distribution of the possible companion, resolve in detail the star forming regions along the rings and reveal the fine filaments and bubbles that surround them. The detailed imaging will enable us to positively check the presence of the star formation threshold and examine how it can be explained in the context of the collisional origin of the system.

I would also like to pursue further the code development by including a treatment of the gaseous component. The modeling of the gas dynamics is essential if one wants to treat a galaxy in a self consistent manner and to deal with problems which involve gas rich systems. This has been done successfully by other researchers (Barnes & Hernquist 1992, Gerber 1993). We could combine the treecode with the SPH method (Monaghan 1985) used in the modeling of collisional ring galaxies by C. Struck (Struck

1995; Appleton & Struck 1995).

BIBLIOGRAPHY

Aarseth, S.J., 1972, In *Gravitational N-Body Problem* IAU Colloquium No. 10, ed. M. Lecar, (Dordrecht: Reidel), p. 373

Aarseth, S.J., 1985, In *Multiple Time Scales*,ed. J.U.Brackbill and B.I. Cohen, (Orlando: Academic Press), p. 377

Allen, D.A., Roche, P.F. & Norris, R.P. 1985, MNRAS, **213**, 67

Appel, A.W., 1985, SIAM J. Sci. Stat. Comput. **6**, 85

Appleton, P. N. & Marston, A. P. 1995, AJ (submitted)

Appleton, P. N. & Struck, C. 1995, In *Fundamentals in Cosmic Physics* (Amsterdam: Overseas Publishers Association), (in press)

Barnes, J., 1992, ApJ, **393**, 484

Barnes, J., 1995, In *Computational Astrophysics, Volume I* ed., J. Barnes, W. Benz, E. Muller, & M. Norman (Berlin: Springer-Verlag), (in press)

Barnes, J. & Hut, P., 1986, Nature, **324**, 446.

Benz, W. *et al.* 1990, ApJ, **348**, 647

Binney, J. & Tremaine, S., 1987, *Galactic Dynamics* (Princeton: Princeton University Press)

Bleloch, G. E., 1990, *Vector Models for Data-Parallel Computing*, Cambridge, (London: MIT Press)

Butcher, H.R. & Oemler, A.,Jr., 1978, ApJ, **219**, 18

Butcher, H.R. & Oemler, A.,Jr., 1984, ApJ, **285**, 426

Carter *et al.*, 1982, Nature **295**, 126.

Combes, F., 1994, In *The Formation and Evolution of Galaxies*, ed. C. Munõz-Tuñón & F. Sánchez (Cambridge: Cambridge University Press), p. 317

Dupraz, C. & Combes, F. 1987, A&A, **185**, L1

Elmegreen, B., 1992, In *Star Formation in Stellar Systems*, eds G. Tenorio-Tagle, M. Prieto & F. Sánchez (Cambridge: Cambridge University Press), p. 381

Fullagar, D *et al.*, 1992, Proceedings of the 5^{th} Australian Supercomputing Conference.

Gerber, R.A., 1993, Ph.D. thesis, Univ. of Illinois, Urbana-Champaign

Gerber, R.A., Lamb, S.A. & Balsara, D.S., 1992, ApJ, **399**, L51

Gerin, M., Combes, F. & Athanassoula, E., 1990, A&A, **230**, 37

Jernigan, J. G. & Porter, D. H. 1989, ApJ Suppl., **71**, 871

Horellou, C. & Combes, F. 1993, In *N-Body Problems and Gravitational Dynamics*, ed. F.Combes and E. Athanassoula (Paris: Observatoire de Paris) p. 168

Hernquist, L., 1987, ApJ. Suppl., **64**, 715

Hernquist, L., 1988, Comp. Phys. Communications, **48**, 107

Hernquist, L., 1993, ApJ, **86**, 389

Hernquist, L. & Katz, N., 1989, ApJ Suppl., **70**, 419

Hernquist, L. & Quinn, P.J 1989, ApJ, **342**, 1

Hockney, R.W. & Eastwood J.W., 1988, *Computer Simulations Using Particles*, (London: IOP Bublishing)

Hubble, E., 1925, *Observatory*, **48**, 139

Hubble, E., 1926, ApJ, **63**, 236

Hubble, E., 1929, ApJ, **69**, 103

Hubble, E., 1936, *The Realm of the Nebulae*, (New Haven: Yale University Press)

Knuth, D. 1973, *Fundamental Algorithms*, (Reading: Addison-Wesley)

Larson, B.M & Tinsley, R.B., 1978, ApJ, **219**, 46

Lavery, R.J. & Henry J.P., 1988, ApJ, **330**, 596

Lynden-Bell, D. & Kalnajs, A.J., 1972, MNRAS, **157**, 1

Lynds, R. & Toomre, A. 1976, ApJ, **209**, 382

Marston, A.P., & Appleton, P.N, 1995, AJ, **109**, 1002

Mihalas, D. & Binney, J., 1981, *Galactic Astronomy*, (San Francisco: W.H. Freeman and Co.)

Mihos, J.C., Richstone, D.O., & Bothun, G.D. 1992, ApJ, **400**, 153

Mihos, J.C. & Hernquist, L., 1994, ApJ, **427**, 1

Monaghan, J.J., 1985, Comp. Phys. Rep., **3**, 71

Monaghan, J.J. & Lattanzio, J.C. 1985, A&A, **149**, 135

Olson, K. & Dorband, J. , 1994, ApJ Suppl. **94**, 117

Pfenniger D. & Norman, C.A., 1990, AJ, **363**, 391

Prieur, J.L. 1990, In *Dynamics and Interactions of Galaxies*, ed. R. Wielen, (Berlin: Springer-Verlag) p. 72

Quillen, A.C. *et al.* 1993, ApJ, **412**, 550

Quinn, P.J. 1984, ApJ **279**, 596

Salmon, J.K. 1991, Ph.D. Thesis, California Inst. of Technology

Salmon, J.K. & Warren, M.S., 1994, Jour. Comp. Phys., **111**, 136

Sandage, A., 1961, *Hubble Atlas of Galaxies*, Carnegie Institution of Washington.

Sanders, D.B. *et al.* 1988, ApJ, **324**, L55

Schweizer, F. & Seitzer, P. 1988, ApJ, **328**, 88

Schiminovich, D., van Gorkom, J., van der Hulst, J. M. & Kasow, S. 1994, ApJ, **432**, L101

Schiminovich, D., van Gorkom, J., van der Hulst, J. M. & Malin, D. F. 1995, ApJ, **444**, L77

Sellwood, J.A., 1987, ARA&A, **26**, 151

Soifer, B.T., Houck, J.R. & Neugebauer, G., 1987, ARA&A **25**, 187

Struck, C., 1995, In *Minnesota Lectures on Extragalactic HI* ed. E. Skillman (ASP, San Francisco) (in press)

Toomre, A. , 1977, In *The Evolution of Galaxies and Stellar Populations*, ed. B. Tinsley & R. Larson (Yale University Observatory: New Haven), p. 401

Toomre, A., 1978, In *The Large-Scale Structure of the Universe*, IAU Symp. No. 79. ed. M.S. Longair and J. Einasto (D. Reidel Publications: Holland), p. 109

Toomre, A. & Toomre, J., 1972, ApJ, **178**, 623

Weil, M. & Hernquist, L., 1993, MNRAS, **214**, 87

White, S. 1983, In *The Origin and Evolution of Galaxies*, ed. B. Jones & J. Jones (Dordrecht: D. Reidel), p. 227.

APPENDIX A PARALLEL TREECODE

The appendix contains the source of the treecode which was developed in order to perform simulations of galaxy interactions using the SIMD parralel architectures MasPar 1 and MasPar 2 of the Scalable Computing Laboratory[1]. The code is written in Fortran 90 and contains extended inline comments. It was developed under the close guidance of Dr. K. Olson NASA/GSFC, to whom I am gratefull. He deserves the full credit for the most crusial conceptual part of the code which was the gravity subroutine. (Olson, K. & Dorband, J., 1994, A.J.Suppl. 94, 117)

All files necessary for a succesful run of the code in the 4096 processor MasPar-2 follow.

The Makefile

```
OBJS    = tree-new.o build_tree-new.o
MPF     = mpfortran -pesize=4 -Zq
OPTS    = -Omax -strip_opts=schedule -extend_source -nofecommon
LIBDIR  = /home/disk3/vassilis/lib/
LIBS = $(LIBDIR)libsort_mp2.a

tree-new: $(OBJS) $(LIBS)
$(MPF) $(OPTS) -o new $(OBJS) $(LIBS)
tree-new.o: tree-new.f
$(MPF) $(OPTS) -c tree-new.f
build_tree-new.o: build_tree-new.f
$(MPF) $(OPTS) -c build_tree-new.f
```

---

[1] Supported by the Applied Mathematical Sciences Program of the Ames Laboratory - U.S. Department of Energy under contract number W-7405-ENG-82

The "parameter" file

```
 parameter (nprocs=4096)      ! the number of processors
 parameter (n=nprocs*8)       ! the number of particles (a power of 8)
 parameter (nlayers=n/nprocs) ! the number of layers of particles
 parameter (acc_param=0.01)   ! the accuracy parameter for gravitational
                              ! calculations
 parameter (soft=0.05)        ! the gravitational softening parameter

 logical doquad               ! this is defined in the file 'quad.h'

 parameter (nsteps=1500)      ! The total number of timesteps
 parameter (nlog=5)           ! dynamics log every nlog steps
 parameter (nout=100)         ! snapshot of the system every nout step
 parameter (dt=5.0e-4)        ! The length of the timestep
 parameter (level_c=5)        ! the highest level containing extra copies,
                              ! which depends on n and # children per node
 parameter (max_nodes=2*n-1 + level_c*nprocs) ! the maximum length of the
                              ! the vectors

 integer uinbod, uoutbod, ulogbod
 character*8 parfile, inbodfile, outbodfile, logbodfile


 parameter(uinbod=10)
 parameter(inbodfile ='gal.dat')
 parameter(uoutbod=11)
 parameter(outbodfile='gal.out')
 parameter(ulogbod=12)
 parameter(logbodfile='gal.bin')
```

The "quad.h" file

```
! !!!!!!!!!!!!!!!!!!!!!!!!!!!!!!!!!!!!!!!!!!!!!!!!!!!!!!!!!!!!!!!!!!!!!!!!!!!
!
! This file simply defines the logical parameter doquad. It was necessary
! to be done this way since the parameter file was included in each
! subroutine and we were getting redefinition errors

parameter (doquad=.FALSE.)
!
! doquad = .FALSE. ==> only monopole contribution in the caculation of forces
! doquad = .TRUE.  ==> quadrupole contribution in the caculation of forces
!
! !!!!!!!!!!!!!!!!!!!!!!!!!!!!!!!!!!!!!!!!!!!!!!!!!!!!!!!!!!!!!!!!!!!!!!!!!!!
```

The Main Code : "tree-new.f"

```
! !!!!!!!!!!!!!!!!!!!!!!!!!!!!!!!!!!!!!!!!!!!!!!!!!!!!!!!!!!!!!!!!!!!!!

! treecode written 4/94 by K. Olson, USRA nad GSFC
! (301) 286-8707, olson@jeans.gsfc.nasa.gov
! A.J. Supplement 94, p117-127 (1994)

! Version #: 94_11_1 : MP-2 (4K PEs)

! !!!!!!!!!!!!!!!!!!!!!!!!!!!!!!!!!!!!!!!!!!!!!!!!!!!!!!!!!!!!!!!!!!!!!
! August 10, 1994
! !!!!!!!!!!!!!!
! 1- Modifications to the original code in order to include calculation
! of the quadrupole moments.

! 2- Use of casting to improve the communications.

! July 94/ Vassilis Charmandaris , ISU
! (515) 294-2989, vassilis@iastate.edu
!
! !!!!!!!!!!!!!!!!!!!!!!!!!!!!!!!!!!!!!!!!!!!!!!!!!!!!!!!!!!!!!!!!!!!!!
! October 24,1994
! !!!!!!!!!!!!!!
! 1- The multiple copies finaly work

! !!!!!!!!!!!!!!!!!!!!!!!!!!!!!!!!!!!!!!!!!!!!!!!!!!!!!!!!!!!!!!!!!!!!!
! November 3, 1994
! !!!!!!!!!!!!!!!
! 1- The leapfrog integrator is included and tested.

! 2- The program is restructured with use of include files.

! !!!!!!!!!!!!!!!!!!!!!!!!!!!!!!!!!!!!!!!!!!!!!!!!!!!!!!!!!!!!!!!!!!!!!

      program tree_search

      include 'parameters'

      include 'quad.h'          ! this file defines the doquad option

! THE PARTICLE DATA, xp, yp and zp are the particle postions.
! ax, ay, and az are the gravitational accelerations for each particle

      real * 4 xp(n),yp(n),zp(n)
      real * 4 velx(n), vely(n), velz(n)
      real * 4 massp(n)
      real * 4 ax(n),ay(n),az(n)
```

```
      real * 4 phi(n)


! the following variables are used for the energy and momentum calculations


      real * 4 vel2(n)
      real * 4 ek(n), ep(n), et(n)
      real * 4 ektot, eptot, ettot

      real * 4 cmx, cmy, cmz, cmvelx, cmvely, cmvelz

      real * 4 amx(n), amy(n), amz(n)
      real * 4 amxtot, amytot, amztot, amtot


c the subroutine gravity will caculate only the potential on
c each particle if the logical phi_only is set to .TRUE.

      logical phi_only

c The quadrupole moments will be included in the calculation of the
c series expantion of the potential if 'doquad' is se to .TRUE.

!      logical doquad


c *********** CALCULATE THE QUADRUPOLE MOMENTS *****************
c
!      doquad = .FALSE.
c
c ************************************************************

      print *,' Number of particles          :', n
      print *,' Calculate quadrupole moments :', doquad
      print *,' Accuracy parameter           :', acc_param
      print *,' Softening parameter          :', soft
      print *,' one timestep is              :', dt
      print *,' the total no. of timesteps is:', nsteps
      print *,' keep dynamics log, every     :', nlog
      print *,' checkpointer file every      :', nout



! !!!!!!!!!!!!!!!!!!!!!!!!!!!!!!!!!!!!!!!!!!!!!!!!!!!!!!!!!!!!!!!!!!!!!!!!
! Read the initial conditions ..
!
!      call init_data (n,tnow,mass,xp,yp,zp,velx,vely,velz)
```

```
!      call random_number(harvest=xp)
!      call random_number(harvest=yp)
!      call random_number(harvest=zp)

!      call random_number(harvest=velx)
!      call random_number(harvest=vely)
!      call random_number(harvest=velz)

!      velx = 100.*velx
!      vely = 100.*vely
!      velz = 100.*velz

      open(unit=uinbod, file=inbodfile, status='unknown')

      do i=1,n
         read(uinbod,*) xp(i),yp(i),zp(i)
      end do

      do i=1,n
         read(uinbod,*) velx(i),vely(i),velz(i)
      end do

      close(unit=uinbod)

      massp = 1.0

      ax = 0.
      ay = 0.
      az = 0.
      phi = 0.



      phi_only = .FALSE.        ! the initial seting is .FALSE.

! !!!!!!!!!!!!!!!!!!!!!!!!!!!!!!!!!!!!!!!!!!!!!!!!!!!!!!!!!!!!!!!!!!!!!!!!

! The main loop of iterations begins

      nloops = 0                ! this is set so that you can count
                                ! the nloops for every timestep
      ek = 0.0
      ep = 0.0
      et = 0.0
      amx = 0.0
      amy = 0.0
      amz = 0.0
```

```
! open the binary logfile

      open(unit=ulogbod, file=logbodfile, status='new', form='unformatted')

! !!!!!!!!!!!!!!!!!!!!!!!!!!!!!!!!!!!!!!!!!!!!!!!!!!!!!!!!!!!!!!!!!!!!!!!

! The dynamics of the initial state

      print *,' initial conditions ..'
      print *,' '

      ntmp = 0

      call out_state(xp,yp,zp,massp,doquad,phi_only,ntmp,
     &     velx,vely,velz,ax,ay,az,phi)

      print *,'  '
! !!!!!!!!!!!!!!!!!!!!!!!!!!!!!!!!!!!!!!!!!!!!!!!!!!!!!!!!!!!!!!!!!!!!!!!
! Do leap frog correction for the first timestep

      print *, ' do the leap frog correction'

      call gravity(xp,yp,zp,massp,doquad,phi_only,ax,ay,az,phi)

      xp = xp + 0.125*ax*dt*dt
      yp = yp + 0.125*ay*dt*dt
      zp = zp + 0.125*az*dt*dt


! !!!!!!!!!!!!!!!!!!!!!!!!!!!!!!!!!!!!!!!!!!!!!!!!!!!!!!!!!!!!!!!!!!!!!!!

! The main time iteration leapfrog loop starts ...

      do nt=1, nsteps

         print *, ' '
         print *, 'Timestep =', nt
         print *, '-----------------------------------'


!        advance the positions
         call step_pos(xp,yp,zp,velx,vely,velz) ! position at nt+1/2

!        zero the acceleration and potential arrays
         call zero_all(ax,ay,az,phi)

!        calculate the gravitational accelaration
```

```
        call gravity(xp,yp,zp,massp,doquad,phi_only,ax,ay,az,phi)
                               ! acceleration
                               ! at nt+1/2

!       advance the velocities
        call step_vel(velx,vely,velz,ax,ay,az)   ! velocity at nt+1

!       advance the positions
        call step_pos(xp,yp,zp,velx,vely,velz)  ! position at nt+1 + leap


!       get a log or output of the current state if needed.

        if (mod(nt,nlog).eq.0) then

           ntmp = nt           ! store timestep to ntmp. This is needed
                               ! in out_state to check if we'll get
                               ! a snapshot of the state of the system

           call out_state(xp,yp,zp,massp,doquad,phi_only,ntmp,
     &          velx,vely,velz,ax,ay,az,phi)

        end if

      end do

! printout the final state of the system

!      open(unit=11, file='data.out', status='unknown')
      open(unit=uoutbod, file=outbodfile, status='unknown')
      do i=1,n
         write(uoutbod,*) xp(i),yp(i),zp(i)
      end do

      do i=1,n
         write(uoutbod,*) velx(i), vely(i),velz(i)
      end do

      do i=1,n
         write(uoutbod,*) phi(i)
      end do

      close(unit=uoutbod)

! close logfile

      close (unit=ulogbod)
 2    stop
```

```
      end

! !!!!!!!!!!!!!!!!!!!!!!!!!!!!!!!!!!!!!!!!!!!!!!!!!!!!!!!!!!!!!!!!!!!!!!!!
! ************************************************************************

      subroutine gravity(xp,yp,zp,massp,doquad,phi_only,ax,ay,az,phi)

! this subroutine calculates the gravitational acceleration and potential
! for every particle of a given distribution using the tree which was
! created by the subroutine make_tree

      include 'parameters'

! THE PARTICLE DATA, xp, yp and zp are the particle postions.
! ax, ay, and az are the gravitational accelerations for each particle

      real * 4 xp(n),yp(n),zp(n)
      real * 4 massp(n)
      real * 4 ax(n),ay(n),az(n)
      real * 4 phi(n)


! THE TREE DATA, xtree, ytree, and ztree are the positions of each node
! in the tree.  mass is the mass of each node and size is the size of each
! node defined to be the distance of the farthest particle which is a member
! of that node

      real * 4 xtree(max_nodes),ytree(max_nodes),ztree(max_nodes)
      real * 4 mass(max_nodes),size(max_nodes)

! The total mass of the system is mgalaxy.

      integer * 4 mgalaxy

c The quadrupole moments will be included in the calculation of the
c series expantion of the potential if 'doquad' is set to .TRUE.

!      logical doquad

c the subroutine will caculate ONLY the potential on each particle
c if the logical phi_only is set to .TRUE.

      logical phi_only

c In order to calculate the quadrupole moments I need to define the array
c quad, which holds the quadrupole moments of each node
```

```
      real * 4 quad(max_nodes,0:5)
cmpf map quad(allbits,memory)


! The following data are used during the search of the tree

! xx, yy, and zz hold differences between particle positions and
! node positions. r is the distance between the two and is computed
! from xx, yy, and zz using the pythagorean therom i.e.
! r = sqrt( xx**2 + yy**2 + zz**2)

      real * 4 xx(nprocs),yy(nprocs),zz(nprocs),r(nprocs)

! xt, yt, zt, masst, and sizet are temporaries which hold the node data
! of the node which currently being searched.  This was done so that
! the node data need only be fetched once during each cycle.

      real * 4 xt(nprocs),yt(nprocs),zt(nprocs)
      real * 4 masst(nprocs),sizet(nprocs)
c
c I also define the temporary which holds quadrupole moments of the node
c
      real * 4 quadt(nprocs,0:5)
cmpf map quadt(allbits,memory)

c as well as six temporaries used in the calculations

      real * 4 r1inv(nprocs), r2(nprocs), r2inv(nprocs)
      real * 4 r3inv(nprocs), r5inv(nprocs), r7inv(nprocs), tempa(nprocs)

! mtot is the total amount of mass searched by any one particle.
! if mtot equals the total amount of the mass in the system, the search
! is done for that particle

      real * 4 mtot(nprocs)

! temp1, temp2, and temp3 are temporaries used during the tree search

      real * 4 temp1(nprocs),temp2(nprocs),temp3(nprocs)

! the following data items are used in the calculation of the exact forces

      real * 4 aex(n),aey(n),aez(n)
      real * 4 xxx(n),yyy(n),zzz(n),rr(n)
      real * 4 error(n), errora(n)
      real * 4 emin, emax, ave_error

      real * 4 ave_accel
```

```
      integer * 4 temp_node(n)
      integer * 4 partno(n),node(nprocs),itree(n)
      integer * 4 noint(n),n_nodes(n)

      integer * 4 node_old(nprocs)

      logical found(n),done(nprocs),success(nprocs)

! the following variables are used for CASTING

      complex * 8  a(max_nodes),b(max_nodes),p_data2(max_nodes)
      complex * 16 p_data(max_nodes),f_data(nprocs),im2(nprocs)
      complex * 8  aa(nprocs),bb(nprocs),im(nprocs)
      complex * 16 p_data1(max_nodes)
      complex * 8  f_data2(nprocs)
      integer mn

! the following variables are used for the EXTRA COPIES

      integer * 4 nlevels, last_node_6
      integer * 4 head(n,5), lnode(nprocs), ncopies(nprocs)
      integer * 4 proc_no(nprocs),level(nprocs)

cmpf map  head(allbits,memory)

! common block used to speed up the casting

      common /cast_2/ f_data,im2

! the following variables are used for timing purposes

      real * 4 timef, timep, timeq, time_all

! !!!!!!!!!!!!!!!!!!!!!!!!!!!!!!!!!!!!!!!!!!!!!!!!!!!!!!!!!!!!!!!!!!!!!!!!!!!
! The explicit use of the INTERFACE BLOCK was necessary.
! Look at page 36 of MasPar notes for explanation.
! This should move into an include file one day ...

      interface

      subroutine make_tree (xtree,ytree,ztree,size,doquad,quad,
     &     mass,partno,itree,n,nlevels,level_c,last_node_6,nprocs,n_nodes)

      real * 4 xtree(n_nodes),ytree(n_nodes),ztree(n_nodes)
      real * 4 mass(n_nodes),size(n_nodes)
      logical doquad
      real * 4 quad(n_nodes,0:5)
```

```
      integer * 4 partno(n),itree(n)
      integer * 4 n_nodes

cmpf map quad(allbits,memory)

      end
      end interface
! !!!!!!!!!!!!!!!!!!!!!!!!!!!!!!!!!!!!!!!!!!!!!!!!!!!!!!!!!!!!!!!!!!!!!!!


c computing the total no. of nodes and levels

      nmax = n
      nn = 1
      step = 2

      do while (step.gt.1)

         step = n/(8**nn)
         nmax = nmax + step
         nn = nn + 1

      end do

      nlevels = nn
      last_node_6 = n           ! the # of the last node at level 'level_c+1'

      print *,' the no. of nodes & levels    :',nmax,nlevels


! !!!!!!!!!!!!!!!!!!!!!!!!!!!!!!!!!!!!!!!!!!!!!!!!!!!!!!!!!!!!!!!!!!!!!
c calculate the heads

! head(:,j) is a variable stored for each particle and each upper level
! that has multiple copies and is the location in the un-expanded list
! of the first node at level j



      head(:,1) = nmax          ! this is the root node
      step = 8                  ! the root node has eight children

      do j = 2,level_c

         head(:,j) = head(:,j-1) - step
         step = step*8

      end do
```

```
! !!!!!!!!!!!!!!!!!!!!!!!!!!!!!!!!!!!!!!!!!!!!!!!!!!!!!!!!!!!!!!!!!!!!!!!

! initializing the arrays ..
! this is VERY important. It was a real pain to figure out why the
! program was behaving weard when I included the leapfrog.

      timef = 0.
      timeq = 0.
      timep = 0.
      time_all = 0.

      partno = 0
      forall(i=1:n) partno(i)=i

      itree = 0

      xtree = 0.
      ytree = 0.
      ztree = 0.

      xtree(1:n) = xp
      ytree(1:n) = yp
      ztree(1:n) = zp

      size = 0.0

      mass = 0.0
      mass(1:n) = massp

      quad = 0.0

! making the tree

      call make_tree (xtree,ytree,ztree,size,doquad,quad,
     &     mass,partno,itree,n,nlevels,level_c,last_node_6,nprocs,max_nodes)


      mgalaxy = n

      ave_accel=n/(0.5**2)   ! the approximate acceleration at the edge
                             ! of the system

! !!!!!!!!!!!!!!!!!!!!!!!!!!!!!!!!!!!!!!!!!!!!!!!!!!!!!!!!!!!!!!!!!!!!!!!!!!

! At this point we pack the values in order to speed up the fetching
! We pack: xtree ytree     --> a
!          ztree size      --> b
```

```
!          a b  [casting]  --> p_data


      im = (0.0,1.0)
      im2 = (0.0,1.0)
      mn = max_nodes

      size=size+1.0
      a = cmplx(xtree,ytree)
      b = cmplx(ztree,size)
      call cast1(a,b,p_data,mn)

! Pack the quadrupole coefficients if you have to :
! We pack: quad(:,0) quad(:,1) --> a
!          quad(:,2) quad(:,3) --> b
!          a b  [casting]      --> p_data1
!          quad(:,4) quad(:,5) --> p_data2

      if (doquad) then

         quad(:,3) = quad(:,3) + 1.0
         a = cmplx(quad(:,0),quad(:,1))
         b = cmplx(quad(:,2),quad(:,3))
         call cast1(a,b,p_data1,mn)

         p_data2 = cmplx(quad(:,4),quad(:,5))

      end if

c !!!!!!!!!!!!!!!!!!!!!!!!!!!!!!!!!!!!!!!!!!!!!!!!!!!!!!!!!!!!!!!!!!!
c searching the tree


      temp_node(itree) = partno(1:n)

      nloops = 0         ! This was moved outside the MAIN loop

      noint = 0
! !!!!!!!!!!!!!!!!!!!!!!!!!!!!!!!!!!!!!!!!!!!!!!!!!!!!!!!!!!!!!!!!!!!!
c the start of the loop over layers

      n2=0

! Here we are searching the trees in layer of particles.  Each layer
! contains nprocs particles.  This is more efficient on the Maspar.

!      print *, 'gravity phi_only', phi_only
```

```
      do i = 1,nlayers

         n1 = n2 + 1
         n2 = n1 + nprocs - 1

         mtot = 0.0
         level = nlevels          ! Start at the lowest level
         lnode = temp_node(n1:n2) ! The starting point in the tree
                                  ! for each particle's search. Each
                                  ! particle starts its search at its
                                  ! location in the tree.
         node = lnode

         proc_no = lnode/(((lnode-1)/nprocs)+1) ! find the CPU #

         done = .FALSE.           ! none of the particles are done
                                  ! searching yet


! !!!!!!!!!!!!!!!!!!!!!!!!!!!!!!!!!!!!!!!!!!!!!!!!!!!!!!!!!!!!!!!!!!!!!!
! the start of the loop to search the tree for this layer
! and loop while any of the particles in this layer have not finished their
! searches yet.

         do while (any(.not.done))

! first fetch the node data via the indirect address "node".

            call mpCpuTimerStart() ! Time the fetch time  : timef

            where (.not.done)

               f_data = p_data(node)
               masst = mass(node)
!               masst = n /(8.**(level-1))  this is true only if massp = 1.
            end where

            call cast2(aa,bb)

            where (.not.done)

               xt = real(aa)
               yt = real(-im*aa)
               zt = real(bb)
               sizet = real(-im*bb) - 1.0

            end where
```

```
          timef = timef+mpCpuTimerElapsed()


! Next compute the distance between the particles and the node each is
! currently searching.

!           call mpCpuTimerStart() ! Start the timer for time_all

          where (.not.done)

             xx = xp(n1:n2) - xt
             yy = yp(n1:n2) - yt
             zz = zp(n1:n2) - zt

             r = (xx**2)+(yy**2)+(zz**2)
             temp1 = sizet**2

          end where

! Next determine if this node is acceptable for the computation of a force.
! This expression is the maximum possible error in treating the node as a
! mass point and not resolving its children.  See Jernigan and Porter, ApJS,
! vol. 71, p. 871.
          success=.FALSE.

          where (r.gt.temp1.and..not.done)

             temp2 = temp1/r
             temp3 = (1.-temp2)**2
             temp3 = ((1+temp2)/temp3)-1.0
             temp3 = temp3*masst/(r*ave_accel)

          elsewhere

             temp3=1.0e10

          end where

! if temp3 is less than the user set accuracy parameter or if the current
! is a particle, then the node is accetable and success is true.

          where ((temp3.le.acc_param.or.lnode.le.n).and..not.done)
    &          success=.TRUE.

! !!!!!!!!!!!!!!!!!!!!!!!!!!!!!!!!!!!!!!!!!!!!!!!!!!!!!!!!!!!!!!!!!!!!!!
! If the node is acceptable, start computations.

! If you want to compute only the pontential do the following
```

```
          if (phi_only) then

             where (success)
                r = r+(soft**2)
                r = sqrt(r)
                r1inv = 1/r

                phi(n1:n2) = phi(n1:n2) - masst*r1inv

                mtot = mtot+masst ! mtot is the total
                                  ! amount of mass "seen" so
                                  ! far

                noint(n1:n2) = noint(n1:n2)+1 ! noint is the total number
                                                 ! nodes a particle interacts
                                                 ! with
             end where

          else

! otherwise compute the gravitational force.

             if (.not.doquad) then

! If we want the MONOPOLE contribution ONLY, we calculate this segment.

                where (success)


                   r = r+(soft**2)
                   r = sqrt(r)
                   r1inv = 1/r
                   r = masst/(r**3)

                   ax(n1:n2) = ax(n1:n2)-(xx*r)
                   ay(n1:n2) = ay(n1:n2)-(yy*r)
                   az(n1:n2) = az(n1:n2)-(zz*r)

                   phi(n1:n2) = phi(n1:n2) - masst*r1inv

                   mtot = mtot+masst ! mtot is the total
                                     ! amount of mass "seen" so
                                     ! far

                   noint(n1:n2) = noint(n1:n2)+1 ! noint is the total
                                                 ! number nodes a particle
                                                 ! interactswith
```

```
                 end where

! If we want to include the QUADRUPOLE terms ALSO then ...

              else

! Fetch the quadrupole coeficients and time it :

                 timep = timep + mpCpuTimerElapsed() ! Begin of timing  quads

                 where (success)
                    f_data = p_data1(node)
                    f_data2 = p_data2(node)
                 end where

                 call cast2(aa,bb)

                 where (success)
                    quadt(:,0) = real(aa)
                    quadt(:,1) = real(-im*aa)
                    quadt(:,2) = real(bb)
                    quadt(:,3) = real(-im*bb) - 1.0
                    quadt(:,4) = real(f_data2)
                    quadt(:,5) = real(-im*f_data2)
                 end where

                 timeq = timeq + mpCpuTimerElapsed() ! End of timing quads

! First compute the monopole term

                 where (success)

                    r = r+(soft**2)
                    r2 = r
                    r = sqrt(r)
                    r1inv = 1/r
                    r = masst/(r**3)

                    phi(n1:n2) = phi(n1:n2) - masst*r1inv

                    ax(n1:n2) = ax(n1:n2)-(xx*r)
                    ay(n1:n2) = ay(n1:n2)-(yy*r)
                    az(n1:n2) = az(n1:n2)-(zz*r)



! At this point we start the calculation of contribution of the
! quadrupole terms
```

```
! Note: The quadrupole moments where defined as:
!               quad(nimn:nmax,0) = Qxx
!               quad(nimn:nmax,1) = Qyy
!               quad(nimn:nmax,2) = Qzz
!               quad(nimn:nmax,3) = Qxy
!               quad(nimn:nmax,4) = Qxz
!               quad(nimn:nmax,5) = Qyz
!

                     r2inv = r1inv*r1inv
                     r3inv = r1inv*r2inv
                     r5inv = r2inv*r3inv
                     r7inv = r2inv*r5inv

                     tempa = 15.*r7inv*xx*yy*zz

                     ax(n1:n2) = ax(n1:n2) +
     &                    + 0.5*(
     &                    xx*3.*r5inv*(quadt(:,0)+quadt(:,1)+quadt(:,2)) +
     &                    3.*(2.*xx*r2-5.*xx*xx*xx)*r7inv*quadt(:,0)-
     &                    5.*xx*r7inv*3.*(yy*yy*quadt(:,1)+zz*zz*quadt(:,2))+
     &                    (r2-5.*xx*xx)*r7inv*3.*(yy*quadt(:,3)+zz*quadt(:,4))-
     &                    tempa*quadt(:,5))

!     &                 15.*r7inv*xx*yy*zz*quadt(:,5))



                     ay(n1:n2) = ay(n1:n2) +
     &                    + 0.5*(
     &                    yy*3.*r5inv*(quadt(:,0)+quadt(:,1)+quadt(:,2))+
     &                    3.*(2.*yy*r2-5.*yy*yy*yy)*r7inv*quadt(:,1)-
     &                    5.*yy*r7inv*3.*(xx*xx*quadt(:,0)+zz*zz*quadt(:,2))+
     &                    (r2-5.*yy*yy)*r7inv*3.*(xx*quadt(:,3)+zz*quadt(:,5))-
     &                    tempa*quadt(:,4))

!     &                  15.*r7inv*xx*yy*zz*quadt(:,4))


                     az(n1:n2) = az(n1:n2) +
     &                    + 0.5*(
     &                    zz*3.*r5inv*(quadt(:,0)+quadt(:,1)+quadt(:,2)) +
     &                    3.*(2.*zz*r2-5.*zz*zz*zz)*r7inv*quadt(:,2)-
     &                    5.*zz*r7inv*3.*(xx*xx*quadt(:,0)+yy*yy*quadt(:,1))+
     &                    (r2-5.*zz*zz)*r7inv*3.*(xx*quadt(:,4)+yy*quadt(:,5))-
     &                    tempa*quadt(:,3))

!     &                  15.*r7inv*xx*yy*zz*quadt(:,3))
```

```
                mtot = mtot+masst ! mtot is the total
                                  ! amount of mass "seen" so
                                  ! far

                noint(n1:n2) = noint(n1:n2)+1 ! noint is the total number
                                              ! nodes a particle interacts
                                              ! with
             end where

          end if           ! doquad if_then_else

       end if              ! phi_only if_then_else

! If mtot equals the total amount of mass in the system, this particle is
! done

       where (mtot.ge.mgalaxy)

          done = .TRUE.
          success = .FALSE.

       end where

! COMPUTING THE NEXT NODE TO SEARCH

! if going down  !!!!!!!!!!!!!!!!!!!!!!!!!!!!!!!!!!!!!!!!!!!!!!!!!!!!!!!!!

! if the last node was not a success, then go to the current nodes "left-most"
! child
! NOTE : we go one level down and the highest level is # 1

       where (.not.success.and..not.done)

          lnode = (8*(lnode-n-1)) + 1 ! the left child
          level = level + 1

       end where

! if going up  !!!!!!!!!!!!!!!!!!!!!!!!!!!!!!!!!!!!!!!!!!!!!!!!!!!!!!!!!!!

! If the previous node was a success then go to a sibling or to an
! ancestor (parent) node.  The following do loop accomplishes this.

       do while (any(success))
```

```
! The current node is stored for later use

               node_old = lnode

! Go to the parent of node

               where (success)
                  lnode = int((lnode-1)/8) + n + 1
                  level = level - 1
               end where

! If node_old was not the "right-most" child of lnode now, stop climbing
! and set node to the right sibling of node_old

               where (success.and.
     &              node_old/8.eq.((8*(lnode-n-1))+1)/8)

                  success = .FALSE.
                  lnode = node_old + 1
                  level = level +1

               end where

            end do

! In case of an overshoot go to the leftmost child of the root node

            where (lnode.gt.nmax)

               lnode = 8*(nmax - n - 1) + 1
               level = 2

            end where

! !!!!!!!!!!!!!!!!!!!!!!!!!!!!!!!!!!!!!!!!!!!!!!!!!!!!!!!!!!!!!!!!!!!!!
! The following 'where' block calculates which copy of the logical node
! (lnode) to fetch (set it to node)
! if the node which is to be requested is at a level that has had no extra
! copies made (level_c+1), the logical node is the node number

            where (level.le.level_c)

               ncopies = nprocs/(8**(level-1))
               node = (ncopies*(proc_no-1) / nprocs) + 1

            elsewhere

               node = lnode
```

```
          end where

          do j = 1, level_c

             where (level.eq.j)

                node = ((lnode - head(n1:n2,j)) * ncopies) +
     &                node + (nprocs*(level_c-j)) + last_node_6

             end where

          end do

! !!!!!!!!!!!!!!!!!!!!!!!!!!!!!!!!!!!!!!!!!!!!!!!!!!!!!!!!!!!!!!!!!!!!!!!!

          time_all = time_all+mpCpuTimerElapsed() ! Total time for the forces

          nloops = nloops+1

        end do                 ! End of the loop searching each layer

      end do                   ! End of the i=1,nlayers loop

! !!!!!!!!!!!!!!!!!!!!!!!!!!!!!!!!!!!!!!!!!!!!!!!!!!!!!!!!!!!!!!!!!!!!!!!!

      print *,' done with tree search '
      print *,' no. of near neighbors of 1     :',n_nodes(1)
      print *,' nloops                         =',nloops
      ave=sum(noint)/n
      print *,' ave no. of terms               :',ave

      timef=timef/1000.0
      timep=timep/1000.0
      timeq=timeq/1000.0
      time_all=time_all/1000.0

      time=mpCpuTimerElapsed()/1000.0
      print *,' time to find forces            =',timef+time_all
      print *,' time to fetch CofMs            =',timef
      print *,' time to fetch quads            =',timeq-timep
      print *,' time to do everything else     =', time_all-(timeq-timep)

c !!!!!!!!!!!!!!!!!!!!!!!!!!!!!!!!!!!!!!!!!!!!!!!!!!!!!!!!!!!!!!!!!!!!
c doing forces exactly for comparison with tree search

!      call mpCPuTimerStart()
```

```
!      aex = 0.0
!      aey = 0.0
!      aez = 0.0
!      xxx = 0.0
!      yyy = 0.0
!      zzz = 0.0
!      error = 0.
!      errora = 0.
!      ave_error = 0.
!      emin = 0.
!      emax = 0.

!      do i=1,n

!         xxx = xp-xp(i)
!         yyy = yp-yp(i)
!         zzz = zp-zp(i)

!         rr = (xxx**2)+(yyy**2)+(zzz**2)+(soft**2)
!         rr = sqrt(rr)

!!          rr = rr**3
!         rr = rr*rr*rr

!         aex = aex-(xxx/rr)
!         aey = aey-(yyy/rr)
!         aez = aez-(zzz/rr)

!      end do

!      print *,' time to compute accs. exactly =',
!     &     mpCpuTimerElapsed()/1000.0


!      error = ((ax-aex)**2)+((ay-aey)**2)+((az-aez)**2)
!      error = error/((aex**2)+(aey**2)+(aez**2))

!      errora = abs(ax-aex)+abs(ay-aey)+abs(az-aez)
!      errora = errora/(abs(aex)+abs(aey)+abs(aez))

!      ave_error = sum(error)/n
!      ave_error = sqrt(ave_error)
!      print *,' rms error = ',ave_error

!      error = sqrt(error)

!      emax=maxval(error)
!      print *,' max error = ',emax
```

```
!      emin=minval(error)
!      print *,' min error = ',emin

!      ave_error=sum(errora)/n
!      print *,' ave error = ',ave_error

      return
      end

! !!!!!!!!!!!!!!!!!!!!!!!!!!!!!!!!!!!!!!!!!!!!!!!!!!!!!!!!!!!!!!!!!!!!!!!!!
! ************************************************************************

      subroutine cast1 (a1,b1,c,n)

! This subroutine packs a1 and b1 into a double precision complex
! array c, to speed up to fetching.

      real * 8 a1(n),b1(n)
      complex * 16 c(n)

      c=dcmplx(a1,b1)

      return
      end

! !!!!!!!!!!!!!!!!!!!!!!!!!!!!!!!!!!!!!!!!!!!!!!!!!!!!!!!!!!!!!!!!!!!!!!!!
! ************************************************************************

      subroutine cast2 (a2,b2)

! This subroutine unpacks the data stored in the common block /cast_2/
! Note that the value of the parameter n is equal to the number of processors
! and needs to be changed when one runs the program to a different machine
! It is set for a 4K (64x64) MasPar

      parameter (n=4096)

!      include 'parameters' ! <- this did not work (I don't know why ..)

      real * 8 a2(n),b2(n)
      complex * 16 c(n),im2(n)

      common /cast_2/ c,im2

      a2 = dble(c)
      b2 = -dble(im2*c)
```

```
      return
      end
! !!!!!!!!!!!!!!!!!!!!!!!!!!!!!!!!!!!!!!!!!!!!!!!!!!!!!!!!!!!!!!!!!!!!!
! **********************************************************************

      subroutine out_state(xp,yp,zp,massp,doquad,phi_only,ntmp,
     &     velx,vely,velz,ax,ay,az,phi)

! This subroutine calculates the total energy and angular momentum
! of the sytem as well as the position and velocity of the center
! of mass.

      include 'parameters'


! THE PARTICLE DATA :
! xp, yp and zp are the particle postions.
! velx, vely and velz are the velocities
! mass is the mass of each particle
! ax, ay, and az are the gravitational accelerations for each particle
! phi is the gravitational potential

      real * 4 xp(n),yp(n),zp(n)
      real * 4 massp(n)
      real * 4 velx(n), vely(n), velz(n)
      real * 4 ax(n),ay(n),az(n)
      real * 4 phi(n)


! temporary variables for the accelerations

      real * 4 axt(n), ayt(n), azt(n)


c The quadrupole moments will be included in the calculation of the
c series expantion of the potential if 'doquad' is set to .TRUE.

!       logical doquad

c the subroutine gravity will caculate only the potential
c on each particle if the logical phi_only is set to .TRUE.

      logical phi_only

! THE DYNAMICAL calculations
! the following variables are used for the energy and momentum calculations

      real * 4 vel2(n)          ! velocity squared
```

```
! position and velocity of the CofM

      real * 4 cmx, cmy, cmz
      real * 4 cmvelx, cmvely, cmvelz

! kinetic (ek), potential (ep), and total (et) energy

      real * 4 ek(n), ep(n), et(n)
      real * 4 ektot, eptot, ettot

! components of the angular momentum

      real * 4 amx(n), amy(n), amz(n)
      real * 4 amxtot, amytot, amztot, amtot

! !!!!!!!!!!!!!!!!!!!!!!!!!!!!!!!!!!!!!!!!!!!!!!!!!!!!!!!!!!!!!!!!!!!!!

! Calculate the dynamics of the system

      print *, ' CALCULATE THE DYNAMICS'


! Correct the positions of particles.
! This way,velocities and positions are calculated on the same timestep.

      xp = xp - 0.125*ax*dt*dt
      yp = yp - 0.125*ay*dt*dt
      zp = zp - 0.125*az*dt*dt

! store the accelerations to correct the particles again later.

      axt = ax
      ayt = ay
      azt = az

! calculate the potential at this time step

      call zero_all(ax,ay,az,phi)


      phi_only = .TRUE.        ! set the switch ON

      call gravity(xp,yp,zp,massp,doquad,phi_only,ax,ay,az,phi)

      phi_only = .FALSE.       ! set the switch OFF, so that next time
                               ! gravity will calculate the accelerations
```

```
! compute the position and velocity of the Center of Mass of the system
! this is true for particles of equal mass.

      call mpCpuTimerStart()

      cmx = sum(xp)/n
      cmy = sum(yp)/n
      cmz = sum(zp)/n

      cmvelx = sum(velx)/n
      cmvely = sum(vely)/n
      cmvelz = sum(velz)/n

! compute the norm squared of the velocity of each particle

      forall(i=1:n)
     &     vel2(i)= velx(i)*velx(i) + vely(i)*vely(i) + velz(i)*velz(i)


! compute the energy

      forall(i=1:n)
     &     ek(i) = 0.5*massp(i)*vel2(i) ! kinetic energy of each particle

      forall(i=1:n)
     &     ep(i) = massp(i)*phi(i) ! potential energy of each particle

      et = ek + ep              ! total energy of each particle

      ektot = sum(ek)           ! kinetic energy of the system
      eptot = 0.5*sum(ep)       ! potential energy of the system
      ettot  = ektot + eptot    ! total energy of the system

! compute the angular momentum

      forall(i=1:n)
     &     amx(i) = massp(i)*(yp(i)*velz(i) - zp(i)*vely(i))
      forall(i=1:n)
     &     amy(i) = massp(i)*(zp(i)*velx(i) - xp(i)*velz(i))
      forall(i=1:n)
     &     amz(i) = massp(i)*(xp(i)*vely(i) - yp(i)*velx(i))

      amxtot = sum(amx)         ! angular momentum components for the CofM
      amytot = sum(amy)
      amztot = sum(amz)

      amtot = amxtot*amxtot + amytot*amytot + amztot*amztot
```

```
      amtot = sqrt(amtot)

! !!!!!!!!!!!!!!!!!!!!!!!!!!!!!!!!!!!!!!!!!!!!!!!!!!!!!!!!!!!!!!!!!!!!!!!
      print *,' ******************************************'
      print *,' time (ms) to compute the dynamics=',
     &     mpCpuTimerElapsed()

      print *, ' the kinetic energy of the system is   :', ektot
      print *, ' the potential energy of the system is :', eptot
      print *, ' the total energy of the system is     :', ettot
      print *, ' the total angular momentum is         :', amtot
      print *, ' amxtot =', amxtot
      print *, ' amytot =', amytot
      print *, ' amztot =', amztot
      print *, ' cmx =', cmx
      print *, ' cmy =', cmy
      print *, ' cmz =', cmz
      print *, ' Energy(1) =', ek(1), ep(1), et(1)
      print *, ' phi(1)    =',phi(1)
      print *,' ******************************************'

! write to the checkpointer file if you have to


      if (mod(ntmp,nout).eq.0) then

         print *, ' writing into TREEBIN'
         print *,' ******************************************'

         do i=1,n
            write(ulogbod) xp(i), yp(i), zp(i),velx(i), vely(i), velz(i),phi(i)
         end do

      end if

! reset the positions of the particles

      ax = axt
      ay = ayt
      az = azt

      xp = xp + 0.125*ax*dt*dt
      yp = yp + 0.125*ay*dt*dt
      zp = zp + 0.125*az*dt*dt

      return
      end
```

```
! !!!!!!!!!!!!!!!!!!!!!!!!!!!!!!!!!!!!!!!!!!!!!!!!!!!!!!!!!!!!!!!!!!!!!!
! **********************************************************************
      subroutine step_vel(velx,vely,velz,ax,ay,az)

! advance the velocities of the particles by dt

      include 'parameters'

      real * 4 velx(n), vely(n), velz(n)
      real * 4 ax(n), ay(n), az(n)

      velx = velx + ax*dt
      vely = vely + ay*dt
      velz = velz + az*dt

      return
      end
! !!!!!!!!!!!!!!!!!!!!!!!!!!!!!!!!!!!!!!!!!!!!!!!!!!!!!!!!!!!!!!!!!!!!!!
! **********************************************************************
      subroutine step_pos(xp,yp,zp,velx,vely,velz)

! advance the positions of the particles by dt/2

      include 'parameters'

      real *4 xp(n), yp(n), zp(n)
      real * 4 velx(n), vely(n), velz(n)

      xp = xp + velx*dt*0.5
      yp = yp + vely*dt*0.5
      zp = zp + velz*dt*0.5

      return
      end
! !!!!!!!!!!!!!!!!!!!!!!!!!!!!!!!!!!!!!!!!!!!!!!!!!!!!!!!!!!!!!!!!!!!!!!
! **********************************************************************

      subroutine zero_all(ax,ay,az,phi)

! Reset the values of the acceleration and potential to zero.

      include 'parameters'

      real * 4 ax(n), ay(n), az(n)
      real * 4 phi(n)

      ax = 0.
      ay = 0.
```

```
      az = 0.
      phi = 0.

      return
      end

! !!!!!!!!!!!!!!!!!!!!!!!!!!!!!!!!!!!!!!!!!!!!!!!!!!!!!!!!!!!!!!!!!!!!!!!!
! ************************************************************************
```

Building the tree : “build_tree-new.f”

```
      subroutine make_tree (x,y,z,size,doquad,quad,mass,partno,itree,n,
     &     nlevels,level_c,last_node_6, nprocs,n_nodes)

! This subroutine sorts a power of 2 particles by RECURSIVELY
! BISECTING THE LONGEST DIMENSION.  That is, the longest dimension (x,
! y or z) is found.  The particle list is sorted on this dimension.  The
! sorted is then divided exactly in half creating two segments.  Each
! segement is then treated the same as the original list but
! independenlty of one any other segments.  This process continues
! until the segment size is 1.  At this point, the values for the
! nodes of the tree (i.e. center of mass, size and total mass) can be
! computed and these computations constitute the last half of this
! subroutine.

      real * 4 x(n_nodes),y(n_nodes),z(n_nodes),r(n_nodes),size(n_nodes)
      real * 4 xx(n),yy(n),zz(n),xsort(n)
      real * 4 minx(n),miny(n),minz(n)
      real * 4 maxx(n),maxy(n),maxz(n)
      real * 4 mass(n_nodes)

c My additions for the quadrupole moments :
c The variables x2cm,y2cm,z2cm are the x,y,z components of the
c distance of a child from the center of mass of the parent node.

      logical doquad
      real * 4 x2cm(n_nodes,0:7),y2cm(n_nodes,0:7),z2cm(n_nodes,0:7)
      real * 4 quad(n_nodes,0:5)

cmpf map quad(allbits,memory), x2cm(allbits,memory)
cmpf map y2cm(allbits,memory), z2cm(allbits,memory)

c My additions for the extra copies

      integer * 4 nlevels, level_c, last_node_6, nprocs, ncopies
      integer * 4 head(n_nodes), level(n_nodes), cp_node(n_nodes)

c End of the extra variables.

      integer * 4 partno(n),partno2(n_nodes),itree(n)
      integer * 4 isort(n),child(2*n-1)

      integer * 4 step

      logical flag(n_nodes)

! The unsorted particle data is stored in temporaries, xx, yy, zz.
```

```
      xx=x(1:n)
      yy=y(1:n)
      zz=z(1:n)
      itree = partno

      forall (i=1:n_nodes) partno2(i)=i

      call mpCpuTimerStart()

! First find the max and min x, y, and z. maxval, minval etc. are F90
! intrinsic functions.

      xmax=maxval(xx)
      ymax=maxval(yy)
      zmax=maxval(zz)
      xmin=minval(xx)
      ymin=minval(yy)
      zmin=minval(zz)

! compute their differnces

      delxx=xmax-xmin
      delyy=ymax-ymin
      delzz=zmax-zmin

! sort on the maximum among these and rearrange all the particle data

      if (delxx.gt.delyy.and.delxx.gt.delzz) then

         call rad_sort (xx,isort,partno,n)
         yy=yy(isort)
         zz=zz(isort)
         itree = itree(isort)

      else

         if (delyy.gt.delzz) then

            call rad_sort (yy,isort,partno,n)
            xx=xx(isort)
            zz=zz(isort)
            itree = itree(isort)

         else

            call rad_sort (zz,isort,partno,n)
            xx=xx(isort)
```

```
          yy=yy(isort)
          itree = itree(isort)

        end if
      end if

      nseg = n/2

! START the segmented scan of the particle vector

      do while (nseg.gt.1)

        step=1
        minx=xx
        miny=yy
        minz=zz
        maxx=xx
        maxy=yy
        maxz=zz

! The following do loop does a segmented min and max along each coordinate
! direction.

        do while (step.le.nseg/2)

          x(1:n)=minx(partno+step)
          y(1:n)=miny(partno+step)
          z(1:n)=minz(partno+step)

          minx=MIN(minx,x(1:n))
          miny=MIN(miny,y(1:n))
          minz=MIN(minz,z(1:n))

          x(1:n)=maxx(partno+step)
          y(1:n)=maxy(partno+step)
          z(1:n)=maxz(partno+step)

          maxx=MAX(maxx,x(1:n))
          maxy=MAX(maxy,y(1:n))
          maxz=MAX(maxz,z(1:n))

          step=step*2

        end do

! The first member of each segment is marked (i.e. flag is .TRUE.).
! The first member of each segment has the min and max of each coordinate
! direction.
```

```
        step=nseg/2
        flag=.FALSE.
        where (partno.eq.(nseg*int((partno-1)/nseg))+1) flag=.TRUE.

! The following do loop spreads the max and min values stored at the "heads"
! to the rest of the segment.

        do while (step.ge.1)

           where (flag)

              minx(partno+step)=minx
              miny(partno+step)=miny
              minz(partno+step)=minz
              maxx(partno+step)=maxx
              maxy(partno+step)=maxy
              maxz(partno+step)=maxz

              flag(partno+step)=flag

           end where

           step=step/2

        end do

! Since each location now has a copy of the minimum and maximum values stored,
! the coordinate direction on which to sort on can be dertermined in parallel

        minx=abs(maxx-minx)
        miny=abs(maxy-miny)
        minz=abs(maxz-minz)

! In each segment, store the value of the coordinate on which to sort into
! the variable xsort.  This is done independently of the other segments.

        where (minx.gt.miny.and.minx.gt.minz) xsort=xx
        where (miny.gt.minx.and.miny.gt.minz) xsort=yy
        where (minz.gt.minx.and.minz.gt.miny) xsort=zz

! "sort_segs" sorts the segments of the vector "xsort"
! each segment is sorted independently of the others and
! each segment is nseg elements long

        call sort_segs(xsort,isort,partno,n,nseg)

! the following statements permute the particle data into order
```

```
        xx=xx(isort)
        yy=yy(isort)
        zz=zz(isort)
        itree = itree(isort)

        nseg=nseg/2

      end do

! !!!!!!!!!!!!!!!!!!!!!!!!!!!!!!!!!!!!!!!!!!!!!!!!!!!!!!!!!!!!!!!!!!!!!!!!!!!!

! Now the particles are in order.  The values of center of mass, size and total
! mass for each node in the tree can now be computed via scan functions.

      x(1:n)=xx
      y(1:n)=yy
      z(1:n)=zz
      size(1:n)=0.0
      mass(n+1:n_nodes)=0

      level = 0
      level(1:n) = nlevels     ! The particles are at the lowest level (6)
      head =  0
      head(1:n) = 1            ! The information for the particles are
                               ! stored on each processor
      nmin=n+1
      nmax=n+(n/8)
      step=n/8

! child is the location of the "left-most" child of the node(s) being
! computed (the tree being constructed here is an 'oct' tree of 8
! children per internal node).

      child = (8*(partno2-n-1)) + 1

!      child2 = child1 + 1
!      child3 = child1 + 2
!      child4 = child1 + 3
!      child5 = child1 + 4
!      child6 = child1 + 5
!      child7 = child1 + 6
!      child8 = child1 + 7

      do while (nmin.le.nmax)


! !!!!!!!!!!!!!!!!!!!!!!!!!!!!!!!!!!!!!!!!!!!!!!!!!!!!!!!!!!!!!!!!!!!!!!!!!!
```

```
! the TOTAL MASS of the node is computed.
! NOTE: we really wouldn't need this number since we are assuming
! that all the particles have equal mass and this could easily be computed
! as the tree is searched.

!         mass(nmin:nmax) = mass(nmin:nmax) + mass(child1(nmin:nmax)) +
!     &        mass(child2(nmin:nmax)) + mass(child3(nmin:nmax)) +
!     &        mass(child4(nmin:nmax)) + mass(child5(nmin:nmax)) +
!     &        mass(child6(nmin:nmax)) + mass(child7(nmin:nmax)) +
!     &        mass(child8(nmin:nmax))

        do j = 0,7
           mass(nmin:nmax) = mass(nmin:nmax) + mass(child(nmin:nmax)+j)
        end do

! The mass is computed on the fly since mass(i)=n/(8**(level-1))

! The locations of the CENTER OF MASS are computed.
! Here the particles are assumed to have equal mass and each node
! has exactly 8 children (a balanced tree).

        x(nmin:nmax) = 0.
        y(nmin:nmax) = 0.
        z(nmin:nmax) = 0.

        do j = 0,7

           x(nmin:nmax) = x(nmin:nmax) +
     &          mass(child(nmin:nmax)+j) * x(child(nmin:nmax)+j)
           y(nmin:nmax) = y(nmin:nmax) +
     &          mass(child(nmin:nmax)+j) * y(child(nmin:nmax)+j)
           z(nmin:nmax) = z(nmin:nmax) +
     &          mass(child(nmin:nmax)+j) * z(child(nmin:nmax)+j)

        end do

!         x(nmin:nmax) = x(nmin:nmax) +
!     &        mass(child1(nmin:nmax)) * x(child1(nmin:nmax)) +
!     &        mass(child2(nmin:nmax)) * x(child2(nmin:nmax)) +
!     &        mass(child3(nmin:nmax)) * x(child3(nmin:nmax)) +
!     &        mass(child4(nmin:nmax)) * x(child4(nmin:nmax)) +
!     &        mass(child5(nmin:nmax)) * x(child5(nmin:nmax)) +
!     &        mass(child6(nmin:nmax)) * x(child6(nmin:nmax)) +
!     &        mass(child7(nmin:nmax)) * x(child7(nmin:nmax)) +
!     &        mass(child8(nmin:nmax)) * x(child8(nmin:nmax))

!         y(nmin:nmax) = y(nmin:nmax) +
```

```
!    &         mass(child1(nmin:nmax)) * y(child1(nmin:nmax)) +
!    &         mass(child2(nmin:nmax)) * y(child2(nmin:nmax)) +
!    &         mass(child3(nmin:nmax)) * y(child3(nmin:nmax)) +
!    &         mass(child4(nmin:nmax)) * y(child4(nmin:nmax)) +
!    &         mass(child5(nmin:nmax)) * y(child5(nmin:nmax)) +
!    &         mass(child6(nmin:nmax)) * y(child6(nmin:nmax)) +
!    &         mass(child7(nmin:nmax)) * y(child7(nmin:nmax)) +
!    &         mass(child8(nmin:nmax)) * y(child8(nmin:nmax))

!         z(nmin:nmax) = z(nmin:nmax) +
!    &         mass(child1(nmin:nmax)) * z(child1(nmin:nmax)) +
!    &         mass(child2(nmin:nmax)) * z(child2(nmin:nmax)) +
!    &         mass(child3(nmin:nmax)) * z(child3(nmin:nmax)) +
!    &         mass(child4(nmin:nmax)) * z(child4(nmin:nmax)) +
!    &         mass(child5(nmin:nmax)) * z(child5(nmin:nmax)) +
!    &         mass(child6(nmin:nmax)) * z(child6(nmin:nmax)) +
!    &         mass(child7(nmin:nmax)) * z(child7(nmin:nmax)) +
!    &         mass(child8(nmin:nmax)) * z(child8(nmin:nmax))


         x(nmin:nmax) = x(nmin:nmax)/mass(nmin:nmax)
         y(nmin:nmax) = y(nmin:nmax)/mass(nmin:nmax)
         z(nmin:nmax) = z(nmin:nmax)/mass(nmin:nmax)

! !!!!!!!!!!!!!!!!!!!!!!!!!!!!!!!!!!!!!!!!!!!!!!!!!!!!!!!!!!!!!!!!!!!!!!!!!!!!

! The SIZE of each node is computed.  The size is taken to be the
! maximum distance (measured from the center of mass of the node)
! of a particle which is a member of this node
!
c Vassilis
c
c I need to calculate the distance of each child from the center mass,
c and store the x,y,z, values of that for later use (calculation of quad)
c
c I define real, array(nmin:nmax,0-7):: x2cm, y2cm, z2cm for this purpose

         x2cm(nmin:nmax,:) = 0.
         y2cm(nmin:nmax,:) = 0.
         z2cm(nmin:nmax,:) = 0.

         do j = 0,7

            x2cm(nmin:nmax,j) = x(nmin:nmax)-x(child(nmin:nmax)+j)
            y2cm(nmin:nmax,j) = y(nmin:nmax)-y(child(nmin:nmax)+j)
            z2cm(nmin:nmax,j) = z(nmin:nmax)-z(child(nmin:nmax)+j)

            r(nmin:nmax) = x2cm(nmin:nmax,j)**2 +
```

```
     &           y2cm(nmin:nmax,j)**2 +
     &           z2cm(nmin:nmax,j)**2


           r(nmin:nmax) = sqrt(r(nmin:nmax)) +
     &           size(child(nmin:nmax)+j)
           size(nmin:nmax) = MAX(size(nmin:nmax),r(nmin:nmax))

        end do

! !!!!!!!!!!!!!!!!!!!!!!!!!!!!!!!!!!!!!!!!!!!!!!!!!!!!!!!!!!!!!!!!!!!!!!!!!!!!!!

c Vassilis
c
c The QUADRUPOLE MOMENTS of the particle particle distribution that
c constitutes each node are calculated. The results are stored in the array
c quad(node_number,0:5). We note that there is no dipole moment when one
c calculates the multiple expansion at the center of mass.
c


c I need the following arrays:
c quad(nmin:nmax,0:5)  --> The six quadrupole moments
c
c I define :
c quad(nimn:nmax,0) = SUM { m(i)*x(i)*x(i) }
c quad(nimn:nmax,1) = Qyy
c quad(nimn:nmax,2) = Qzz
c quad(nimn:nmax,3) = Qxy
c quad(nimn:nmax,4) = Qxz
c quad(nimn:nmax,5) = Qyz
c

        if (doquad) then

           quad(nmin:nmax,:) = 0.

c Calculate contributions from children.

              do j = 0,7

                 quad(nmin:nmax,0) = quad(nmin:nmax,0) +
     &                quad(child(nmin:nmax)+j,0) +
     &                mass(child(nmin:nmax)+j)*(x2cm(nmin:nmax,j)**2)

                 quad(nmin:nmax,1) = quad(nmin:nmax,1) +
     &                quad(child(nmin:nmax)+j,1) +
     &                mass(child(nmin:nmax)+j)*(y2cm(nmin:nmax,j)**2)
```

```
                 quad(nmin:nmax,2) = quad(nmin:nmax,2) +
     &                quad(child(nmin:nmax)+j,2) +
     &                mass(child(nmin:nmax)+j)*(z2cm(nmin:nmax,j)**2)

                 quad(nmin:nmax,3) = quad(nmin:nmax,3) +
     &                quad(child(nmin:nmax)+j,3) +
     &                mass(child(nmin:nmax)+j) *
     &                2.*x2cm(nmin:nmax,j)*y2cm(nmin:nmax,j)

                 quad(nmin:nmax,4) = quad(nmin:nmax,4) +
     &                quad(child(nmin:nmax)+j,4) +
     &                mass(child(nmin:nmax)+j) *
     &                2.*x2cm(nmin:nmax,j)*z2cm(nmin:nmax,j)

                 quad(nmin:nmax,5) = quad(nmin:nmax,5) +
     &                quad(child(nmin:nmax)+j,5) +
     &                mass(child(nmin:nmax)+j) *
     &                2.*y2cm(nmin:nmax,j)*z2cm(nmin:nmax,j)

              end do


           end if

! !!!!!!!!!!!!!!!!!!!!!!!!!!!!!!!!!!!!!!!!!!!!!!!!!!!!!!!!!!!!!!!!!!!!!!!!!

! Now compute the next level (root node is level # 1)

           level(nmin:nmax) = level(child(nmin:nmax)) - 1
           head(nmin:nmax) = nmin
           nmin=nmax+1
           nmax=nmax+(step/8)
           step=step/8

        end do
! !!!!!!!!!!!!!!!!!!!!!!!!!!!!!!!!!!!!!!!!!!!!!!!!!!!!!!!!!!!!!!!!!!!!!!!!!

! make the extra copies for each of the levels

        do j = 1, level_c

           flag = .FALSE.
           ncopies = nprocs/(8**(j-1))

           where (level.eq.j)

              cp_node = ((partno2-head) * ncopies) +
```

```
*          (nprocs * (level_c-level)) + 1 + last_node_6

        x(cp_node) = x
        y(cp_node) = y
        z(cp_node) = z
        mass(cp_node) = mass
        size(cp_node) = size
        quad(cp_node,0) = quad(:,0)
        quad(cp_node,1) = quad(:,1)
        quad(cp_node,2) = quad(:,2)
        quad(cp_node,3) = quad(:,3)
        quad(cp_node,4) = quad(:,4)
        quad(cp_node,5) = quad(:,5)
        flag(cp_node) = .TRUE.

     end where
     step = 1
     do while (step.le.ncopies/2)

        where (flag)

           x(partno2+step) = x
           y(partno2+step) = y
           z(partno2+step) = z
           mass(partno2+step) = mass
           size(partno2+step) = size
           quad(partno2+step,0) = quad(:,0)
           quad(partno2+step,1) = quad(:,1)
           quad(partno2+step,2) = quad(:,2)
           quad(partno2+step,3) = quad(:,3)
           quad(partno2+step,4) = quad(:,4)
           quad(partno2+step,5) = quad(:,5)
           flag(partno2+step) = .TRUE.

        end where

        step = step*2

     end do

  end do


! !!!!!!!!!!!!!!!!!!!!!!!!!!!!!!!!!!!!!!!!!!!!!!!!!!!!!!!!!!!!!!!!!!!!!!!!!!!


  time=mpCpuTimerElapsed()/1000.0
  print *,' time to make tree            =',time
```

```
!       print *, n_nodes

!       do i = 1,n_nodes
!          write (10,*) i, mass(i)
!       end do

!       do i = 1,n_nodes
!          write (11,*) i, x(i)
!       end do


       return
       end
```

Subroutines

The following subroutines are doing the sorting and were stored in the library

$(LIBDIR)libsort_mp2.a

```
      subroutine rad_sort(x,ilist,partno,n)

c This subroutine sorts a list of real numbers, x, into increasing
c order.  n is the total number of elements of x.  ilist is a permute
c address that enables the callig routine to order other number in a
c record of numbers that also contains x.  rad_sort calls radix_sort.

      real * 4 x(n)
      real * 4 xt(n)
      real * 4 xo(n)
      real * 4 size,xmax,xmin

      integer * 4 partno(n)
      integer * 4 ilist(n),ilistt(n),ix(n)

      xmax=maxval(x)
      xmin=minval(x)

      size=(xmax-xmin)/(100*n)

      if (size.ne.0.0) then
         ix=int((x-xmin)/size)+1
      else
         ix=1
      end if

      ilist=partno

      call radix_sort(ix,ilist,n)

      x=x(ilist)

c bubble sort to finish

      xt=x
      ilistt=ilist

      where (partno.gt.1)
         xo=x-x(partno-1)
      elsewhere
         xo=1.0
      end where
```

```
      j=0

      do while (any(xo.lt.0))

c         where (partno.ne.1) xo=x-x(partno-1)

         forall (i=1:n,i.ne.1) xo(i)=x(i)-x(i-1)

c         where (xo.lt.0.0.and.xo(partno-1).ge.0.0)

c            x(partno-1)=x
c            x=xt(partno-1)
c            ilist(partno-1)=ilist
c            ilist=ilistt(partno-1)

c end where

         forall (i=1:n,xo(i).lt.0.0.and.xo(i-1).ge.0.0)
     &        x(i-1)=x(i)
         forall (i=1:n,xo(i).lt.0.0.and.xo(i-1).ge.0.0)
     &        x(i)=xt(i-1)
         forall (i=1:n,xo(i).lt.0.0.and.xo(i-1).ge.0.0)
     &        ilist(i-1)=ilist(i)
         forall (i=1:n,xo(i).lt.0.0.and.xo(i-1).ge.0.0)
     &        ilist(i)=ilistt(i-1)

        xt=x
        ilistt=ilist

        j=j+1

      end do

      return
      end
```

```
c     split_radix_sort
c     Blelloch p.43
c
      subroutine radix_sort(keys,data,n)

c This subroutine sorts integers into increasing order.

      integer * 4 nbits

      integer n,iposition,ntrue,bot
      integer keys(n),data(n)

      logical m(n)

      complex * 8 ka(n),ra(n),im(n)

      ka = cmplx(keys,data)

      im = (0,-1)

      nbits=(log10(real(maxval(keys)))/log10(2.)) + 1
      if (2**nbits.lt.maxval(keys)) nbits = nbits + 1

      do iposition = 0, nbits-1

         m = BTEST(int(real(ka)),iposition)

         ntrue = count(m)

         bot = n-ntrue+1

         ra = 0


         ra(1:n) = PACK(ka,.not. m,ka)

         ra(bot:n) = PACK(ka,m,ka)

         ka = ra

      end do

      keys = real(ka)
      data = real(im*ka)

      return
      end
```

```
      subroutine sort_segs (x,ilist,partno,n,nseg)

! This subroutine sorts a vector which is divided into segments.  Each
! segment is sorted independently of the others.  The segment length is
! nseg. ilist is a permute location which is sorted along with the vector
! x.  ilist is used to permute other data associated with x after the
! sort is completed.  It calls radix_sort.

      real * 4 x(n)
      real * 4 xt(n)
      real * 4 xo(n)
      real * 4 size,xmax,xmin

      integer * 4 partno(n)
      integer * 4 ilist(n),ilistt(n),ix(n)

      logical iflag(n)

      xmax = maxval(x)
      xmin = minval(x)

      size = (xmax-xmin)/(100*nseg)

      if (size.ne.0.0) then
         ix = int((x-xmin)/size)+1
      else
         ix = 1
      end if

      ix = ix + (100*nseg*int((partno-1)/nseg))
      ilist = partno

      call radix_sort(ix,ilist,n)

      x = x(ilist)

c bubble sort to finish

      xt = x
      ilistt = ilist

      where (partno.gt.nseg*int((partno-1)/nseg)+1)
         xo = x-x(partno-1)
      elsewhere
         xo = 1.0
      end where

      do while (any(xo.lt.0))
```

```
    forall (i=1:n,i.ne.nseg*int((i-1)/nseg)+1)
&        xo(i) = x(i)-x(i-1)

    forall (i=1:n,xo(i).lt.0.0.and.xo(i-1).ge.0.0)
&        x(i-1) = x(i)
    forall (i=1:n,xo(i).lt.0.0.and.xo(i-1).ge.0.0)
&        x(i) = xt(i-1)
    forall (i=1:n,xo(i).lt.0.0.and.xo(i-1).ge.0.0)
&        ilist(i-1) = ilist(i)
    forall (i=1:n,xo(i).lt.0.0.and.xo(i-1).ge.0.0)
&        ilist(i) = ilistt(i-1)

   xt = x
   ilistt = ilist

 end do

 return
 end
```